Imperial College London
Department of Physics

Detecting Atoms with Integrated Optics and Frequency-Synthesised Light

Matthias Kohnen

November 2012

Supervised by Prof. Edward A. Hinds

Submitted in part fulfilment of the requirements for the degree of
Doctor of Philosophy in Physics of Imperial College London
and the Diploma of Imperial College London

Declaration

I declare that the work presented in this thesis is my own and that all work by others used in this thesis is appropriately referenced.

Abstract

This thesis reports on the development of novel techniques for the detection and manipulation of cold gases of neutral atoms. The research presented focusses on the implementation of a photonic waveguide chip into an atom optics experiment. Our photonic chip consists of 12 parallel waveguides with a 10 μm pitch and a 16 μm trench in the centre. A wire subchip underneath the photonic chip can create magnetic fields to guide atoms into the trench and hold them there. The electric field of the light mode propagating through the waveguides has a $1/e$ radius of 2.2 μm. This small light mode can readily be used for local measurements of the atomic density. This thesis describes the setup of the waveguide chip experiment and gives a detailed characterisation of the interaction between light and atoms in the trench.

Additionally, I report on a scheme for detecting atoms while minimising the number of scattered photons for a given precision of the measurement. We use a light beam synthesized from two frequencies tuned to either side of the atomic resonance and detect the differential phase shift they acquire when passing through an atomic cloud by referencing the beat between the two frequencies to a local oscillator. Unlike most similar techniques our beam does not contain a carrier signal and can therefore be balanced around the atomic resonance in order to cancel the mean optical dipole force on the atoms.

Contents

1 Introduction **15**

1.1 Our waveguide chip 17

1.2 Optimising measurements 18

1.2.1 Figure of merit 18

1.2.2 Summary 21

1.3 Contents of this thesis 22

2 Photonic waveguide chips **23**

2.1 Propagation of light in an optical waveguide 24

2.2 Mode matching between fibres and waveguides 26

2.3 Transmission through the trench 28

2.4 Waveguide chips for atom-optical experiments 29

2.5 Connecting the chip 29

2.5.1 Practical considerations 29

2.5.2 Alignment 31

2.5.3 Testing the thermal stability 34

2.5.4 Placing the chip in vacuum 35

2.5.5 Results 35

3 Atom-Light interaction **36**

3.1 Atomic Hamiltonian 37

3.2 Interaction with the electric field 40

3.3 Incoherent interaction with the vacuum 41

3.4 Dressed states 42

3.5 Effect on the light field 43

3.6 Obtaining solutions 44

4 Experimental setup **46**

4.1 Laser setup 46

4.2 Vacuum . . . 49
4.2.1 Setup . . . 49
4.2.2 Limitations . . . 51
4.3 Magneto-optical trapping . . . 53
4.4 Magnetic trapping . . . 54
4.5 Subchip . . . 54
4.6 Two generations of atom chips . . . 56
4.7 Coils . . . 57
4.8 Basic experiment . . . 58

5 Detecting atoms with a photonic chip 61
5.1 Atoms in a light mode . . . 61
5.2 Characterising 12 atom-photon junctions . . . 63
5.3 Measuring polarisation stability . . . 68
5.4 Measuring intensity . . . 71
5.5 Using magnetic traps . . . 74

6 Detecting atoms with frequency-synthesised light 78
6.1 Frequency-synthesising light . . . 80
6.2 Identifying noise sources . . . 83
6.2.1 Expected noise . . . 83
6.2.2 Experiments . . . 86
6.2.3 Discussion . . . 89
6.3 Phase-shift signals . . . 90
6.4 Losses . . . 93
6.5 Figure of merit . . . 98

7 Temporal correlation functions 103
7.1 Correlation functions . . . 104
7.2 Correlations in an ideal Bose gas . . . 105
7.3 Gaussian probe beam . . . 108
7.4 Numerical values . . . 110
7.5 Possible measurements . . . 111
7.6 Summary . . . 114

8 Conclusion and Outlook 116

9 Appendix **119**

9.1 Calculating the figure of merit for absorption and phase measurements . . . 119

9.1.1 Absorption . . . 120

9.1.2 Interferometer . . . 121

9.2 Temporal correlations: Next steps . . . 122

9.2.1 Interacting thermal gas . . . 122

9.2.2 Condensation . . . 123

List of Tables

2.1 Properties of Epotek-OG116, taken from preliminary data sheet. 31

5.1 Parameters of magnetic trap for current values before and after the compressing phase. The values are results of a simulations but agree with experimental observations. 75

6.1 Parameters of the beat note detection system necessary to calculate the expected noise level. The table also indicates the origin of each value. The product of sensitivity of the diode and transimpedance gain of the AAPD ($G_t S = G_t e\eta \langle G \rangle_a \lambda/(hc)$) was confirmed experimentally. 89

List of Figures

1.1 Artist impression of our photonic waveguide chip. A silica layer is deposited onto a silicon substrate and coated with a gold layer. The sketch shows six of the twelve waveguides, which fan out towards both ends of the chip, where they are connected to a fibre array. The waveguide are intercepted by a 16 μm wide trench to guide atoms into the light mode. Figure taken from reference [49]. 18

1.2 Sketch of a setup for detecting the absorption and the phase shift of a light beam passing through a cloud of atoms. In an absorption measurement the light power of a probe beam passing through an atomic sample is compared to the power of the beam when no atoms are present. For measuring the phase shift a reference beam is required, which in this example is provided by splitting the beam on a beam splitter (BS) and guiding one part of the light around the atoms. Both beams are combined on a second BS and interfere. 19

2.1 The right image shows the intensity profile of the waveguide mode obtained with a Fourier decomposition method as explained in the text. The left graph shows a cut through that intensity profile in horizontal ($y = 0$ and diagonal ($x = y$) direction. It also show the Gaussian profile that matches the two cuts best. The fitted width parameter w_0 is 2.18 μm in agreement with the far field measurements. 26

2.2 Intensity (left) and phase (right) of a freely expanding Gaussian beam. The axis are in units of the Rayleigh range z_R. 0 corresponds to the position of the first waveguide. The light then freely diverges in the trench. The black vertical line indicates the position of the second waveguide where the light leaves the trench. 29

2.3 Comparison of the transmission calculated from the real and complex integral. For $l = z_R$ the loss taking the phase mismatch into account is approximately 10 % larger then the pure intensity overlap. 30

2.4 Alignment stage for connecting the V-groove assemblies to a waveguide chip. Clamps mounted on a prism mount (4) hold the V-groove assemblies (5) consisting of transparent lid (a), silicon base (b) and fibres (6) in place. The waveguide chip (7) is mounted on a dummy subchip (3). Translational adjustment is done using micro positioning stages (1). For visual inspection a microscope objective (2) is used. The lower picture shows a zoom on the waveguide-fibre interface on the chip after assembly (clamps removed). . . 33

3.1 Energy differences between the ground and excited states hyperine levels of the ^{87}Rb D_2 line. The splittings are to scale within each manifold, but different for each manifold and for the optical transition. Along with the energies the Landé factors g_F and the corresponding magnetic moment $g_F\mu_B/\hbar$ are given. Not shown are the Zeeman sublevels of the hyperfine states, which are degenerate when no external magnetic field is present. Figure taken from reference [1]. 38

4.1 Photographs of the experiment. Top right: Image of the main chamber including cryopump and getter pump. Magnetic coils on the vacuum windows are used to create offset fields. Current for magnetic trapping runs through the blue cables, which end in electrical feedthroughs on the the top flange. The LVIS chamber is visible at the back. A schematic diagram of the vacuum setup can be found in figure 4.3. Top right: Top flange (goes onto the main chamber upside down) containing copper subchip, electric feedthroughs, photonic waveguide chip and optical feedthroughs. Bottom left: Optics underneath the main chamber, including a Pike CCD camera and the optics for the magneto-optical trap. The main chamber sits on top of the plate at the top and is optically accessible via a hole in the plate and a viewport in the bottom flange. Bottom right: Laser setup, including lasers for cooling (TA) of Rubidium atoms, for stabilising the cooling laser to a rubidium transition (Ref) and for pumping atoms lost into substates that are not part of the cooling cycle back into the cycle (ReM and ReS). Details are explained in figure 4.2. 47

4.2 Sketch of the laser configuration used in the experiment. Neglecting details, the figure shows how the light from the Reference (Ref), Repump master (ReM) and slave (ReS) and tapered amplifier (TA100) are combined and distributed amongst the fibres for the two imaging axes (Im1 and Im2), waveguides (WG) and the frequency synthesis setup (FS) as well as the free-space beam paths for MOT and LVIS. The laseres are referenced to the atomic transition using polarisation spectroscopy (Pol Spec) and saturation spectroscopy (Sat Spec). The left diagram shows the transitions addressed by the lasers and their relative detunings. 50

4.3 Sketch of the vacuum chamber, showing beam path for the horizontal MOT beam and the frequency-synthesised probe beam (FS). The waveguides on the chip run parallel to the FS beam. The pumping section on the left consists of an ionisation pump (ION) and an ionisation gauge. The non-evaporable getter pump (NEG) was recently moved to the main chamber to increase the pumping speed. The cryogenic pump (CRYO) was also fitted recently to pump heavier molecules that are released from glue and the acrylate fibre coating. 51

4.4 Pressure rise after switching off the ion pump as measured in a test chamber with similar volume and pumping speed to the main chamber. The three curves show the pressure rise for an empty chamber, a chamber containing large amounts of glue and a chamber with 10 m of fibre, including the acrylate coating. 52
4.5 Magnetic field geometries for creating trapping potentials with a wire and an offset field. The geometries used on our experiment are the U wire configuration (b) for the MOT and the Z wire trap (c) for conservatively trapping the atoms. Figure taken from [12]. 55
4.6 Exploded drawing of the chip as it is mounted on the vacuum flange. From bottom to top the layers are (purpose in brackets): Copper block (heat sink), U plate (MOT fields), Shapal layer (electrical insulation), ribbon wires (bias fields), wire plate (field gradients), waveguide chip (light access). 56
4.7 Left side: Wire plate with H structure coloured in dark grey and end wires coloured in light gray. The lower right part shows a zoom of the central part of the H. The wires are 1.2 mm wide and the central part of the H is 4 mm long (inner part only). The plate is 0.5 mm thick. Upper right: Dimensions of the U-plate are 10 mm × 24 mm (without connectors). The plate is 1 mm thick. 57
4.8 Absorption image of a magnetically trapped cloud containing 600, 000 atoms. The color scale corresponds to the optical density, where red corresponds to a larger optical depth. The long axis of the cloud is 350 μm long. The imaging beam is reflected of the waveguide chip and the mirror image of the cloud is visible as well. The waveguides (going from bottom to top slightly left of the centre of the image) produce an uneven surface of the chip, and light hitting those region is scattered and not captured by the camera. 60

5.1 Absorption and fluorescence of light by atoms detected with the waveguide chip. The curves are an average from several individual runs to increase the signal-to-noise ratio. 63
5.2 Measuring transmission across the setup. We denote as total transmission the fraction of power measured on the photo diode (PD) in part B of the power measured in part A. Losses occur at the interfaces labelled in blue. For the measurement of the atomic saturation the bare fibre terminator unit (BFTU) is replaced with a fibre splicer and losses from the trench to the PD are measured. This isolates the loss due to one waveguide-fibre interface. 66
5.3 Three measurements to characterise the waveguide. Top: Transmission of light through the whole setup. Centre: Absorption due to atoms in the trench. Bottom: Fluorescence from a focused light beam. A Gaussian profile with a $2/e$ radius of 40 μm fits the measurement. Channel 2,5 and 9 do not work in the third measurement (see text). One of the outermost channels shows almost no transmission and is not included in the graph. . 67

5.4 Measurement of the mapping of input polarisation to atomic transitions via Zeeman spectroscopy of atoms in a magnetic field. Data for each graph is acquired over the course of 1 h. Top: Atoms in a magnetic field of +0.78 mT, right handed circular light at the input. The light drives on average 85% σ^- transitions (left peak). Centre: Atoms in a magnetic field of −0.78 mT, left handed circular light at the input. The light drives on average 80% σ^+ transitions (left peak). Bottom: Atoms in a magnetic field of +0.78 mT, linear (vertically) polarised light at the input. The light drives on average 35% σ^- transitions (left peak). 69
5.5 Stability of polarisation mapping. The data acquired over the course of 70 min for the centre graph in figure 5.4 is analysed in intervals of 10 min and the relative fraction of light driving σ^+ transitions in each interval is plotted. The fraction decreases from (95 ± 10) % to (65 ± 10) % during the measurement. The setup is therefore stable enough to perform polarisation sensitive measurements. 70
5.6 Measurement of the atomic saturation. The fitted saturation power is (26 ± 3) pW, indicating a coupling efficiency at the waveguide-fibre interface of $(16 \pm 6 \pm 2)$ %. 73
5.7 Averaged fractional absorption as a function of time relative to the switch-off of the magnetic fields gradients. The two curves are recorded at the maximum of the two frequency peaks in figure 5.8. The peak at lower frequencies corresponds to the earlier peak on the time trace. 76
5.8 Spectrum showing the maximum absorption seen on the light transmitted through a waveguide when moving the trap into the trench. The absorption data is independently analysed before (blue curve) and after (green curve) the trap is switched off. The first peak corresponds to the cycling transition in the trap with a trap bottom field of 0.5 mT in z direction (along the trench), the second peak to the cycling transition in the homogeneous offset field of 1.3 mT in y direction (direction of gravity). The second peak also shows contributions of the π transition. 76

6.1 Experimental setup. (A) Synthesis: The incoming beam is modulated by a double-pass acousto-optical modulator (AOM) driven with two frequencies rf_1 and rf_2, which makes use of a quarter-wave plate ($\lambda/4$) and a polarising beam splitter cube (PBS). The output is coupled into a single-mode fibre. (C) Experimental chamber: The beam leaving the fibre is collimated, passed through a linear polariser (LP) and focussed (L_3) onto the magnetic trap (MT), re-collimated (L_4) and coupled back into a multi-mode fibre. (B) Demodulation: Light is detected with an analogue avalanche photodiode (AAPD). A phase sensitive detector (PSD) determines the in-phase and quadrature part of the beat note signal. Modulation and reference signals are produced by the same multi-channel direct digital synthesizer (DDS), and therefore phase stable. The PSD outputs as well as the output of the AAPD are recorded by a computer controlled analogue-to-digital converter (ADC). 82

6.2 Noise spectrum of the AAPD. The upper graph shows the spectrum recorded with 22 nW of light incident on the photo-diode, where the photon shot noise is the dominant noise source. The acquisition bandwidth is 200 kHz. The lower graph shows the Fourier spectrum of the AAPD signal when no light is hitting the diode. Here, the $1/f$ characteristics (red line) of electronic noise dominates the spectrum up to 100 kHz. 84

6.3 Fluctuations of signals from 50 light pulses, each of 10 μs duration. The graphs show the pulse-to-pulse standard deviation of the filtered AAPD output V_0 (top left), the demodulator output V_i and V_q (top right) and the inferred quantities of beat note amplitude (bottom left) and phase (bottom right). Along with the experimental data, the relevant parts of the noise model given in equation 6.5 and the counting ($\sqrt{N}$) noise is plotted. The phase noise graph also contains a line indicating the pure photon shot noise limit without the excess noise introduced by the avalanche process. 88

6.4 Measurement of phase shift θ and amplitude reduction τ of an optically-carried 60 MHz beat note signal due to atoms in a magnetic trap as a function of detuning relative to an arbitrary zero. Light is polarised perpendicular to the magnetic field. The solid lines are fits of phase shift and absorption calculated from equation 6.8 and 6.7. Fitting parameters are the magnetic field, frequency offset and the atomic column density $N_c = (2.2 \pm 0.6) \times 10^{12}$ m^{-2}. 93

6.5 Measurement of the axial trap frequency in a single realisation of the experiment. 120 light pulses of 50 μs with 2×10^6 photons each at a repetition rate of 1 kHz are applied to the atoms. The frequency bands are separated by 60 MHz, with a central frequency detuning corresponding to +17.3 MHz in figure 6.4. The inferred density variations are due to movements of the cloud in and out of the beam. A damped sine wave of (21 ± 1) Hz and a damping coefficient of 0.26 s^{-1} fits the data. 94

6.6 Loss of atoms from a magnetic trap due to 200 light pulses of 30 μs and 60 μs, containing 3×10^5 and 6×10^5 photons each, respectively. The loss is due to depumping of the atoms into an untrapped or weakly-trapped state. Since depumping is about 7 times less likely for atoms exposed to perpendicular light than for those interacting with parallel light, the loss also decreases by the same factor. The solid lines are theoretical predictions from a rate equation model. 95

6.7 Relative coupling strengths for excitations from the trapped $|F, m\rangle = |2, 2\rangle$ state. Transitions driven by light perpendicular (parallel) to the magnetic field are indicated by a solid (dashed) line. The branching ratios from the excited states back to the different ground states are also shown. An atom undergoing a transition to the weakly and untrapped states (dotted lines) are considered to be lost. 96

6.8 Trapping potentials for the trapped $|2, 2\rangle$ and weakly trapped $|2, 1\rangle$ ground states. The dashed line show the magnetic trap potential only, the solid curves the comprised magnetic potential and the gravitational forces which lower the barrier for escape by such an amount that almost all of the atoms in $|2, 1\rangle$ leave the trap between measurement pulses. 97

6.9 Figure of merit (FoM) for an idealised detector and light polarised perpendicular to the magnetic field. The two curves show the FoM for atoms in a magnetic trap (solid line) and in a negligible magnetic field (dashed line). When lifting the degeneracy of the magnetic sublevels the symmetry of the graph is broken. At the same time the optimum FoM is increased. 100

6.10 Optimising the figure of merit η in terms of central detuning f_0, beat frequency $2\delta f$, and number of photons N_γ. The average magnetic field is set to 0.65 mT, as in figure 6.4. The figure of merit (FoM) is calculated using the phase noise presented in equation 6.5, with (solid line) and without (dashed line) mechanical/technical noise. In (a) the FoM is calculated for different values of the central frequency f_0. The optimum values is found at $f_0 = +22.3$ MHz. (b) shows the maximum of $\eta(f_0)$ for different values of $2\delta f$. The best value for operation is $2\delta f \gtrsim 60$ MHz. (c) shows the FoM versus the number of photons used in a probe pulse. Here, the maximum is at $N_\gamma = 35000$. In all graphs the values that are not scanned are fixed at their optimum values for operation. 101

7.1 Bosonic enhancement of the correlations of the atom number fluctuations ($\tilde{C}_2(\tau, 0)$ from equations 7.30) for a set of parameters typical for our experiments (see text). Dashed line: correlations calculated with simple propagator (equation 7.21), solid line: calculated with full propagator (equation 7.20). 111

7.2 Optimising the signal-to-noise ratio ($\tilde{C}(0,0)/\sigma_C$) of the measurement by varying temperature and probe beam size. The SNR is maximised by maximising the average atomic column density in the beam either by reducing the temperature or by reducing the beam size and thus focussing the beam onto the dense parts of the cloud. 114

1 Introduction

The study of ultracold neutral atoms has greatly enhanced our understanding of the quantum nature of matter. The key strengths of experiments with ultracold atoms is that their interaction with the surroundings can be made weak and the confining potential and the interactions between particles can easily be tuned. State-sensitive detection with up to single particle resolution can be done with as little as a carefully tuned laser beam and a CCD camera. Time scales for the motion of the atoms are set by the curvature of the confining potential and typically on the order of milliseconds, well resolvable with standard electronics.

Dilute quantum gases are not readily found in nature. We generate them to examine the behaviour of matter isolated from the influence of its surroundings. They are also used to mimic systems found in nature, but with a handle on the interactions. Both fundamentally different kinds of particles, Bosons [2, 3, 4] and Fermions [5] can be cooled deep into the quantum regime, giving the experimentalist the freedom to pick between the two. Using Feshbach resonances, two Fermions can be associated to form a bosonic molecule, which can then be condensed [6, 7, 8]. The interactions between the two particles are controlled by a homogeneous offset field. Varying this field, the regime from a Bose-Einstein condensate to a degenerate and weakly interacting Fermi gas can be explored (BEC-BCS crossover [9, 10]).

The potential trapping the particles can be formed with a gradient magnetic field or a laser beam with spatially varying intensity. Therefore, overlapping standing light waves in the three spatial dimensions can generate a potential similar to the one electrons see in a crystal or a metal. Tuning the depth of the lattice, the crossover from a superfluid to a Mott-insulator can be explored [11].

A common goal is to further enhance the control over the atoms up to a point where any arbitrary quantum system can be modelled. This goal requires careful engineering of the tools used to manipulate and detect the

atoms. An atomic physicist's toolbox mainly contains magnetic fields and light beams. To enhance the precision of these tools we try to shrink them down to the size of the object we want to handle. This is in our case a ^{87}Rb atom. For light scattering the size of the atom is given by the scattering cross section σ_0. This cross section is set by the wavelength λ of the light, which is for the transition we address 780 nm. For a resonant light beam driving a transition between two atomic states we get

$$\sigma_0 = \frac{3\lambda^2}{2\pi}. \tag{1.1}$$

Using a light beam with an area of the order of σ_0 helps us to individually address small samples of atoms or even single atoms. It is then desirable to have not only a single, isolated atomic sample, but an array of several of them, so that the interactions between neighbouring atomic samples can be studied. Our inspiration is the electronic circuit board, where each junction can individually be designed and micro fabricated on a chip. We want to build such a chip for atoms and light, containing all components needed for the experiment, alignment-free and easy to assemble. In the far future such a chip might form the core of a quantum computer just as the circuit board does for a classical computer.

In the last two decades, tremendous progress has been made in confining the structures necessary for creating magnetic fields onto a chip [12, 13, 14]. Experiments with these "atom chips", here called magnetic chips, have been used to study matter wave interference [15, 16], low-dimensional quantum gases [17], surface interactions [18] and for metrology [19, 20, 21].

More recently scientists started to confine the structures guiding light to and from atoms to a chip. First experiments in this direction used tapered fibres glued to a magnetic chip [22, 23, 24]. Although very successful in detecting small atomic samples down to single atoms, this approach is not easily extended to multiple light-atom interaction regions and still requires a lot of patience and a steady hand to assemble. Our group is the first to successfully pursue the miniaturisation of optical access with a different tool, a photonic waveguide chip. As circuit boards for photons, these chips are made of glass, with paths of higher refractive index than the surrounding material supporting the propagation of light. Details on how these chips are made can be found in chapter 2.

Although new to the field of atomic physics, photonic waveguide chips have long been known to the optics community and become increasingly important in telecommunication as the world wide transfer of information moves from electronic to optical. The world market volume on optical telecommunication technology amounts to a total of 15 billion euros in 2005 (not including optical fibres) and is expected to double by 2015 [25], necessitating further technological developments in the field of optical processing of classical information.

The use of photonic waveguide chips is not restricted to engineering optical telecommunication. Impressive applications of such chips are also reported in fundamental science, ranging from quantum information processing [26] to analysis of liquids [27] and the integration of microfluids as optical components [28]. Since the demonstrated degree of control of light is very useful for detecting and manipulating cold atoms as well, atom optics can benefit from using waveguide chips.

1.1 Our waveguide chip

Our first waveguide chip as shown in figure 1.1 contains twelve parallel waveguides with a rectangular profile of $4\,\mu\text{m} \times 4\,\mu\text{m}$, and a core-to-core separation of $10\,\mu\text{m}$. The electric field of the light propagating in these waveguides has a $1/e$ radius of about $2.2\,\mu\text{m}$ for light at 780 nm as used in our experiments. The waveguides fan out towards the edges of the chip for connection to a fibre array. In the centre of the chip the waveguides are intercepted with a $16\,\mu\text{m}$ wide trench for atomic access (figure 1.1). When we load atoms into the trench, this chip enables us to individually tailor the light at twelve closely spaced points of interaction between atoms and light, which we call atom-photon junctions. The use of these junctions opens new opportunities for probing and controlling ultracold gases. Examples of applications are the direct observation of the propagation of density disturbances in a quantum degenerate gas or Rydberg interactions between elements of an optical dipole trap array. Furthermore, the small size of the light beams improves the quality of a measurement aiming at a minimal disturbance of the atoms.

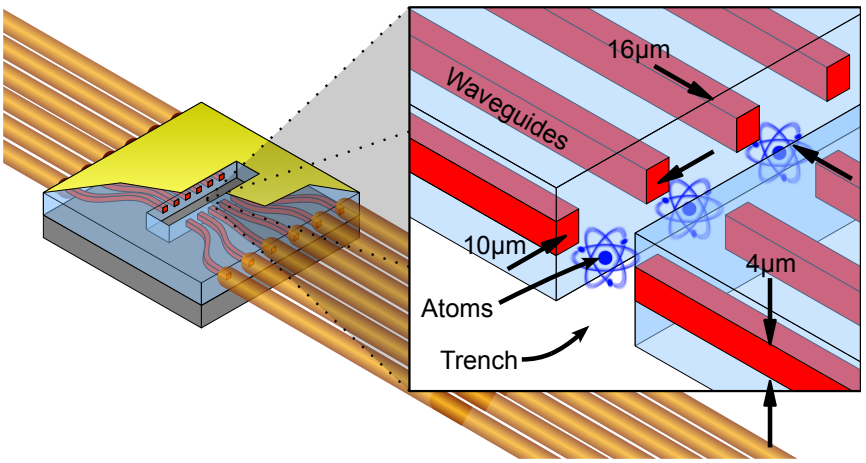


Figure 1.1: Artist impression of our photonic waveguide chip. A silica layer is deposited onto a silicon substrate and coated with a gold layer. The sketch shows six of the twelve waveguides, which fan out towards both ends of the chip, where they are connected to a fibre array. The waveguide are intercepted by a 16 μm wide trench to guide atoms into the light mode. Figure taken from reference [49].

1.2 Optimising measurements

Optimised measurements of atomic densities find application in a variety of experiments. One application, the measurement of temporal correlations, is detailed in chapter 7. Other possibilities include feedback loops [29, 30, 31] to stabilise the atom number in a trap or to damp centre-of-mass oscillations. The accuracy of these measurements depends on the interaction strength between the probe light and the atoms. This strength can be tuned by varying the frequency of the light. However, the more strongly the atoms and light interact, the more photons are scattered. Scattering of photons will cause the atoms to change their internal quantum state or even kick atoms out of the trap. A weakly destructive measurement is therefore always a trade-off between measurement accuracy and the destruction of the measured quantum state [32].

1.2.1 Figure of merit

In our specific case we are looking at measuring the number of atoms in a volume illuminated by a probe beam. The closer we tune the probe light to the atomic resonance and the more photons we use, the more accurately

we can determine the number of atoms in the beam. At the same time scattering of photons will increase the loss of atoms from the trap. To characterise the quality of a measurement we will introduce a figure of merit (FoM) η:

$$\eta^2 = \frac{1}{\rho\sigma_a^2} \tag{1.2}$$

where ρ is the number of photons scattered per atom during the measurement and σ_a is the uncertainty in the measured atom number N_a. Defining the FoM this way makes it independent of both the number of atoms probed and the number of photons detected as we will show in the following. We calculate this FoM for the two different types of measurement: the loss of light power in an absorption experiment and the phase shift of a light beam in an interferometric setup. These are both illustrated in figure 1.2.

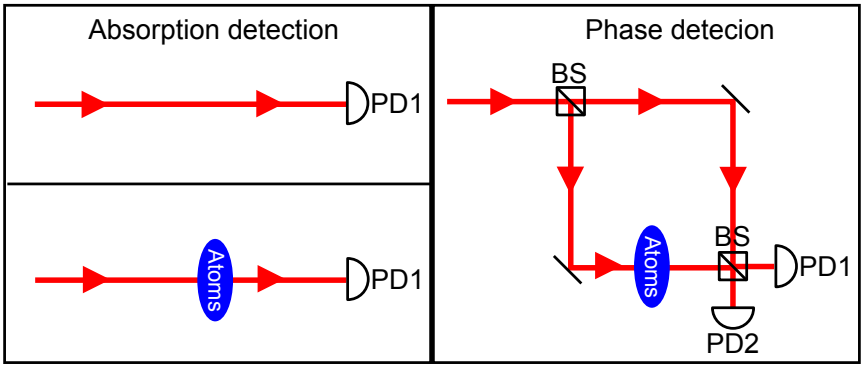


Figure 1.2: Sketch of a setup for detecting the absorption and the phase shift of a light beam passing through a cloud of atoms. In an absorption measurement the light power of a probe beam passing through an atomic sample is compared to the power of the beam when no atoms are present. For measuring the phase shift a reference beam is required, which in this example is provided by splitting the beam on a beam splitter (BS) and guiding one part of the light around the atoms. Both beams are combined on a second BS and interfere.

The power of a light beam passing through a cloud of atoms will be absorbed according to the Beer-Lambert law as $P' = P_0 e^{-\alpha}$, where P_0 is the initial power of the light beam. We can then write the attenuation constant α as a function of number of atoms N_a in a probe beam of area A and frequency ω_L as

$$\alpha = \frac{N_a \sigma_0}{2A} \frac{1}{1+\Delta^2}. \tag{1.3}$$

where $\Delta = (\omega_L - \omega_0)/(\Gamma/2)$ is the detuning of the laser from the atomic resonance ω_0 and Γ is the inverse of the excited state lifetime. When detuned

from the atomic resonance, the light beam will also acquire a phase shift

$$\phi = \frac{N_a \sigma_0}{2A} \frac{\Delta}{1+\Delta^2}. \tag{1.4}$$

For an absorption measurement as illustrated in figure 1.2(a) the figure of merit defined in equation 1.2 is

$$\eta^2 = \frac{1}{\rho \sigma_a^2} = \frac{\alpha}{2N_a} = \frac{\sigma_0}{A} \frac{1}{1+\Delta^2}, \tag{1.5}$$

which can be derived in a few simple steps as presented in the appendix. This FoM is maximal for $\Delta = 0$ where it becomes

$$\eta^2 = \frac{\sigma_0}{A}. \tag{1.6}$$

Instead of detecting the absorption of light one can also detect the fluorescence, that is the photons scattered out of the beam. Here, a reference measurement is not required and the FoM is reduced by the solid angle over which the photons are detected.

In a two-path Mach-Zehnder type interferometer (figure 1.2(b)), the figure of merit is

$$\eta^2 = \frac{1}{\rho \sigma_a^2} = 2\frac{N_a}{\alpha} \left(\frac{\phi}{N_a} \right)^2 = \frac{\sigma_0}{A} \frac{\Delta^2}{1+\Delta^2} \tag{1.7}$$

which takes its maximum for $\Delta \gg 1$ where it approaches

$$\eta^2 = \frac{\sigma_0}{A}. \tag{1.8}$$

The derivation is again detailed in the appendix.

The FoM in both cases can be improved by measuring the reference beam more accurately. In the absorption measurement this can be done by measuring the reference beam several times, in the interferometer measurement by increasing the intensity of the reference beam.

In our experiments we measure the differential phase shift of two frequencies in a single light beam using a phase-sensitive detector. A derivation of the figure of merit for this kind of interferometer can be found in chapter 6. In the limit of equation 1.8 we get

$$\eta^2 = \frac{\sigma_0}{A}, \tag{1.9}$$

which is a factor of two worse than the corresponding result for the Mach-Zehnder interferometer. This reduction is due to the fact that a phase-sensitive detector amplifies noise and amplitude slightly different, as I will explain in chapter 6.

1.2.2 Summary

Phase-shift and absorption measurements experience the same fundamental limit when it comes to comparing the minimum uncertainty per scattered photon. These results show that measurements of a phase are not superior to measurements of absorption for a weakly destructive detection of the atom number. The maximum FoM is in fact identical in both cases. The real gain of the phase shift measurements is revealed when considering the measurement of an optically thick atomic sample, where a resonant measurement would lead to multiple scattering of single photons and therefore to a reduction of the FoM. The phase shift measurement on the other hand shows its best performance when the light is tuned far away from the atomic resonance and the optical thickness can be adjusted.

This thesis presents measurements of both types. When we detect atoms with the waveguide chip (chapter 5) we infer the atomic density from the absorption of resonant light. In chapter 6 I present a technique for detecting atoms via the phase shift they imprint on the beat note of a frequency-synthesised light beam.

A phase-sensitive measurement employing a phase-sensitive detector performs slightly worse than a phase measurement with a Mach-Zehnder interferometer. Its advantages in terms of stability, ease of setup, required space on the experimental site, low maintenance and small back-action on the probed sample makes it, however, superior in certain experimental conditions.

The FoM scales inversely with the beam area. This shows one of the key advantages of probing cold atoms with micro-fabricated optics. The small probe beam from the waveguides minimises the uncertainty in the measured atom number for a fixed number of scattered photons.

1.3 Contents of this thesis

This thesis starts by introducing waveguide chips, explaining the different manufacturing processes in general and the requirements for a chip in a cold atoms experiment in particular. Furthermore, I describe how light modes in a waveguide can be calculated and motivate the specific design of our chip. Chapter 3 outlines the theory of the most central physical process of this thesis, the interaction between light and atoms. After a quick overview of our experimental setup and the standard techniques used to trap and cool neutral atoms, the experimental results are described in two parts. The first part describes measurements on the interaction of light in a multichannel waveguide chip with cold atoms. The second part describes measurements of the density of an atomic cloud by the differential phase shift between two frequency components of a probe beam after passing through the cloud. A possible applications for using the frequency-synthesised probe light on a photonic waveguide chip is outlined in chapter 7. Here, I calculate temporal correlation functions in ultracold gas and explore the possibility of measuring these correlations with our apparatus.

2 Photonic waveguide chips

Photonic waveguide chips are circuit boards for light. They offer the possibility of information processing in a scalable way and can be a building block for scalable atom traps. The equivalent of conducting paths on these chips are regions of higher refractive index in a surrounding of lower refractive index. Our chips were manufactured at the Centre for Integrated Photonics (CIP) in Ipswich, UK. Starting with a 0.5 mm thick silicon wafer, a layer of 10 μm of undoped silica is deposited by thermal oxidation. A second layer of boron- and germanium- doped silica is deposited by flame hydrolysis and etched through a UV-lithography mask to form the cores of the waveguides. These cores have a square cross-section of $(4 \times 4)\mu\text{m}^2$. A further layer of silica doped with boron and phosphorus, deposited by flame hydrolysis, concludes the waveguide structure. The doping is necessary to match the refractive index of the lower cladding, since flame hydrolysis and thermal oxidation give the silclia different refractive indices. The chip is coated with 50 nm of chrome and 100 nm of gold, which is of use for trapping atoms near the surface. A trench is cut in the centre of the chip by deep reactive ion etching. The trench has a cross-section (width $\times$ length) of 16 $\mu\text{m} \times 500\,\mu\text{m}$ and is 22 μm deep. Finally, the end facets of the chip are polished to minimize coupling losses.

On our chip, the index contrast is produced by different doping for different layers. Alternatively, waveguides can directly be written with high energy radiation focussed into bulk material. This has been done using short laser pulses in different kinds of glasses [33] or UV light in doped, photosensitive glasses as pioneered by Svalgaard and co-workers [34]. While these techniques provide a much faster and more flexible way of producing waveguide chips, the refractive index contrast achievable is smaller compared to doped material. A large index contrast, however, is required for a small beam area. Further advancement in the field of direct-written waveguides will surely enhance the refractive index contrast achievable and those

waveguides will become an option for future atom optics experiment.

This chapter begins with a brief description of how light modes in such a waveguide chip can be calculated. The numerical solutions for the general equation are found and approximations for some experimental circumstances are given. These results motivate the dimensions we chose for our waveguides. Finally, I will describe the experimental procedure used to connect the waveguide chip to optical fibres for use in an ultra high vacuum (UHV) chamber.

2.1 Propagation of light in an optical waveguide

We want to calculate the mode profile of a beam propagating along z through a waveguide with refractive index profile $n(x, y)$. Neglecting the (small) losses in the medium, we take n to be real. Furthermore, we assume that the refractive index variation is small, so that weak-guiding theory is applicable. With these approximations we can neglect polarisation and write the electric field as a scalar quantity E, satisfying the wave equation:

$$\nabla^2 E - \frac{1}{v_{ph}^2}\frac{\partial^2}{\partial t^2}E = 0, \tag{2.1}$$

where $v_{ph} = c/n$ is the phase velocity of the electro-magnetic wave in the medium. We are looking for the steady state mode profile $E(x, y)$ for a wave propagating along z with a component of the wave-vector along this axis of $k_z = \omega/v_{ph}$, where ω is the angular frequency of the light. The electric field with local wave number $k(x, y) = \omega/(c/n(x, y)) = k_0 n(x, y)$ can now be written as

$$E(x, y, z, t) = \tilde{U}(x, y)e^{\mathrm{i}\omega t - \mathrm{i}k_z z}, \tag{2.2}$$

and the derivatives for t and z in the wave equation can be executed:

$$\left(\frac{\partial^2}{\partial x^2} + \frac{\partial^2}{\partial y^2} + n(x, y)^2 k_0^2 - k_z^2\right)\tilde{U} = 0. \tag{2.3}$$

In the most general case, this partial differential equation needs to be solved numerically.

An efficient way to do so is demonstrated by S. Hewlett and F. Ladouceur [35]. The main idea is to expand the electric field into a Fourier series. To prop-

erly account for the boundary conditions, the infinite x-y plane is mapped onto the unit square and the Fourier decomposition is done in the transformed coordinates. In transformed coordinates u and v the field is decomposed into N^2 Fourier components:

$$\tilde{U}(u,v) = 2\sum_{m=1}^{N}\sum_{n=1}^{N} a_{m,n}\sin(m\pi u)\sin(n\pi v) \tag{2.4}$$

Plugging this series expansion into equation 2.3 transforms the differential equation into an eigenvalue problem, which can readily be solved using standard routines.

The authors call their method the modified Fourier decomposition method (MFDM) to set it apart from earlier Fourier decomposition methods which do not use the mapping to the unit square. The modified method shows very good convergence, e.g. the electric field for the LP_{11} mode of a multimode square waveguide differs by less than 0.1 % from that obtained with a finite element method for $N = 25$.

In principle we can also use the solution to calculate the cross coupling between adjacent waveguides and the bend loss [36]. However, both are smaller than the numerical precision provided by 32 bit floating point arithmetic and therefore negligible. In the laboratory we do measure a cross coupling of the order of 10^{-4} between neighbouring channels, but this is mainly caused by light coupling directly from the supply-fibre into the glass layer which eventually couples into the second waveguide.

Where appropriate, we will approximate the waveguide mode by a Gaussian as shown in figure 2.1, which makes calculations analytically tractable. Deviations from the numerical treatment are less then a few percent, which makes the Gaussian sufficiently accurate for our purposes.

Experimentally the mode size is determined by measuring the divergence angle of the light in the far-field. A Gaussian profile

$$I(x,y) = I_0 e^{\frac{2(x+y)^2}{w^2}} \tag{2.5}$$

is fitted to the intensity profile $I(x,y)$ measured by a CCD camera. The camera is mounted on a translation stage and is moved between images by a known distance Δz in the direction of beam propagation z. To each image we fit a Gaussian profile of width w and determine the change in this width

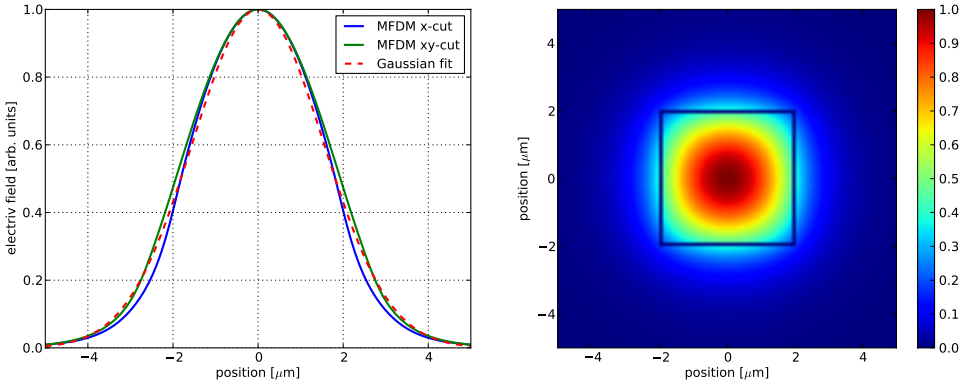


Figure 2.1: The right image shows the intensity profile of the waveguide mode obtained with a Fourier decomposition method as explained in the text. The left graph shows a cut through that intensity profile in horizontal ($y = 0$ and diagonal ($x = y$) direction. It also show the Gaussian profile that matches the two cuts best. The fitted width parameter w_0 is 2.18 μm in agreement with the far field measurements.

between images Δw. If the images are taken at distances from the focus that are much larger than the Rayleigh range z_R (see below), $\Delta w/\Delta z$ is constant and can be used to calculate w_0:

$$\frac{\Delta w}{\Delta z} = \frac{\lambda}{\pi w_0} \tag{2.6}$$

The result $w_0 = (2.2 \pm 0.1)\ \mu$m agrees with the expectations obtained from the Fourier expansion.

The simulation shows that higher-order modes are not supported in the waveguides at a wavelength of 780 nm. This was experimentally confirmed by moving a fibre along the input plane of the waveguide chip. The intensity profile of the light beam leaving the waveguide is then recorded on a CCD camera and examine for asymmetric deviations from a Gaussian profile. Since such asymmetries could not be observed we can exclude contributions of higher-order modes within the measurement precision.

2.2 Mode matching between fibres and waveguides

The electric field $E(x, y, z, t)$ of a freely propagating electro-magnetic wave satisfies the wave equation 2.1. For a wave propagating with a wave number $k = \omega/c$ as $E(x, y, z, t) = U'(x, y, z) \exp(\mathrm{i}ckt)$ the wave equation becomes

the Helmholtz equation

$$\nabla^2 U' + k^2 U' = 0 \tag{2.7}$$

The electric field can be decomposed into the fast-varying oscillation with the wavelength of the light and a slowly-varying envelope. If we take the wave to propagate along the z axis we can write this as $U'(x, y, z) = A(x, y, z) \exp(-\mathrm{i}kz)$. For points close to the z axis, $\partial A/\partial z \ll kA$. In this paraxial approximation the Helmholtz equation for the envelope becomes:

$$\left(\frac{\partial^2}{\partial x^2} + \frac{\partial^2}{\partial y^2}\right) A - 2\mathrm{i}k\frac{\partial}{\partial z}A = 0, \tag{2.8}$$

which is called the paraxial Helmholtz equation. A solution of this equation is the Gaussian beam, whose complex amplitude can be written as [37]:

$$U(r, z) = E_0 \frac{w_0}{w(z)} \exp\left(-\frac{r^2}{w_0^2}\right) \left(-\mathrm{i}kz - \mathrm{i}k\frac{r^2}{2R(z)} + \mathrm{i}\zeta(z)\right). \tag{2.9}$$

Here, E_0 denotes the peak electric field amplitude, z is the propagation direction of the light beam, $r^2 = x^2 + y^2$ is the perpendicular distance from the propagation axis and w_0 is the minimal width of the mode at $z = 0$. The width of the mode at position z is $w(z) = \sqrt{1 + (z/z_R)^2}$, with the Rayleigh range $z_R = \pi w_0^2/\lambda$. The radius of curvature is $R(z) = z\,(1 + z_R/z)^2$ and the longitudinal phase shift (Gouy phase) is $\zeta(r) = \arctan(z/z_R)$. In contrast, a guided mode is a mode that does not diverge, i.e. the electric field profile is $U(r, 0)$ for all z.

To calculate the mode overlap between the fibre mode and the mode in the waveguide, we will approximate the mode field of the waveguide with a Gaussian profile $U_w(r, 0)$ of radius w_w

$$U_w(r, 0) = E_0 \exp\left(-\frac{r^2}{w^2}\right). \tag{2.10}$$

This makes the problem radially symmetric. In the single-mode fibre that brings the light to the waveguide, the Gaussian mode field $U_f(r, 0)$ has some other radius w_f. When light is coupled from the fibre into the waveguide and vice versa we expected the fraction of power transmitted to be proportional

to the mode overlap

$$\eta = \frac{\left(\int_0^\infty r dr U_f(r,0) U_w(r,0)\right)^2}{\int_0^\infty r dr U_f^2(r,0) \int_0^\infty r dr U_w^2(r,0)} = \frac{4 w_f^2 w_w^2}{\left(w_f^2 + w_w^2\right)^2}. \tag{2.11}$$

2.3 Transmission through the trench

A central part of our experiments is the interaction between light from the waveguides and an atomic cloud. To bring atoms into the light mode the waveguides are intercepted by a trench as shown in figure 1.1. Light leaving a waveguide on one end of the trench will diverge in the trench and only some of the light will couple into the waveguide mode on the other end. To calculate how much of the light reaches the waveguide mode after passing through a trench of width l, one might be tempted to just calculate the latter expression for $w(0)$ and $w(l)$. However, the imaginary part of the electric field accounts for a phase shift for points with equal z and different r. This phase shift leads to a curvature of the wave front, which is maximal at the Rayleigh range z_R. On our chip $l \approx z_R$ and the mismatch between the phase of the light wave and the constant phase of the waveguide mode significantly reduces the transmission (cf. figures 2.2 and 2.3). The full complex integral

$$\eta = \frac{\left(\int_0^\infty r dr U_w(r,0) U_w(r,l)\right) \times c.c.}{\left(\int_0^\infty r dr U_w(r,0) U_w^*(r,0)\right)^2} = \frac{1}{1 + \left(\frac{\lambda l}{2\pi w_0^2}\right)^2} \tag{2.12}$$

gives a transmission of 85 % across the 16 μm trench of the chip due to the mode overlap. The real integral 2.11 gives a transmission of approximately 94 %. Additionally, there are Fresnel losses on the waveguide-air and air-waveguide interfaces. The transmission T through each interface is [37]

$$T = \frac{4 n_a n_w}{(n_a + n_w)^2}. \tag{2.13}$$

With the refractive indices $n_a \approx 1$ of air and $n_w \approx 1.46$ of the waveguide cores the transmission is about $T \approx 96.5\,\%$.

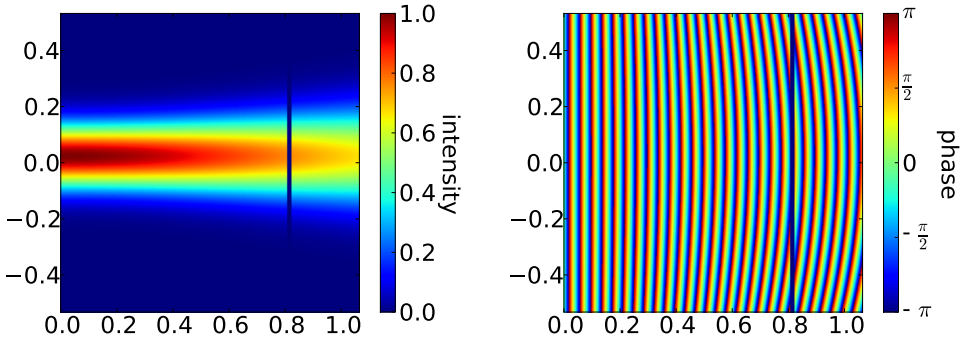


Figure 2.2: Intensity (left) and phase (right) of a freely expanding Gaussian beam. The axis are in units of the Rayleigh range z_R. 0 corresponds to the position of the first waveguide. The light then freely diverges in the trench. The black vertical line indicates the position of the second waveguide where the light leaves the trench.

2.4 Waveguide chips for atom-optical experiments

Using the waveguide chip for manipulating and detecting atoms sets some restrictions on the parameter space for the chip dimensions. First, the wavelength has to match the atomic transition, which is in our case 780 nm. Since this is substantially shorter then the standard Telecom wavelengths which are above 1200 nm, we have to customise our layout in terms of waveguide dimensions and refractive index contrast. Second, we want the light mode to be small to probe small sub-samples of the atomic cloud. This can only be achieved by using a relatively large refractive index contrast, which limits us to lithographically fabricated chips. Third, the width of the trench is a trade-off between loss due to divergence of the beam and space for atomic access. Furthermore, the width is chosen so that diverging beams from both sides of the trench can produce an intensity maximum in the centre with sufficient gradients to trap atom by the optical dipole force. Depth and width of the trench are then chosen to give room for cigar-shape clouds of atoms with a circular cross section and large aspect ratios as they are produced by our magnetic subchip as explained in chapter 4.

2.5 Connecting the chip

2.5.1 Practical considerations

Light is supplied to the waveguides using 12 fibres assembled on a V-groove assembly (VGA) as shown in figure 2.4(5). The fibres (figure 2.4(6)) are

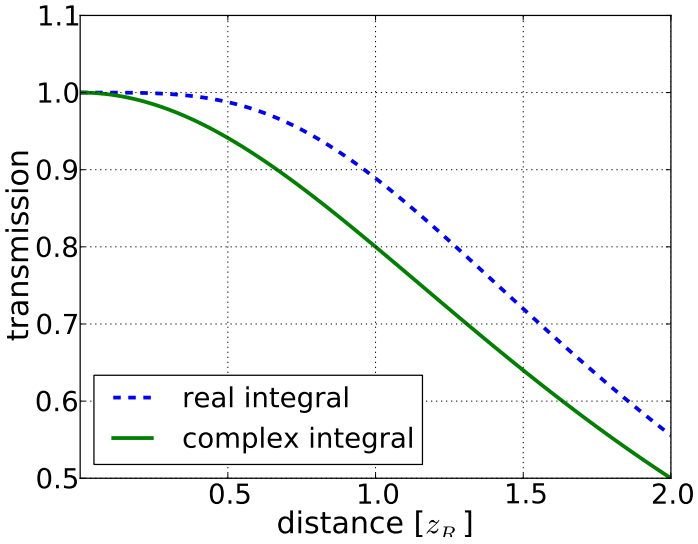


Figure 2.3: Comparison of the transmission calculated from the real and complex integral. For $l = z_R$ the loss taking the phase mismatch into account is approximately 10 % larger then the pure intensity overlap.

single mode at 780 nm with a 5 μm core and 125 μm cladding. The VGAs are commercially available from OZ optics. To prepare the setup for the use in an atom optic experiment a permanent connection between fibres and waveguide chip has to be established. This connection must withstand temperature fluctuations between room temperature and at least 100 °C. The high temperature end of the range is reached while baking the vacuum chamber to achieve ultra high vacuum (UHV).

To establish this permanent connection, the choice of an appropriate glue is crucial. The glue has to be transparent to the light used in the experiment, with a refractive index close to those of waveguides and fibres. It must have a low outgassing rate, as it is part of a UHV system with pressures well below 10^{-10} torr. Furthermore, the glass transition temperature above which the glue disintegrates should lie well above 100 °C. Experiments showed that exceeding this temperature causes the fibres to move so far that the coupling of light into the waveguide is destroyed. A low thermal expansion is a further requirement for the junction to survive high temperatures. After moderate success with Epotek-353ND, we now use Epotek-OG116, mainly because of its higher glass transition temperature. Additionally, switching from heat-curing to UV-curing glue simplified the assembly, since the curing process is

much faster and realignment during curing is hardly necessary. The values of the relevant parameters taken from the Epotek OG-116 data sheet can be found in table 2.1.

When using UV glue, special care has to be taken that the UV light can reach all of the applied glue, since uncured glue reduces the mechanical stability and contributes to outgassing. Since the waveguide chip and V-groove assembly are transparent only on the top side, optical access for the UV light requires the V-grooves to be glued upside down to the chip. The lower image of figure 2.4 shows the interface between V-groove assembly (5) and waveguide chip (7). The transparent lid of the V-groove assembly (a) and the silicon substrate of the chip face each other, as well as the silicon substrate of the V-groove assembly (b) and the silica surface of the waveguide chip.

2.5.2 Alignment

The alignment setup is shown in figure 2.4. A clamp was designed that can hold the V-groove assembly (VGA, figure 2.4(5)). It is attached to a Thorlabs prism mount (KM100P, figure 2.4(4)) and a micro positioning stage (MAX312D, figure 2.4(1)) for rotational and translational alignment, respectively. This leaves just one final rotational degree of freedom that cannot be controlled. To describe the alignment, I will make use of a coordinate systems where the x-axis points along the waveguides and the y-axis is parallel to the direction of gravity as shown in figure 2.4. I will use the Tait-Bryan angles to describe rotations, where the yaw angle describes a rotation around the y-axis, pitch around the z-axis and roll around the x-axis.

The waveguide chip (figure 2.4(7)) in the centre is mounted on a dummy subchip (figure 2.4(3)). At the top of the image is a microscope objective

Property	Value	Unit
Glass transition temperature	146	°C
Thermal expansion	54×10^{-6}	$°C^{-1}$
Refractive Index	1.54	
Spectral transmission @ 780 nm	> 0.98	

Table 2.1: Properties of Epotek-OG116, taken from preliminary data sheet.

(figure 2.4(2)) used for diagnostics during alignment.

The angle that cannot be adjusted is the pitch angle. However, a small tilt along this angle does not seem to have major influence on the coupling. The alignment along this axis is good enough, if the VGA is rested on the waveguide chip before being picked up from the top with the clamp. The yaw angle can be observed through the microscope looking down onto the chip, since it is in the plane of view. Aligning can therefore be done by observation. The roll angle can be adjusted once light transmission through two spatially separated channels is detected. A misalignment in the roll angle will lead to a different position of maximum transmission for the two channels when moving the translation stage in y direction. Changing the roll angle until the maximum of both transmissions occur at the same y position allows a very precise alignment. It is not possible to optimise the coupling in all channels simultaneously because the fibres are not perfectly aligned in the V-grooves but the position of the cores differ from one to another.

Once the optimum alignment is found, the VGAs are glued in place with a droplet of glue on the VGA surface facing the waveguide chip. The amount of glue is chosen carefully (just a small droplet) so that a thin homogeneous layer of glue will be established when the VGA is pushed against the waveguide surface. This forms a bond between the two surfaces. Too much glue on the other hand will not cure properly, resulting in the aforementioned drawbacks for the experiment.

After gently pushing the VGAs against the waveguide chip, the glue is cured by shining UV light onto the interface from the top, the rear left and the rear right subsequently (directions as seen in direction of light propagation). When curing from the rear, the angle between the UV lamp and the fibres is kept as small as possible so that the interface is properly illuminated through the glass lid of the VGA. The UV lamp is switched on twice for 400 s in each of the three positions. The light power transmitted through the fibre/waveguide channels is constantly monitored and found to be very stable. Readjustment is therefore not necessary.

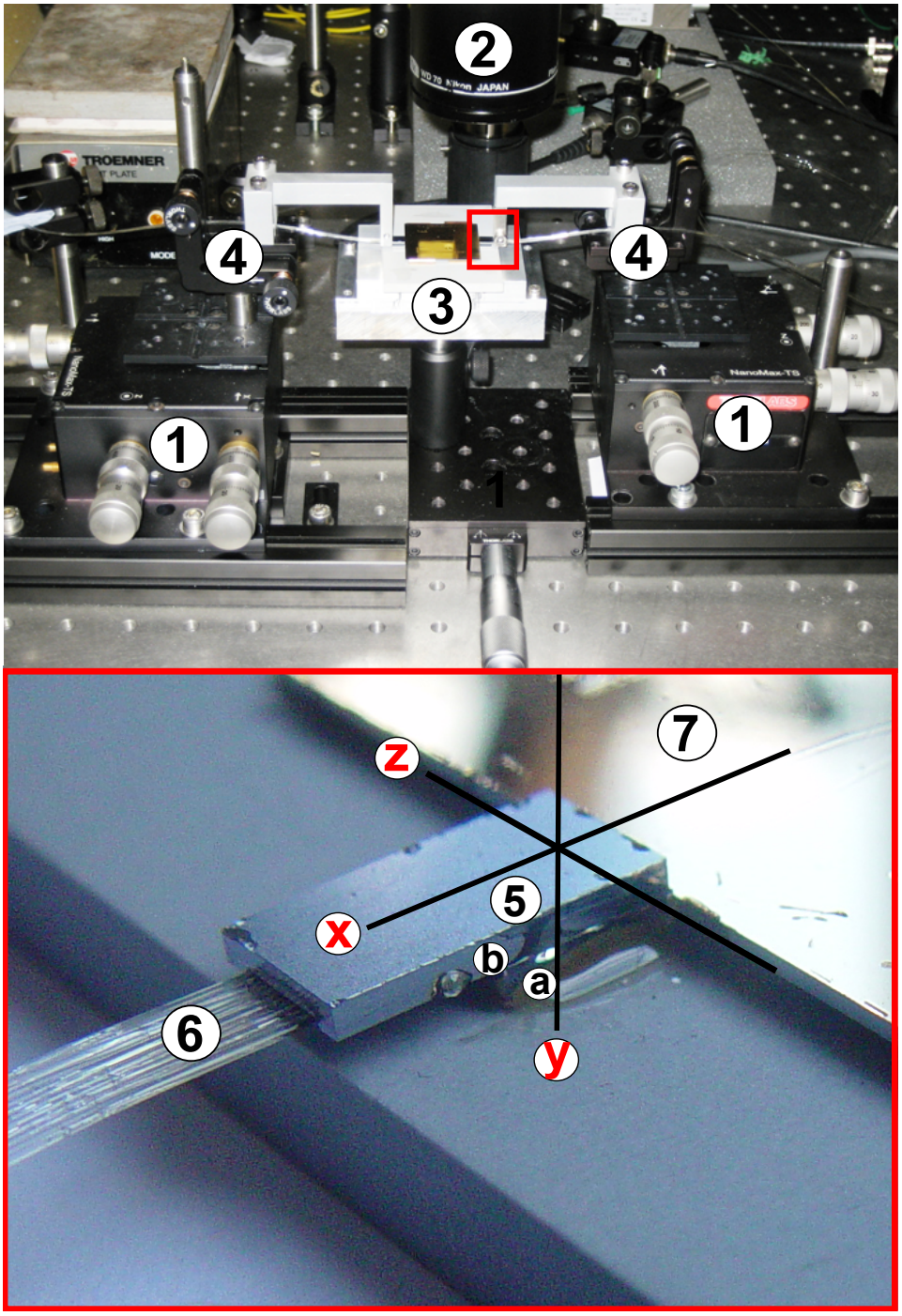


Figure 2.4: Alignment stage for connecting the V-groove assemblies to a waveguide chip. Clamps mounted on a prism mount (4) hold the V-groove assemblies (5) consisting of transparent lid (a), silicon base (b) and fibres (6) in place. The waveguide chip (7) is mounted on a dummy subchip (3). Translational adjustment is done using micro positioning stages (1). For visual inspection a microscope objective (2) is used. The lower picture shows a zoom on the waveguide-fibre interface on the chip after assembly (clamps removed).

2.5.3 Testing the thermal stability

After curing the glue, the setup is mounted on a hot plate and several heating tests are preformed. Initially, the temperature of the waveguide chip is cycled between 130 °C and room temperature. These cycles are repeated more than 10 times in the course of 24 h. Afterwards, the setup is held at 120 °C for a further 24 h period. After cool-down, the transmission through the setup is found to be within 10 % of the value it had before the test. Values can be found in chapter 5.

We tried adding glue between the glass lid of the VGA (figure 2.4(5a)) and the subchip to increase the stability of the setup. Repeating the heating cycles showed no major differences, therefore the additional glue was not used for the final chip. To account for long-term drifts in laser power and fluctuations in coupling from the free-space laser beam to the waveguide, we did a reference measurement monitoring the transmission of the chip kept at room temperature over 24 h.

Glueing the waveguide chip and experimental history

Thermal stress is a major risk. Therefore, the way the chip is glued to the subchip must be considered carefully. The first waveguide chip was glued onto an aluminium block with two drops of heat-curing Epotek H74. The glue was cured at 150 °C. Thermal stress, however, forced the chip to shatter after a couple of days. The next chip was glued with a single drop of glue in the centre. The VGAs were attached with one layer of glue between VGA and waveguide chip and additionally enforced with glue between VGA and subchip. When this setup was heated a few degrees above room temperature, the coupling was completely lost, due to a combination of uncured glue and thermal stress. After this second attempt, the V grooves where turned upside down as described above for UV light access and the curing time was doubled. The dummy subchip was updated to closer match the real chip by glueing copper plates on top. The copper plates are separated by a trench. A single drop of glue was used on each of these plates to attach the waveguide chip and cured between 120 °C and 130 °C. The gap between the plates helped reducing thermal stress and the setup finally survived the thermal cycles successfully.

2.5.4 Placing the chip in vacuum

The optical fibres are fed through into the vacuum via Teflon ferrules in a Swagelok connector, similar to the ones developed in the group of Eric Cornell [38]. Each Teflon ferrule contains 6 holes, 300 μm in diameter. The fibres with their jacket on have a diameter of 250 μm. When the Teflon is compressed in a standard Swagelok connector, a seal is produced that is good enough to reach pressures below 2×10^{-10} torr in the vacuum chamber. This pressure was reported by Eric Cornell [38]. Although our chamber is at a higher pressure, we do not see any limitations due to the optical feedthroughs. Even with a helium leak detector we could not detect any leaks down to a rate of 10^{-10} torrl/s. We did notice, however, that the Swagelok connectors became loose while baking the chamber and had to be tightened afterwards.

2.5.5 Results

The transmission across the two fibre-waveguide junctions and the trench are measured for each channel on a test assembly as well as on the final chip under vacuum. The transmission on the test chip after heating tests varies in the range of 10 % - 35 %. In a separate setup with a different chip, transmission across the trench was measured to be around 55 % which comprises the mode overlap, Fresnel reflection and the roughness of the trench sides. A further reduction by a factor of 0.8 on each waveguide-fibre interface due to mode mismatch leads to the measured 35 % transmission. Variations are due to variations in the position of the fibres in the V-grooves.

On the final chip, a copper piece extends a few tens of microns beyond the chip edge on one side. The V-groove assembly therefore can not be placed as close to the chip as needed for maximum coupling on this side. The net transmission of the middle 10 channels of the final chip varies between 4 % and 8 %. The transmission through the first channel is only 2 % and therefore slightly worse, whereas the twelfth channel has almost no transmission on one of the fibre-waveguide interfaces. The total transmission through this channel is on the order of 10^{-5}.

3 Atom-Light interaction

To measure atomic densities we detect a light beam after interaction with the atomic sample. To infer the atomic density from this light beam, the interaction between the atoms and the light field has to be well understood. This is certainly the case for the simplest situation of two level atoms in a monochromatic light field (see e.g. [39]). Considering all relevant levels of a ^{87}Rb atom complicates the situation, but there is still literature available that deals with this problem (e.g [40]). We do experiments in which the atoms are detected with a light field consisting of more than one frequency component (chapter 6). Here, numerical simulations have to be employed. This chapter reviews a textbook approach for the multi-level atom in a monochromatic light field as it can be found in [41] and extends it to include more than one light frequency. The resulting equations can be solved numerically.

The state of the atomic ensemble is described by its density matrix [42]. The time evolution of the density matrix is given by the Heisenberg equation. We will first construct the system Hamiltonian treating the light field classically. This approximation is valid because each mode of the input light field will contain enough photons that the emission or absorption of a single photon into that mode does not significantly change the dynamics of the system. The light field is taken to contain several frequencies closely spaced around a centre frequency ω_a in a way that the frequency differences δ_k between the frequencies are much smaller than the central frequency.

This semi-classical approach neglects the effect of spontaneous emission, as photons can be emitted into all available modes of the vacuum. However, the changes of populations and coherences due to this effect are well known from the Wigner-Weisskopf theory [43] (see e.g. [44] for a more pedagogic derivation). This part of the population change is independent of the laser field. To treat the problem numerically these changes are written in matrix form and added to the coherent evolution. The Heisenberg equation then

becomes a Lindblad type master equation [45].

The time evolution of the density matrix can then be found by integrating the Lindblad type master equation using standard numerical routines. We can calculate the refractive index of the atomic ensemble from the density matrix and use this to calculate the change of the light field. The resulting equations are shown to recover the correct expressions when restricting the problem to two- or multi-level atoms in a monochromatic light field.

3.1 Atomic Hamiltonian

The atoms used in our experiment are ^{87}Rb atoms. As an alkali metal each atom has one valence electron, whose quantum state is described by the principle quantum number and the state vector $|\Lambda\rangle = |L, J, F, m\rangle$ (figure 3.1). All other electrons are in completely filled shells and do not contribute to the total angular momentum of the atom. In its ground state, the valence electron has a principle quantum number of 5. In all our experiments the electron will not change its principle quantum number. The transitions we address are transitions between states of different orbital angular momentum quantum numbers L, namely $L = 0$ to $L = 1$, with transition frequencies in the near infra-red. The spin of the electron can be oriented either parallel or anti-parallel to the orbital angular momentum, splitting the state with $L = 1$ into two states with different total angular momentum of the electron. The quantum numbers of these states are $J = 1/2$ and $J = 3/2$, called the fine-structure quantum numbers [46]. Transitions from the $L = 0$ ground state to these two states are called the D_1 and D_2 line, respectively. In our experiment we address only the D_2 line.

Because the angle between the total angular momentum of the electron and the angular momentum of the nucleus I_n can take different values, each state of the fine structure exhibits a hyperfine structure, characterised by the quantum number F, which runs from $I_n - J$ to $I_n + J$ in steps of 1. The angular momentum of the nucleus of ^{87}Rb is $I_n = 3/2$. Finally, the alignment of the total angular momentum with an external magnetic field gives rise to a Zeeman substructure of the hyperfine states, characterised by the quantum number m, which runs from $-F$ to F in steps of 1.

In summary, we consider transitions between the Zeeman hyperfine states $|\Lambda\rangle = |0, 1/2, F, m\rangle$ (or $5^2\mathrm{S}_{1/2}$ in standard spectroscopic notation), subse-

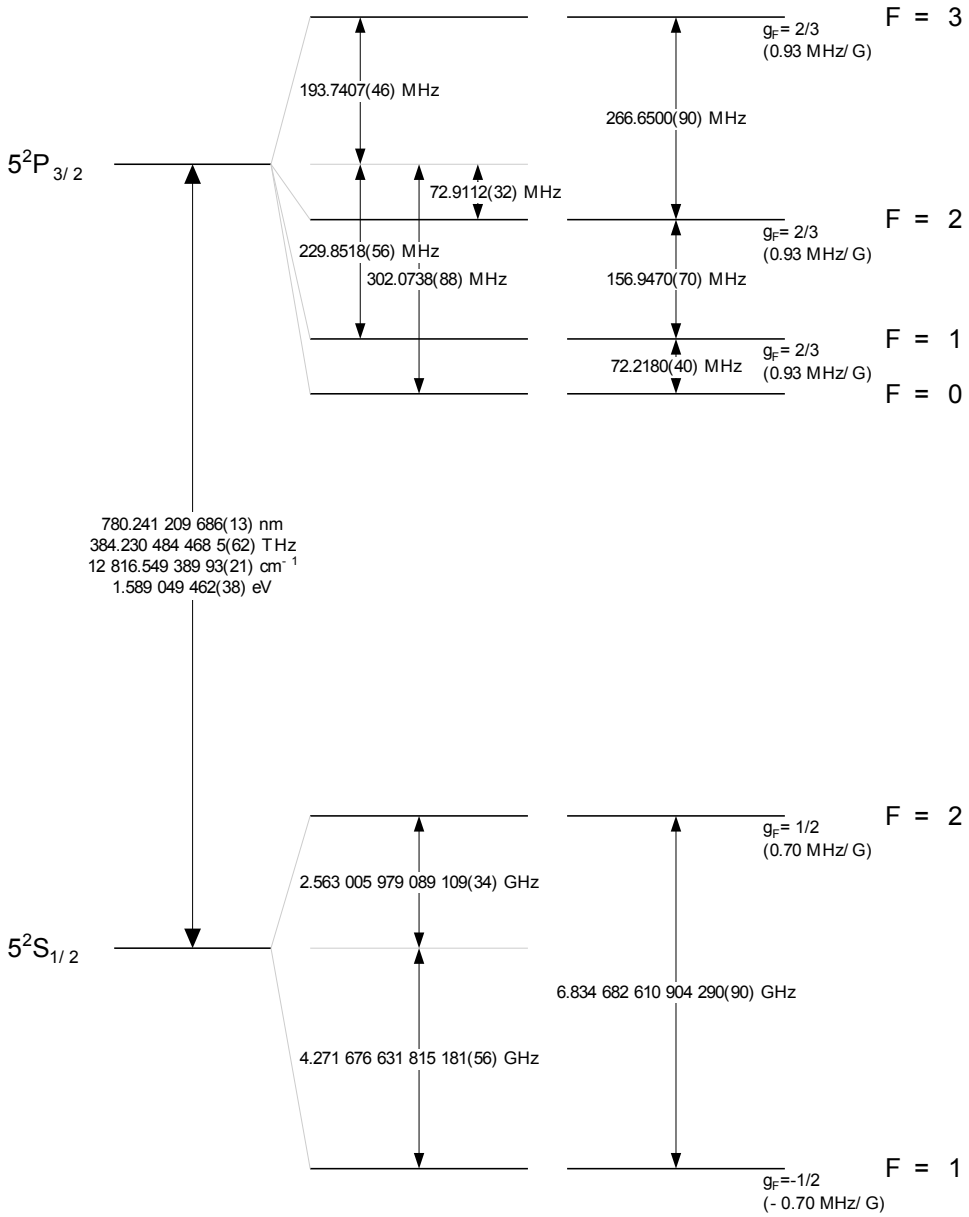


Figure 3.1: Energy differences between the ground and excited states hyperine levels of the ^{87}Rb D_2 line. The splittings are to scale within each manifold, but different for each manifold and for the optical transition. Along with the energies the Landé factors g_F and the corresponding magnetic moment $g_F\mu_B/\hbar$ are given. Not shown are the Zeeman sublevels of the hyperfine states, which are degenerate when no external magnetic field is present. Figure taken from reference [1].

quently called ground states, and the $|\Lambda'\rangle = |1, 3/2, F', m'\rangle$ ($5^2P_{3/2}$) states, which will be called excited states. All other transitions are far detuned from the light field and will only contribute negligibly to the state evolution.

The state of an ensemble of atoms can be described using the density operator

$$\hat{\rho} = \sum_j p_j \, |j\rangle \, \langle j| \tag{3.1}$$

where the $|j\rangle$ are a set of pure states completely describing the state of the ensemble, and p_j is the probability of finding the system in that state ($\sum_j p_j = 1$). In a chosen basis set, here the atomic states $|\Lambda\rangle$, the matrix elements ρ_{kl} are easily calculated as $\rho_{kl} = \langle \Lambda_k | \hat{\rho} | \Lambda_l \rangle$. The time evolution of this operator in the absence of dissipation is given by the Heisenberg equation:

$$\dot{\hat{\rho}} = -\frac{i}{\hbar} \left[\hat{\rho}, \hat{H} \right], \tag{3.2}$$

where $\hat{H}$ is the Hamiltonian operator of the system. In the semi-classical limit we neglect quantum fluctuations of the light field. The Hamiltonian consists of the bare atom Hamiltonian $\hat{H}_a$ and the interaction Hamiltonian $\hat{H}_{int}$.

The Hamiltonian of the free atom is

$$\hat{H}_a = \sum_j \hbar\omega_j \, |\Lambda_j\rangle \, \langle \Lambda_j| \tag{3.3}$$

Here, Λ_j runs over all atomic states in the basis and $\hbar\omega_j$ is the energy of the jth state. The mean angular frequency ω_a of the D_2 line is the average transition frequency between the ground and excited state manifold, where every hyperfine state is weighted by its $2F + 1$ degeneracy. Setting the weighted average of the ground state as the zero of energy, the transition angular frequency of each state ω_j is the sum of the hyperfine shift δ_F, the Zeeman shift $\delta_Z(B, \Lambda)$ of the magnetic sublevels in a magnetic field B and — for the the excited states — the transition angular frequency of the D_2 line. The Zeeman shift is

$$\delta_Z(B, \Lambda) = m \, g_\Lambda \, \mu_B \, B \tag{3.4}$$

where g_Λ is the Landé factor for the respective hyperfine level [1], which not only depends on the hyperfine-structure quantum number F, but also on the angular momentum of the electron L and the fine-structure quantum number J. With these definitions the atomic operator can be written as:

$$\begin{aligned}\hat{H}_a =&\hbar \sum_{\Lambda'} \left[\omega_a + \delta_{F'} + \delta_Z(B, \Lambda')\right] |\Lambda'\rangle \langle\Lambda'| \\ &+ \hbar \sum_{\Lambda} \left[\delta_F + \delta_Z(B, \Lambda)\right] |\Lambda\rangle \langle\Lambda| \,, \end{aligned} \tag{3.5}$$

where we denote the ground states with $|\Lambda\rangle$ and the excited states with $|\Lambda'\rangle$.

3.2 Interaction with the electric field

We only consider electric dipole transitions, whose Hamiltonian is given as the scalar product of electric field and atomic dipole operator $\hat{H}_{int} = \hat{\mathbf{d}}\mathbf{E}$. The amplitude of the electric field can be written as $E = \sum_k E_k \cos(\omega_k t)$, with E_k and ω_k being the peak electric field and the frequency of the k-th frequency component, respectively. We will take the direction of the local magnetic field as the quantisation axis and write the polarisation p_k of each light mode in the basis of atomic transitions as a set of three real numbers. The numbers are equal to the proportion of light power in the beam that drives σ^- ($\Delta m = m' - m = -1$), π ($\Delta m = 0$) and σ^+ ($\Delta m = +1$) transitions ($p_k = \left(p_-^k, p_0^k, p_+^k\right)$, $p_-^k + p_0^k + p_+^k = 1$). Expressing the polarisation components of the light field in the reference frame of atomic transitions account for all effects of the alignment of the atomic dipole moments with respect to the electric field.

The dipole moment can be calculated from the integral over the charge distribution. The reduced dipole moment for the D_2 line is [1]

$$d_2 = \langle J = 1/2 \parallel \hat{d} \parallel J' = 3/2\rangle = 4.22753(78)\, e a_0. \tag{3.6}$$

The relative strengths of the transitions between magnetic sublevels are given by the Wigner $3j$ symbols. With that the dipole operator can be written as:

$$\hat{d} = d_2 \sum_{\Lambda\Lambda'} S(\Lambda; \Lambda') \left(|\Lambda\rangle \langle\Lambda'| + |\Lambda'\rangle \langle\Lambda|\right), \tag{3.7}$$

where $|\Lambda'\rangle\langle\Lambda|$ and $|\Lambda\rangle\langle\Lambda'|$ are the energy raising and lowering operator, respectively. The coupling strength $S(\Lambda;\Lambda')$ is defined as:

$$\begin{aligned} S(\Lambda;\Lambda') =& 2(2F+1)(2F'+1) \\ & \times \begin{pmatrix} F' & 1 & F \\ -m' & m'-m & m \end{pmatrix}^2 \begin{Bmatrix} J & J' & 1 \\ F' & F & I \end{Bmatrix}^2 \end{aligned} \tag{3.8}$$

where the round brackets denote the Wigner $3j$ symbol and the curly brackets denote the Wigner $6j$ symbol.

When illuminated with a light field on resonance ground and excited states undergo a population transfer at a rate governed by the Rabi frequency defined as

$$\Omega_k = -d_2 E_k/\hbar, \tag{3.9}$$

which sets the time scale for coherent evolution. The Hamiltonian for the coherent interaction of atoms with the full laser field is then:

$$\hat{H}_{int} = \hbar \sum_{\Lambda,\Lambda',k} p^k_{(m'-m)} \Omega_k S(\Lambda;\Lambda') \cos(\omega_k t) \left(|\Lambda\rangle\langle\Lambda'| + |\Lambda'\rangle\langle\Lambda| \right). \tag{3.10}$$

k again runs over the frequency components of the laser field.

The total Hamiltonian describing the coherent evolution of the atomic states is given by the sum of the atomic Hamiltonian given in equation 3.5 and the interaction Hamiltonian from equation 3.10

$$\hat{H}_{tot} = \hat{H}_{int} + \hat{H}_a \tag{3.11}$$

3.3 Incoherent interaction with the vacuum

Spontaneous emission requires a full quantised description of the electric field, since it arises due to the existence of virtual photons in all available modes of the vacuum. A theoretical treatment of the problem is given by the Wigner-Weisskopf theory [43]. Essentially, integrating over the full atom-light Hamiltonian and tracing over the light field results a decay of the coherences (off-diagonal matrix elements) with $\Gamma/2$, where $\Gamma = \omega_a^3/(3\pi\epsilon_0\hbar c^3)d_2$ is twice the inverse of the lifetime of the excited state. The branching ratios into the sublevels of the ground state are given by the square of the Wigner $3j$ symbols, normalised by the multiplicity of the ground state $2F+1$. For

a numerical treatment of the problem, we build a matrix that creates the desired decay rates:

$$\begin{aligned}\hat{\sigma}_{SE} =& -\frac{\Gamma}{2}\sum_{\Lambda\Lambda'}\left(|\Lambda\rangle\langle\Lambda'| + |\Lambda'\rangle\langle\Lambda|\right) - \Gamma\sum_{\Lambda'}|\Lambda'\rangle\langle\Lambda'| \\ &+ \Gamma\sum_{\Lambda,\Lambda'}(2F+1)\,S(\Lambda;\Lambda')\,|\Lambda\rangle\langle\Lambda|\,. \end{aligned} \tag{3.12}$$

Collecting everything together, the Lindblad type master equation reads:

$$\dot{\hat{\rho}} = -\frac{i}{\hbar}\left[\hat{\rho}, \hat{H}_{tot}\right] + \hat{\sigma}_{SE}. \tag{3.13}$$

3.4 Dressed states

When numerically solving equation 3.13, the time step size is determined by the fastest time scale in the Hamiltonian, which is the optical frequency ω_a. The transfer between atomic states, however, happens on the time scale of the Rabi frequency Ω, which is much lower in our experiment. To perform a numerical simulation efficiently we will therefore switch into a frame of reference that rotates with the atomic transition frequency

$$\tilde{\rho}_{kl} = \rho_{kl} e^{-\mathrm{i\,sgn(k-l)\omega_a t}}, \tag{3.14}$$

where sgn(·) denotes the function returning the sign of a non-zero argument and 0 if the argument is zero. In contrast to most textbooks we rotate with the frequency of the atomic transition ω_a instead of using the laser frequency ω_L. The time scale of the simulation is now set by the detunings of the laser fields from the atomic transition. In this frame of reference we can neglect terms that rotate much faster than the detuning frequency as they average to zero. This approximation is commonly called the rotating wave approximation.

Replacing $\hat{\rho}$ by $\tilde{\hat{\rho}}$, the atomic Hamiltonian in this rotating wave approximation becomes:

$$\begin{aligned}\tilde{\hat{H}}_a =& \hbar\sum_{\Lambda'}\left[\delta_{F'} + \delta_Z(B,\Lambda')\right]|\Lambda'\rangle\langle\Lambda'| \\ &+ \hbar\sum_{\Lambda}\left[\delta_F + \delta_Z(B,\Lambda)\right]|\Lambda\rangle\langle\Lambda|\,,\end{aligned}$$

The interaction Hamiltonian is now:

$$\tilde{\hat{H}}_{int} = \frac{\hbar}{2} \sum_{\Lambda,\Lambda',k} p^{k}_{(m'-m)} \Omega_k S(\Lambda;\Lambda') \left(e^{\mathrm{i}\delta_\mathrm{k}\mathrm{t}} \left|\Lambda\right\rangle \left\langle\Lambda'\right| + e^{-\mathrm{i}\delta_\mathrm{k}\mathrm{t}} \left|\Lambda'\right\rangle \left\langle\Lambda\right| \right), \quad (3.15)$$

where $\delta_k = \omega_a - \omega_k$ is the detuning of the respective laser frequency from the central atomic transition. The spontaneous emission matrix $\hat{\sigma}_{SE}$ is unchanged.

3.5 Effect on the light field

Although the light field is fixed in the Hamiltonian, the change of the dipole characteristics of the atoms leads to a change of the refractive index of the atomic ensemble. The refractive index is nothing but the induced dipole of the atoms at the frequency of the electric field in question times the density of those atoms. The proportionality factor between the electric field E and the induced dipole moment d_i of the atom is the polarisibility $\tilde{\alpha}$ ($d_i = \tilde{\alpha}E$). To calculate $\tilde{\alpha}$ we calculate the expectation value of the dipole operator $\hat{d}$: $\langle\hat{d}\rangle = \mathrm{Tr}(\hat{\rho}\hat{d})$.

The refractive index is polarisation, frequency and intensity dependent. After finding the time evolution of the density matrix, the refractive index for each component of the electric field has to be calculated separately. We calculate the refractive index for light with frequency ω_0 and amplitude in units of the Rabi frequency Ω_0. Absorption of the light is controlled by the in-phase part of the polarisibility $\tilde{\alpha}_i$, while the quadrature ($\pi/2$ out of phase) part $\tilde{\alpha}_q$ determines the optical phase shift:

$$\left\langle \hat{d} \right\rangle = \mathrm{Tr}\left(\hat{\rho}\hat{\mathrm{d}}\right) = \tilde{\alpha}\mathrm{E} = \frac{\hbar}{\mathrm{d}_2}\Omega_0 \left(\tilde{\alpha}_\mathrm{i}\cos\omega_0\mathrm{t} + \tilde{\alpha}_\mathrm{q}\sin\omega_0\mathrm{t}\right). \quad (3.16)$$

Once $\tilde{\alpha}$ is found the refractive index is $n^2 = 1 + N_D\tilde{\alpha}$, where N_D is atomic density. Since $N_D\tilde{\alpha} \ll 1$ in the experiments that follow, the refractive index can be approximated as $n = 1 + N_D\tilde{\alpha}/2$

Using the master equation 3.13 derived above, the expectation value of the density operator is

$$\left\langle \hat{d} \right\rangle = \mathrm{Tr}\left(\hat{\rho}\hat{\mathrm{d}}\right) = \sum_{\mathrm{k,l}} \rho_{\mathrm{kl}}\mathrm{d}_{\mathrm{lk}} = \sum_{\mathrm{k<l}} \tilde{\rho}_{\mathrm{kl}}\mathrm{d}_{\mathrm{lk}}\mathrm{e}^{\mathrm{i}\omega_\mathrm{a}\mathrm{t}}\mathrm{e}^{\mathrm{i}(\omega_0-\omega_0)\mathrm{t}} + \mathrm{h.c.}\,. \quad (3.17)$$

Here $1 = \exp\left[\mathrm{i}\left(\omega_0 - \omega_0\right)\right]$ is introduced to show the origin of the detuning terms in the next step. We define the sum over the elements of the lower triangle of the product matrix as

$$\Sigma_L = \sum_{k<l} \tilde{\rho}_{kl} d_{lk} e^{\mathrm{i}\delta_0 \mathrm{t}} \tag{3.18}$$

and the sum over the elemnts of the upper triangle as

$$\Sigma_U = \sum_{k>l} \tilde{\rho}_{kl} d_{lk} e^{-\mathrm{i}\delta_0 \mathrm{t}} = \Sigma_L^*. \tag{3.19}$$

Then:

$$\left\langle \hat{d} \right\rangle = \left(\Sigma_L + \Sigma_U\right) \cos\omega_0 t + \left(\Sigma_L - \Sigma_U\right) \sin\omega_0 t \tag{3.20}$$

The diagonal elements are zero because the diagonal elements of the dipole operator are zero. The result just needs to be normalised by $E_0 = \Omega_0 \hbar/2$ to yield the polarisibility. Using the expression for the excited state life time

$$\Gamma = \frac{\omega_a^3}{3\pi\epsilon_0 \hbar c^3} d_2^2, \tag{3.21}$$

the phase shift ϕ and the attenuation of the electric field α of the light beam while travelling through a cloud with column density N_c are then:

$$\phi = \frac{3\lambda_0^2 \Gamma N_c}{8\pi\Omega_0} \left(\Sigma_L + \Sigma_U\right) \tag{3.22}$$

$$\alpha = \exp\left(-\frac{3\lambda_0^2 \Gamma N_c}{8i\pi\Omega_0} \left(\Sigma_L - \Sigma_U\right)\right), \tag{3.23}$$

with $\lambda_0 = 2\pi/\omega_0$ being the wavelength of the light in free space.

3.6 Obtaining solutions

The difficult part in the previous calculations is to solve equation 3.13 for the coherences. In the simple case of a two-level atom in a monochromatic light field aligned with the dipole moment of the atom, the steady state solution is known to be [47]

$$\rho_{eg} = \rho_{ge}^* = \frac{i\Omega}{2\left(\Gamma/2 - i\delta\right)\left(1 + s\right)} \tag{3.24}$$

with the saturation parameter $s = (\Omega/\Gamma)^2$. Hence the absorption and phase shift term recover from equations 3.22 and 3.23 and take the familiar form

$$\alpha = \frac{1}{2}\frac{3\lambda^2}{2\pi}\left(\frac{1}{1+s}\right)\frac{\Gamma^2}{\Gamma^2+4\delta^2}N_c \tag{3.25}$$

$$\phi = \frac{3\lambda^2}{2\pi}\left(\frac{1}{1+s}\right)\frac{\Gamma\delta}{\Gamma^2+4\delta^2}N_c, \tag{3.26}$$

after we assume small absorption and expand the exponential function in equation 3.23. For a multilevel atom in a monochromatic laser field, the transitions have to be weighted by their coupling strength and yield for hyperfine transitions of the ^{87}Rb D_2 line [40]:

$$\alpha = \frac{1}{2}\frac{3\lambda^2}{2\pi}\left(\frac{1}{1+s}\right)\sum_{\Lambda,\Lambda'} p_{(m'-m)}\nu_\Lambda S(\Lambda,\Lambda')\frac{\Gamma^2}{\Gamma^2+4\delta(\Lambda;\Lambda')^2}N_c \tag{3.27}$$

$$\phi = \frac{3\lambda^2}{2\pi}\left(\frac{1}{1+s}\right)\sum_{\Lambda,\Lambda'} p_{(m'-m)}\nu_\Lambda S(\Lambda,\Lambda')\frac{\Gamma\delta(\Lambda;\Lambda')}{\Gamma^2+4\delta(\Lambda;\Lambda')^2}N_c, \tag{3.28}$$

with the detuning

$$\delta(\Lambda;\Lambda') = \delta_F + \delta_Z(B,\Lambda) - \delta_{F'} - \delta_Z(B,\Lambda'). \tag{3.29}$$

ν_Λ is the fraction of atoms in the ground state $|\Lambda\rangle$, and the equations are only valid as long as these populations do not change.

No analytic solution was found for the general case of solving the master equation 3.13 for a multi-level atom in a multi-frequency light beam. I therefore used a numerical differential equation solver (`Lsoda` from the Fortran library `odepack` with the `scipy.integrate.odeint` user interface) to find the coherences between the different states and to calculate the expected light shift.

4 Experimental setup

The aim of this chapter is to give an overview of our experimental apparatus as shown in figure 4.1. Some parts of the setup are already described in the theses of my predecessors and I will refer to their work where appropriate. Also, many parts of the apparatus are standard for an atom optics experiment and are described in many textbooks (for example in [47]).

The chapter starts with a brief description of the laser setup, which mainly survived from an early experiment and is detailed in C. Sinclair's thesis [48]. It underwent only small changes since then, which are mentioned here. Thereafter, the vacuum setup is described, which is already outlined in M. Succo's thesis [49]. Here, a quick analysis of vacuum issues and attempts to circumvent them is added. The next part is about the subchip and the coils used for creating magnetic fields. The manufacture of the first-generation subchip is described in great detail by M. Succo [49]. A second generation of this chip was built and used for most of the work presented here and the differences and improvements are explained. Finally, the basic steps in an experimental cycle are outlined, which are standard to most atom optics experiments. The central parts for the work presented in this thesis, namely the photonic waveguide chip and the setup for phase-shift measurements have their own chapters.

4.1 Laser setup

The lasers in our experiment are used to address transitions of the D_2 line of ^{87}Rb as shown in the left part of figure 4.2. Our experiment contains two magneto-optical traps (MOTs), one for the low-velocity intense source of atoms (LVIS) [50] and one in the main chamber. These MOTs work on the $F = 2 \rightarrow F' = 3$ hyperfine transition. The cooling light is supplied by a commercial tapered amplifier module (Toptica TA100) as shown in figure 4.2. The module contains a diode laser with an extended cavity and

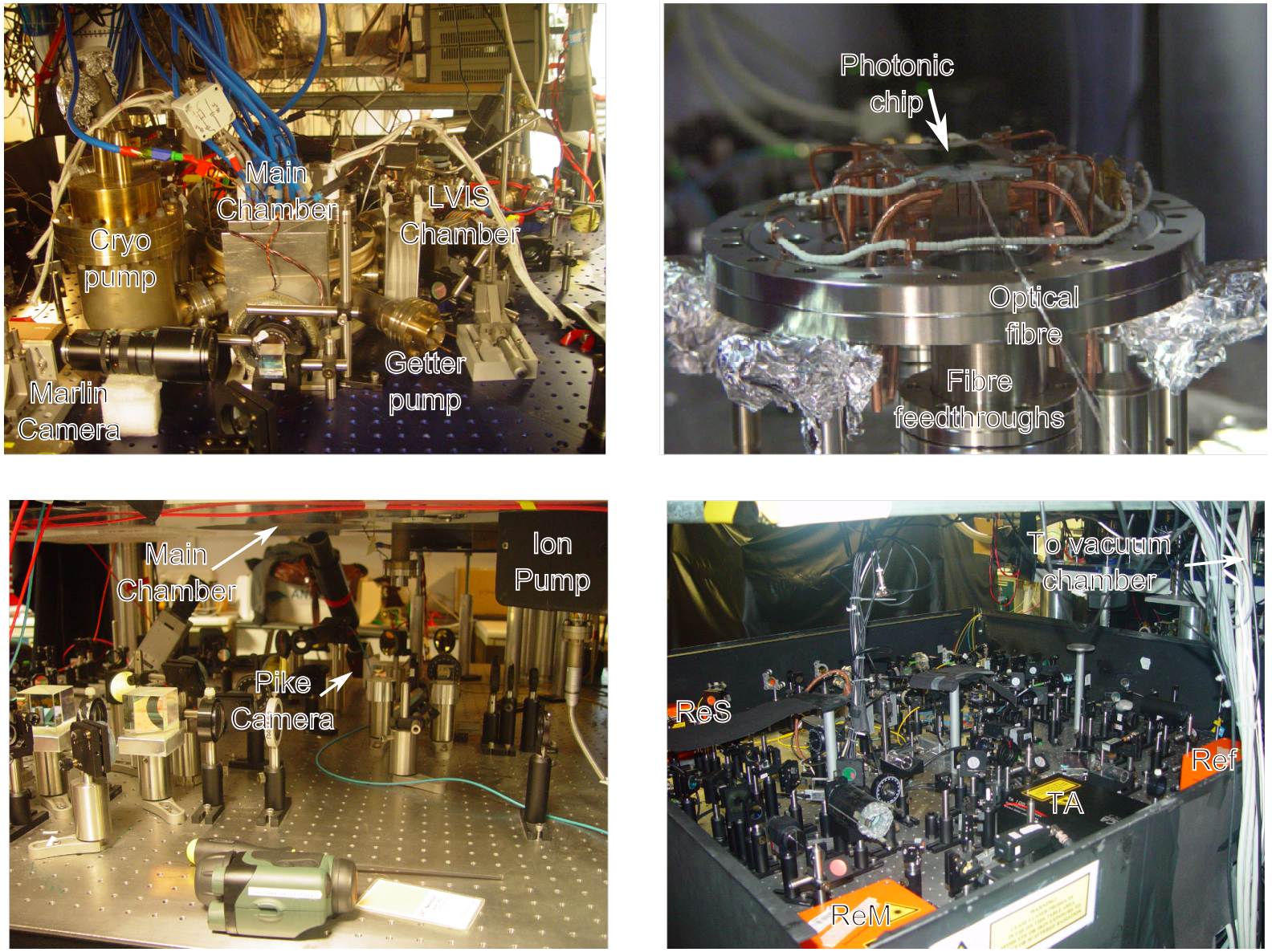


Figure 4.1: Photographs of the experiment. Top right: Image of the main chamber including cryopump and getter pump. Magnetic coils on the vacuum windows are used to create offset fields. Current for magnetic trapping runs through the blue cables, which end in electrical feedthroughs on the the top flange. The LVIS chamber is visible at the back. A schematic diagram of the vacuum setup can be found in figure 4.3. Top right: Top flange (goes onto the main chamber upside down) containing copper subchip, electric feedthroughs, photonic waveguide chip and optical feedthroughs. Bottom left: Optics underneath the main chamber, including a Pike CCD camera and the optics for the magneto-optical trap. The main chamber sits on top of the plate at the top and is optically accessible via a hole in the plate and a viewport in the bottom flange. Bottom right: Laser setup, including lasers for cooling (TA) of Rubidium atoms, for stabilising the cooling laser to a rubidium transition (Ref) and for pumping atoms lost into substates that are not part of the cooling cycle back into the cycle (ReM and ReS). Details are explained in figure 4.2.

a tapered amplifier crystal with a specified output power of 500 mW. The extended cavity ensures that the linewidth of the laser is narrower then the atomic transition and that the frequency of the laser can be tuned to the desired frequency. The output light is split in a ratio of 3:1 (LVIS:main MOT) and each beam is sent through an acousto-optical modulator (AOM), as indicated in figure 4.2, for switching. Single-mode, polarisation-maintaining optical fibres improve the mode quality before the beams are sent to the vacuum chamber.

A second diode laser equipped with an extended cavity [51] is locked to the $F = 2 \rightarrow F' = 3$ cooling transition via polarisation spectroscopy [52]. This laser, marked as Ref in figure 4.2, was assembled in our workshop [53]. Its light is used for optical pumping and as a reference for the tapered amplifier laser. For the former purpose the light is shifted by 267 MHz to the pumping transition ($F = 2 \rightarrow F' = 2$) by passing it twice through an AOM driven at 133.5 MHz. Some of that light is used for the frequency-synthesis setup as described in chapter 6, the rest is combined with the imaging light and sent to the experimental chamber. For the latter purpose some of the light is overlapped with a monitor output of the master laser of the tapered amplifier module. The beat between the two laser frequencies is detected on an RF photo-diode and locked to typically 80 MHz using a side-of-filter technique [54]. The light from the tapered amplifier is shifted back close to the cooling resonance using AOMs.

The third extended cavity laser, marked as ReM in figure 4.2, is locked to a peak in the detected spectrum, approximately 80 MHz away from the repump transition ($F = 1 \rightarrow F' = 2$), also using polarisation spectroscopy. It is fed into another diode laser (ReS) in a Slave/Master configuration to ensure sufficient repump power in all beams. Both lasers were assembled in our workshop [53]. The repump light is shifted to the repump transition by an AOM. Again, the mode profile is improved by transmission through a single-mode fibre, before the light is split and distributed between MOT and LVIS beams. We also tried adding repump light to the optical pumping and imaging beam, but as this did not improvement the atom number in the magnetic trap we refrained from doing so in further experiments.

Light for imaging and for absorption detection using waveguides is taken from the unshifted zero order light passing through the LVIS AOM. It is shifted towards resonance by its own AOM, split and coupled into three

fibres, marked as WG, Im1 and Im2 in figure 4.2. The first fibre, WG, supplies the waveguides via a second splitting stage. The second fibre, Im1, which is also used for optical pumping, leads to the horizontal imaging axis. The third, Im2, ends underneath the chamber and is used to image the long axis of the magnetic trap.

4.2 Vacuum

4.2.1 Setup

Our experiment consists of two chambers. An experimental chamber, containing the waveguide chip and an LVIS chamber, which we need for collecting and pre-cooling the atoms and which will be described in more detail later on.

The experimental chamber is a commercial 8" spherical octagon vacuum chamber from Kimball Physics (MCF800), fitted with an 8" anti-reflection coated window at the bottom and initially 6 coated windows on the $2\,^3/_4$" side flanges. The other two side flanges are used to connect the LVIS chamber, taken from the former experiment [48] and the pumping section as shown in figure 4.3. The LVIS and main chamber are connected via a pin-hole of (1 ± 0.2) mm diameter to enable ^{87}Rb atoms to enter the main chamber. The conductance through that pin-hole is very low, which means that the pressure ratio between the two chambers can be up to two orders of magnitude, preventing the Rubidium vapour from the dispensers from disturbing the magnetic trap.

The chip is mounted to a blank 8" flange on the top. This flange contains 16 high-current feedthroughs for connecting the subchip, which is a copper block containing the wires for magnetic trapping as detailed below. There are also six low-current feedthroughs to connect thermocouples and four Swagelock connectors with ferrules and fibres as described in chapter 2.

The pumping section consists of a VacIon Plus 55 ion pump from Varian with a nominal pumping speed for nitrogen of 55 l/s, a getter pump with an ST-707 cartridge from Saes getter and a UHV-24 Ionization Gauge from Varian. Note, that the LVIS has its own ion pump. The Cryopump shown in figure 4.3 was added later and showed hardly any effect. It was not operated during the experiments presented in this thesis.

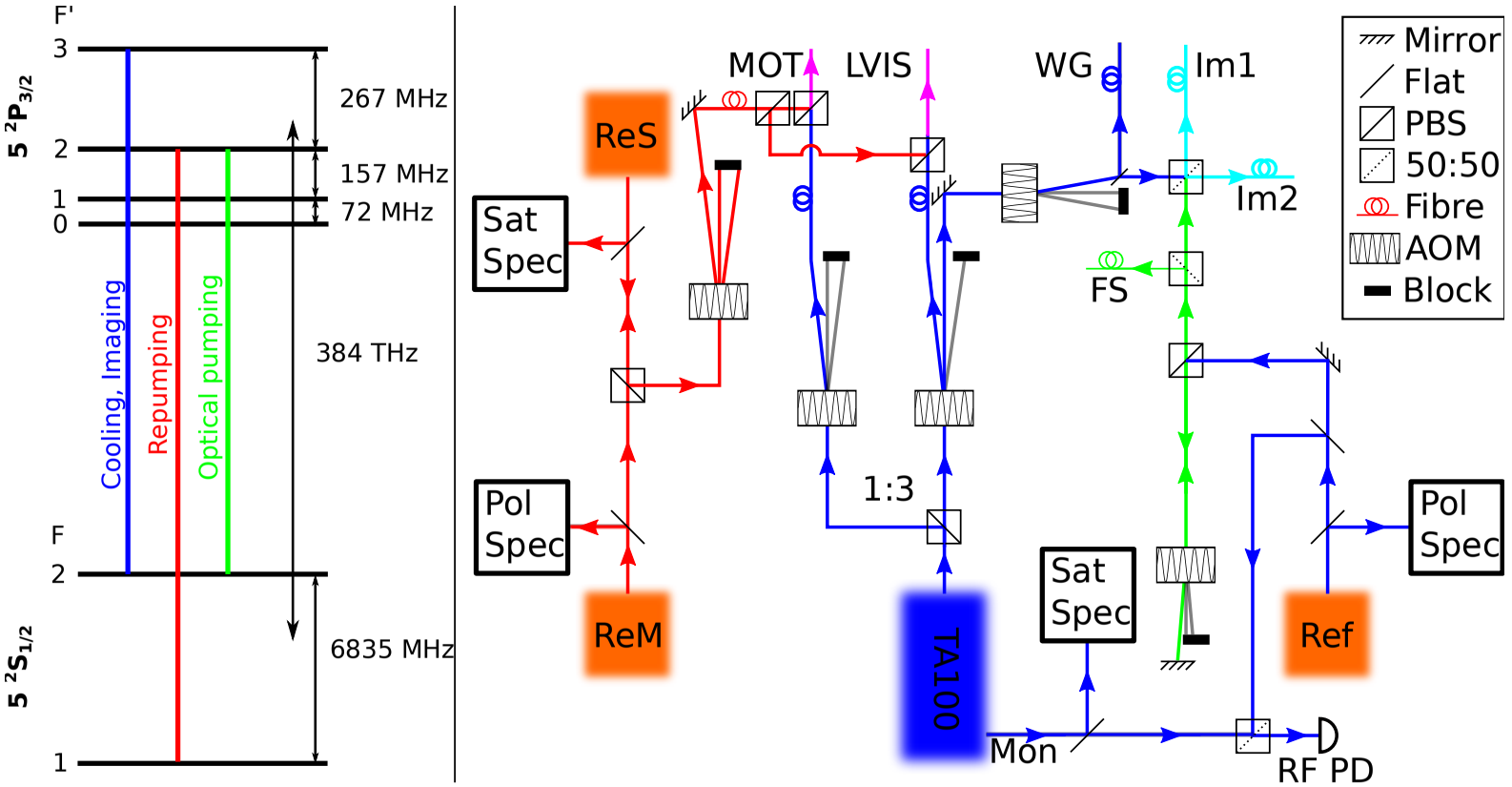


Figure 4.2: Sketch of the laser configuration used in the experiment. Neglecting details, the figure shows how the light from the Reference (Ref), Repump master (ReM) and slave (ReS) and tapered amplifier (TA100) are combined and distributed amongst the fibres for the two imaging axes (Im1 and Im2), waveguides (WG) and the frequency synthesis setup (FS) as well as the free-space beam paths for MOT and LVIS. The laseres are referenced to the atomic transition using polarisation spectroscopy (Pol Spec) and saturation spectroscopy (Sat Spec). The left diagram shows the transitions addressed by the lasers and their relative detunings.

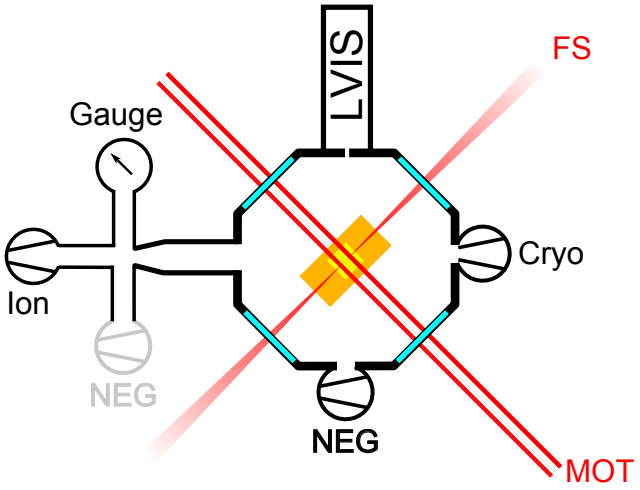


Figure 4.3: Sketch of the vacuum chamber, showing beam path for the horizontal MOT beam and the frequency-synthesised probe beam (FS). The waveguides on the chip run parallel to the FS beam. The pumping section on the left consists of an ionisation pump (ION) and an ionisation gauge. The non-evaporable getter pump (NEG) was recently moved to the main chamber to increase the pumping speed. The cryogenic pump (CRYO) was also fitted recently to pump heavier molecules that are released from glue and the acrylate fibre coating.

4.2.2 Limitations

Although the dimensions of the pumping section seem well suited to achieve an ultra high vacuum (UHV) with pressures below 10^{-10} torr, our setup is still struggling to reach this pressure. Currently, the pressure is stuck at 10^{-9} torr, which limits the lifetime of our magnetic trap to a few seconds and obstructs efficient evaporative cooling. The search for possible explanations revealed two main candidates which might contaminate the vacuum: the acrylate coating of the fibres and the glue used to construct the subchip. Outgassing tests done in a separate chamber hint that both are part of the problem but cannot explain the full gas load. Figure 4.4 shows results of these tests. The time evolution of the pressure is fitted with the following model:

$$V\frac{dP}{dt} = \sum_i Q_i \exp\left(-\frac{t}{\tau_i}\right) \tag{4.1}$$

where the gas loads Q_i and the time constants τ_i of the empty chamber, the fibres and the glue were fitted to all three curves simultaneously. It is obvious that glue and fibre increase the outgassing by a factor of 2 and 3 respectively. However, the total amounts of glue and fibre in these tests

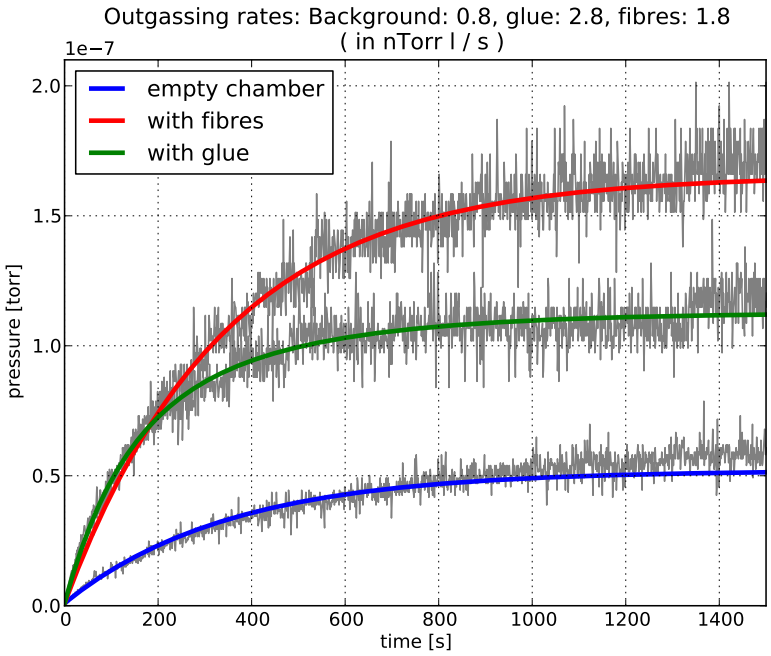


Figure 4.4: Pressure rise after switching off the ion pump as measured in a test chamber with similar volume and pumping speed to the main chamber. The three curves show the pressure rise for an empty chamber, a chamber containing large amounts of glue and a chamber with 10 m of fibre, including the acrylate coating.

exceed the amounts in the main chamber by a factor 3 and 5, respectively. The same experiment on the main chamber shows a steeper pressure rise, but is not directly comparable to the test chamber data due to different volume and geometry of the chamber. For a comparable experiment we would need to break the vacuum in the main-chamber and disassemble parts of the working setup which would severely disrupt the experiment.

To avoid a rebuild of the chip, we tried to increase the effective pumping speed by moving the NEG pump to one of the ports of the experimental chamber and by attaching a cryogenic pump, which has a better pumping speed for larger molecules. However, neither of these changes produced a significant improvement in the overall pressure or in the lifetime of the magnetic trap.

4.3 Magneto-optical trapping

The experiments presented in this thesis make use of two fundamentally different trapping techniques: the magneto-optical trap (MOT) and the magnetic trap. A magneto optical trap is formed by three pairs of counter-propagating beams in the three dimensions of space. The beams are detuned to the red side of an atomic resonance. When the atoms move in the light beams, the Doppler shift brings the atoms closer to resonance with that light beam propagating in the opposite direction. The atom scatters more photons from that beam and will therefore be slowed down. A quadrupole field is introduced to make the force position-dependant. The Zeeman shift of the atoms brings the atoms closer to resonance with the counter-propagating laser beam when they try to leave the centre of the trap, provided that the polarisation of the light beams is chosen correctly. This provides a restoring force towards the centre of the MOT.

The MOT is a dissipative trap: not only does it hold the atoms in a certain place, it also cools them. Because of the polarisation gradient cooling mechanism [55], the atoms in our ^{87}Rb MOT are cooler than the Doppler temperature $T_D = 146\mu$K [1], typically reaching a few tens of μK. At the density reached in our MOT, typically about $0.04\,\text{atoms}/\mu\text{m}^3$, this is still far from degeneracy. To cool the atoms down to degeneracy, we have to use cooling techniques that do not depend on the scattering of photons, which is in our case magnetic trapping and forced evaporation.

For our experiments we use two MOTs. The first MOT is almost a standard MOT as described above. It sits in a separate chamber, labelled LVIS in figure 4.3, and is formed by three retro-reflected laser beams and a pair of anti-Helmholtz coils for the quadrupole field. In front of each retro-reflecting mirror is a quarter-wave plate to reverse the circular polarisation. The trap catches atoms from a ^{87}Rb background vapour released from a Rubidium dispenser.

One of the beams is reflected off a quarter wave plate with a silver coating that sits under vacuum at the junction of the two chambers and contains the pin hole. Atoms escape from the MOT through the hole where the reflected beam is missing. They form a beam of cold atoms that enters the main chamber. A MOT in this configuration is called a low-velocity intense source of cold atoms (LVIS [50]). The two-chamber system has the

advantage that the main experiment can be done at a very low pressure, whereas the LVIS can collect atoms from a ^{87}Rb vapour at higher pressure.

The atoms are picked up in the main chamber by the second MOT. This MOT consists of two pairs of counter-propagating beams, where one pair is reflected of the surface of the chip. The atoms see the same configuration as explained above when the MOT coils are arranged around the axis of one of the reflected beams. This MOT is known as a reflection-MOT [56].

Finally, the quadrupole field is generated by current flowing through a U-shaped conductor, together with a homogeneous offset field [57]. The use of a U-plate, rather than coils, greatly simplifies the chip setup. This U-MOT is the starting point for almost all experiments described in this thesis.

4.4 Magnetic trapping

The $F = 2$ ground state of ^{87}Rb has 5 Zeeman sublevels with magnetic quantum number $m = -2...2$. In a small magnetic field B (linear regime) the energy of these states shifts as $mg_F\mu_B B$ as described in chapter 3. For the $F = 2$ ground state $g_F = 1/2$. The states with $m = 2$ and $m = 1$ can therefore be trapped in a minimum of the magnetic field. In our experiments we pump the atoms into the $m = 2$ state for tighter trapping at a given magnetic field gradient.

The magnetic field gradients for the trap are produced by current in a Z shape wire together with a homogeneous offset field. A long wire with an offset field creates a $2D$ confining quadrupole potential. The potential is closed in the remaining dimension by the ends of the Z as shown in figure 4.5). For further details and scientific applications the reader is referred to the following review articles [12, 13, 14].

4.5 Subchip

The currents for trapping and guiding the atoms are carried by a wire subchip immediately beneath[1] the optical chip. An exploded diagram of the chip is shown in figure 4.6. The base of the subchip is a copper block to heat sink the current-carrying elements. On top of that is a piece of

[1] The terms "above" and "beneath" in this section refer to the chip as it is built. In the vacuum chamber it will be mounted upside down

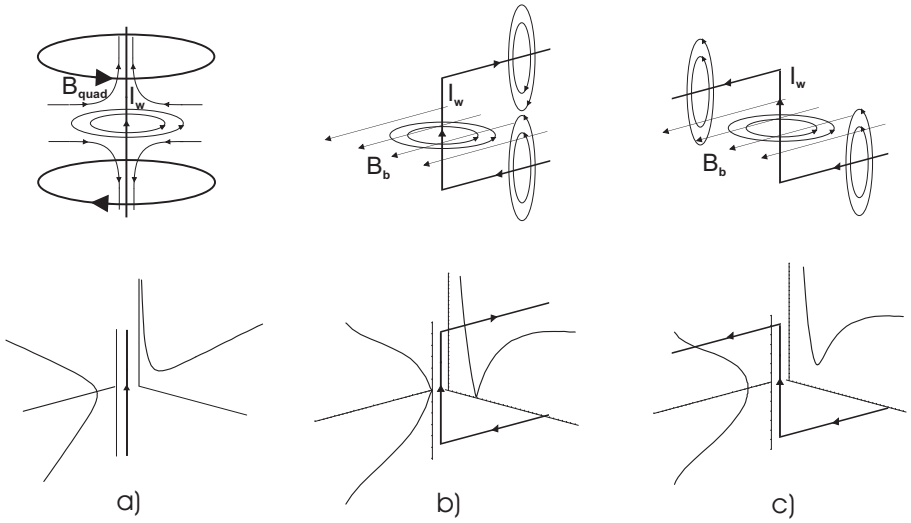


Figure 4.5: Magnetic field geometries for creating trapping potentials with a wire and an offset field. The geometries used on our experiment are the U wire configuration (b) for the MOT and the Z wire trap (c) for conservatively trapping the atoms. Figure taken from [12].

Shapal[2] to insulate the current-carrying elements from each other and from the base. The Shapal piece has three pockets, one at the bottom and two at the top. The one at the bottom accommodates a U-plate used to create a quadrupole field for the MOT [57], the two at the top are for two bias wires which generate a homogeneous offset field. On top of the Shapal piece is an H-plate (see figure 4.7), containing a conducting H structure along with two end wires. The H-plate, U-plate and bias wires were cut from a copper plate using a wire-cutting electric discharge machine. All copper parts are surface oxidised at 200 °C for 4 hours. They are then glued together using Epotek H-77 and H-74 epoxy, cured at 130 °C for 2 hours. We found that the copper-oxide forms a much better bond with the epoxy than pure copper.

The H-plate can be connected to form either a U or a Z configuration as required. Running 80 A through the bias wires and 38 A through the H-plate in Z configuration, we can produce magnetic traps with trapping frequencies of 1100 Hz × 1100 Hz × 30 Hz when the trap bottom field is 0.1 mT. The end wires provide additional control over the tilt of the trap with respect to the waveguides and slightly boost the axial trapping frequency. The H-part connected in U configuration can be used to force the MOT into a shape

[2]Shapal^{TM} is a machinable form of aluminium nitride ceramic with a high thermal conductivity (90 W/mK).

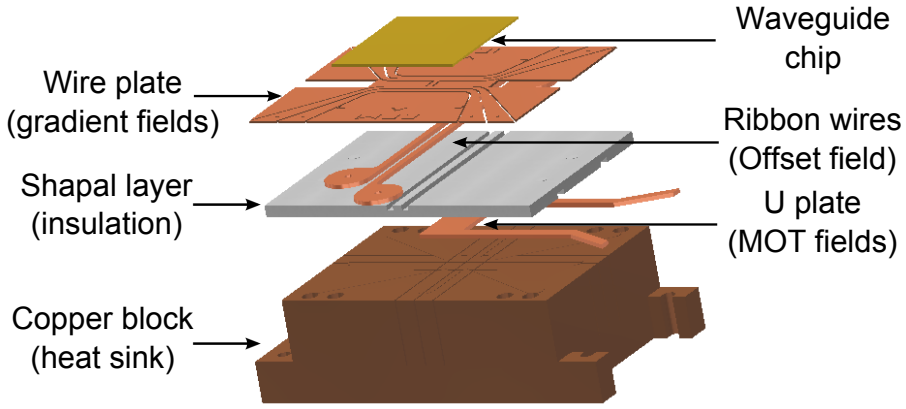


Figure 4.6: Exploded drawing of the chip as it is mounted on the vacuum flange. From bottom to top the layers are (purpose in brackets): Copper block (heat sink), U plate (MOT fields), Shapal layer (electrical insulation), ribbon wires (bias fields), wire plate (field gradients), waveguide chip (light access).

that closely matches the magnetic trap.

4.6 Two generations of atom chips

The work presented in chapter 5 was done with two different generations of our atom chip. The first generation is described in M. Succo's thesis [49]. Although design and fabrication of the second generation chip is very similar to the first, there are a few substantial changes. The first one is that we added the U-plate as described above [57]. On the first generation of the subchip we used a pair of small coils to generate the magnetic fields for the MOT. Changing over to the U-plate substantially simplifies the setup and frees up optical access while additionally elongating the MOT in a desirable direction. This increases the spatial overlap between the MOT and the magnetic trap.

Second, the shape of the bias wires was changed from round to ribbon wires with a rectangular cross section. This increases the conducting area by more than a factor 2 and improves thermal contact with the Shapal layer, which became necessary after the previous chip partly burnt due to overheating of those wires. Furthermore, the length of the central part of the Z-wire was reduced to increase the axial trapping frequency but this also reduces the atom number in the magnetic trap.

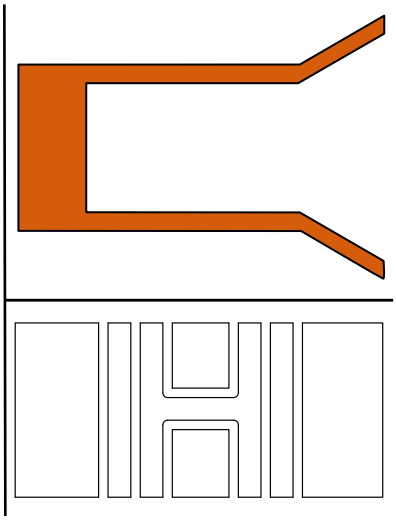


Figure 4.7: Left side: Wire plate with H structure coloured in dark grey and end wires coloured in light gray. The lower right part shows a zoom of the central part of the H. The wires are 1.2 mm wide and the central part of the H is 4 mm long (inner part only). The plate is 0.5 mm thick. Upper right: Dimensions of the U-plate are 10 mm × 24 mm (without connectors). The plate is 1 mm thick.

With the improved chip we were able to run 80 A through the bias wires and 50 A through the H-plate continuously with the temperature of the chip rising by less then 30 °C. For shorter duty cycles the current through the H-plate can be increased to 80 A without damaging the chip.

Along with the new subchip we used a new waveguide chip. Although the chip itself is identical to the one previously used, we changed from individually connecting three waveguides to optical fibres to connecting all twelve waveguides using a fibre V-groove assembly as described in chapter 2. For these V-groove assemblies to fit onto the subchip, parts of the excess copper from the wire chip were removed. It was also necessary to change the fibre vaccum feedthroughs from commercially available optical feedthrough from LewVac to the Teflon ferrules described in reference [38]. Since the commercial feedthroughs introduced losses of 50 % each, changing the feedthroughs substantially increased the overall transmission of light through the setup.

4.7 Coils

Homogeneous offset fields in all three directions of space are provided by coils mounted outside the chamber. These fields can be used to move the

MOT around and to compensate for stray fields. Two pairs of these coils are mounted around four of the side windows of the chamber, connected in Helmholtz configuration. They contain approximately 190 windings each and generate an offset field at the centre of the chamber of 1.3 G/A. They are driven with bipolar power supplies with a maximum current of ±12 A. The third pair of coils is mounted around the 8" top flange and bottom window. They contain approximately 150 windings and create a centre field of 13 G/A.

4.8 Basic experiment

The starting point for all the experiments presented in this thesis is a magneto-optical trap formed by two counter-propagating beams reflected off the gold surface of the waveguide chip at an angle of 45 °. The confinement along the third axis is provided by two beams counter-propagating along the perpendicular, horizontal axis. The magnetic fields are created by running 70 A through the U-plate. The MOT is supplied with cold beam of atoms from the LVIS and can be moved with offset fields from the external coils to maximise the atom number.

Atoms above (or rather below) the surface of the waveguide chip can be imaged by standard absorption imaging. The intensity profile $I_s(x, y)$ using resonant light passing through the atoms is recorded on a CCD camera, AVT Pike F-145 and AVT Marlin F-033 in our case as shown in figure 4.1. The image is compared with a reference image I_r recorded when no atoms are present (figure 4.8). Light travelling through the atomic cloud is attenuated according to the Beer-Lambert law. The optical column density along the beam propagation axis can be calculated knowing the resonant atomic cross section $\sigma_0 = 3\lambda^2/(2\pi)$ for circularly polarised light on the cycling transition. Integrating over the whole CCD image yields the number of detected atoms:

$$N_{at} = -\frac{1}{\sigma_0} \int dx \int dy \log\left(\frac{I_s(x, y)}{I_r(x, y)}\right) \tag{4.2}$$

With the trap on, the absorption image gives information on the density distribution of atoms in the trap. When the trap is switched off a few ms before the image is taken, the spatial distribution is related to the momentum distribution of the trapped atoms, which can be used to diag-

nose temperature or acceleration of the atoms due to residual magnetic field gradients.

Figure 4.8 shows an example absorption image of atoms in a magnetic trap. The atoms are imaged with an absorption beam hitting the chip surface at an angle of 45 °. The imaging beam is slightly rotated with respect to the MOT beams and detected with the Pike camera. The cloud and its image are both visible. The waveguides are also visible, since the chip surface above the waveguides is not even and light is randomly scattered. The cloud is imaged along its long axis, which is important for diagnosing alignment and shape of the magnetic trap. The color coding refers to detected atomic column density, where red is high densities and blue low densities. The parameters of this particular atom cloud are given in the figure caption.

A second imaging beam runs along the horizontal MOT axis and is detected with the Marlin camera. This image integrates along the long axis of the trap, giving largest optical density for experiments with small atom numbers.

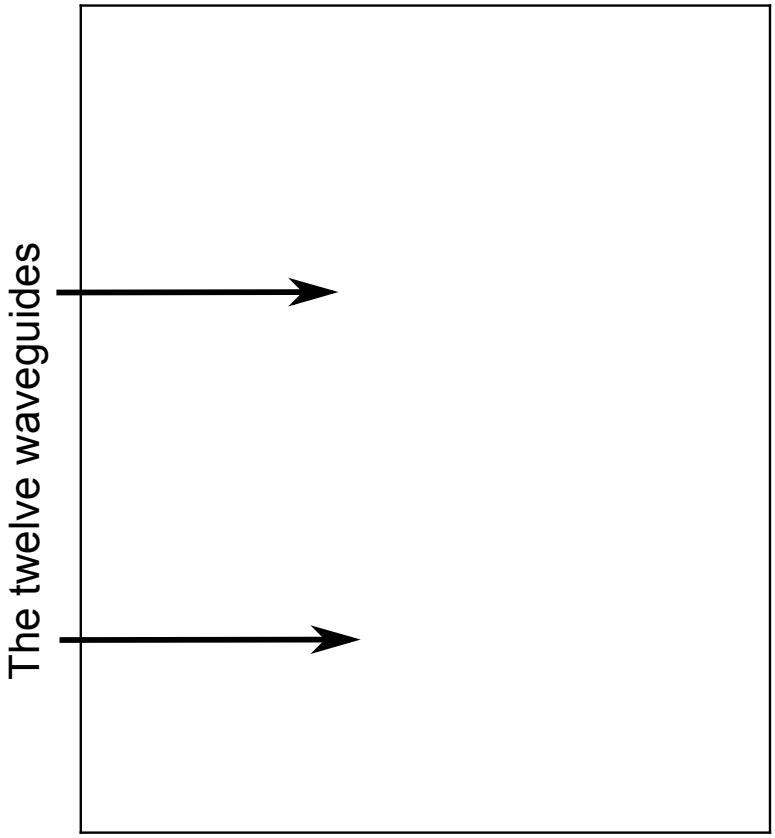


Figure 4.8: Absorption image of a magnetically trapped cloud containing $600,000$ atoms. The color scale corresponds to the optical density, where red corresponds to a larger optical depth. The long axis of the cloud is $350\,\mu$m long. The imaging beam is reflected of the waveguide chip and the mirror image of the cloud is visible as well. The waveguides (going from bottom to top slightly left of the centre of the image) produce an uneven surface of the chip, and light hitting those region is scattered and not captured by the camera.

5 Detecting atoms with a photonic chip

The major part of the work presented in this chapter is published in Nature Photonics with the title "An array of integrated atom-photon junctions" [58] and describes the first experiments with cold atoms interacting with light from a photonic waveguide chip. The aim of the experiments is to demonstrate the sensitivity of the apparatus as well as to characterise light parameters such as frequency, intensity and polarisation using the atoms as a probe.

The chapter explains how the observed absorption and fluorescence signals can be related to the atomic density in the trench. Subsequently, the experimental sequence is described along with the measurement protocol for characterising each of the twelve waveguides. The experiments that diagnose frequency, polarisation and intensity of the light using the atoms as a probe are presented thereafter. Finally, first measurements of magnetically trapped atoms with waveguide light are described.

For the discussion we introduce a coordinate system where z points along the flow of current in the central part of the Z wire, x points along the propagation direction of light, and y is the direction of gravity.

5.1 Atoms in a light mode

To calculate how the presence of an atomic cloud changes the intensity of a transmitted light beam, we start with a density distribution of atoms $N_D(x, y, z)$ and a light field $E(x, y, z)$. The scattered light power is proportional to the intensity of the input light beam $I(x, y, z) \propto E(x, y, z)E^*(x, y, z)$. The curvature of the wavefront changes the polarisation of light with respect to the magnetic field for different positions of the atomic cloud. In the presented experiments, however, these effects are small and we will neglect

the wavefront curvature in the following. We can then define the number of atoms that interact with the light as the integral over atom density, weighted by the intensity of the light:

$$N_a = \frac{1}{I_0} \int_{-\infty}^{\infty} dx \int_{-\infty}^{\infty} dy \int_{-\infty}^{\infty} dz \, I(x,y,z) N_D(x,y,z) \tag{5.1}$$

with $I_0 = 1/(\epsilon_0 c) \times E^2(0,0,0)$. The light field in the trench can be approximated by a Gaussian profile as defined in equation 2.9, with a $1/e$ field radius of $w_w = 2.18\,\mu$m. When atoms are launched from a MOT at the trench we can assume a constant atomic density over the whole trench volume, since the MOT is much larger then the trench. Furthermore, the interaction region is limited to the length of the trench l in x direction. The number of atoms then becomes

$$N_a = \frac{N_D}{I_0} \int_{0}^{l} dx \int_{-\infty}^{\infty} dy \int_{-\infty}^{\infty} dz \, I(x,y,z) = \frac{\pi l w_w^2}{2} N_D \tag{5.2}$$

There are two ways of detecting these atoms using resonant light. The first is to excite the atoms with an external light beam and observe the photons scattered into the waveguide mode. A signal recorded this way is shown in the right graph of figure 5.1. The number of photons scattered is maximised by using intensities well above saturation. Here, each atom scatters photons with a rate of $\Gamma/2$, which makes the total rate of photons arriving at the detector

$$\dot{N}_\gamma^{fl} = \frac{\Gamma}{2} \frac{w_w^2}{l^2} \frac{\pi l w_w^2}{2} N_D, \tag{5.3}$$

which directly maps to the measured power as $P = \hbar\omega_a \dot{N}_\gamma^{fl}$. The solid angle that the waveguide mode covers for an atom in the centre of the trench is only $w_w^2/l^2 = 1/64$, which means that the collection efficiency is very low.

The other method measures the number of photons scattered out of the waveguide mode. This is done by comparing the intensity of a light beam after passing through the atoms with the intensity of the same light beam detected when no atoms are present. To maximise the signal, the intensity recorded when no atoms are present relative to the intensity detected in the

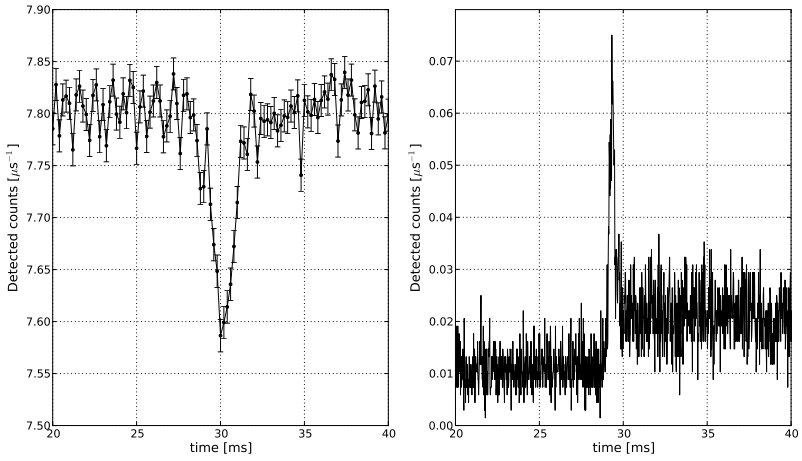


Figure 5.1: Absorption and fluorescence of light by atoms detected with the waveguide chip. The curves are an average from several individual runs to increase the signal-to-noise ratio.

presence of atoms must be maximised. This can be done by using a beam size that does not exceed the size of the atomic cloud and by choosing light intensities that do not saturate the atomic transition, i.e. that are smaller than the saturation intensity I_{sat}. The fraction of light absorbed in this circumstances is

$$\alpha = \frac{\hbar\omega_a \Gamma l}{2I_{sat}} N_D. \tag{5.4}$$

Note, that I_{sat} depends on the polarisation of the light and the state of the atoms. Since our vacuum chamber obstructs the view of the detector, we can only use a small solid angle to collect photons. Therefore, absorption signals can usually be acquired with a larger signal-to-noise ratio than fluorescence signals.

5.2 Characterising 12 atom-photon junctions

Atoms are brought into the trench according to the following sequence: the MOT in the main chamber is loaded for 3 s (see chapter 4) 4 mm away from the chip surface. A typical MOT contains 150 million atoms at a temperature of about 100 μK and a peak density of 0.04 atoms/μm^3. The

magnetic field minimum is then shifted towards the chip surface by ramping the current through the offset coils. The atoms move 4 mm in 10 ms, thus they are launched towards the trench with a velocity of 0.4 mm/ms. After the ramp is completed, the MOT light is switched off.

For absorption measurements, light transmitted through one of the waveguide channels is monitored on a single photon counting avalanche photodiode (SPAPD). The light intensity is set well below atomic saturation to maximise the absorption signal. The left graph in figure 5.1 shows the time trace of such a measurement. The light level recorded on the SPAPD when no atoms are present is 7.80 photons/μs. At $t = 20$ a magnetic field ramp is executed that launches atoms from the MOT towards the trench and the MOT is switched off at $t = 30$. When the atoms reach the trench, the light level is reduced to a value of about 7.58 photons/μs. The curve in figure 5.1 shows an average over about 100 measurements to enhance the signal to noise ratio. With equation 5.4 and the appropriate saturation intensity $I_{sat} = 22\,\mathrm{pW}/\mu\mathrm{m}^2$ (see below), we infer a density of $10^{-2}\,\mathrm{atoms}/\mu\mathrm{m}^3$, which is about 1 atom in the waveguide mode on average.

For fluorescence measurements, light scattered from an external beam is monitored on the SPAPD. Here, the light intensity is well above saturation to maximise the signal. Such a measurement is shown in the right graph of 5.1. An external excitation beam focussed onto the trench is switched on at $t = 29$ ms, when the atoms are just above the trench. The light beam pushes the atoms into the trench, which makes the peak much sharper than the dip in the graph on the left side. The excitation beam is left on, slightly increasing the light level even after the atoms have left the trench. This trace is an average over 34 measurement. With equation 5.3 we infer a density consistent with the $10^{-2}\,\mathrm{atoms}/\mu\mathrm{m}^3$ measured in the absorption measurement.

To characterise the 12 atom-photon junctions, three measurements were performed on each junction[1]:

- Transmission of light from input to output fibre
- Absorption of light when trench is homogeneously filled with atoms

[1] Measurements presented here are done with two different generations of atom chips (see chaper 4). While the characterisation of all twelve channels and the measurements with atoms from a magnetic trap was done on the second generation chip, all other measurements in this chapter where done on the first generation.

- Fluorescence from a beam focussed to 40 μm

Figure 5.2 shows how the optical transmission of each channel is measured. We first measure the light power leaving the supply fibre and compare it with the light power leaving the output fibre. The measured loss comprises the loss of light at the junction between supply fibre and input fibre, input fibre and waveguide, waveguide and output fibre and through the trench. The results are shown in the first graph of figure 5.3. The gray shaded area shows the 1σ interval around the mean value. Poor overall transmission is measured due to a copper piece sticking out underneath the waveguide chip which dramatically reduces the input fibre to waveguide coupling (see chapter 4). The resulting gap between the V-groove array and the end facet of the chip might include contaminations, which can be the reason for one of the channels showing almost no transmission.

The large fluctuations between points is due to the junction between supply fibre and input fibre. This junction is established using bare fibre terminator units (Thorlabs BFTU). These clamp the fibre in place with a spring. The coupling of light from the supply fibre into the input fibre (figure 5.2) critically depends on the exact position of the fibre. Ideally, the end of the input fibre should be as close to the supply fibre as possible, with both end facets oriented parallel to each other. To achieve maximum transmission, the input fibre has to be pressed against the supply fibre while monitoring the transmission of light. However, the spring cannot hold the fibre in this position. The movement of one fibre against the other degrades the quality of the end facets of both fibres, leading to an overall reduction in the maximum achievable coupling. The recorded transmission values are the optimal values found after several minutes of tweaking.

The second set of measurements shown in figure 5.3 are absorption measurements as described above. For these measurement the BFTU at the input is replaced with a fibre-to-fibre mechanical splicer (Thorlabs TS-125), whose overall coupling efficiency is smaller than the maximal value achievable with the BFTU, but guarantees a more stable coupling. Here, we measure the fraction of light that is transmitted from the atoms to the detector. Since drifts in the supply fibre to input fibre junction equally affect the light power at the atoms and at the detector, these drifts do not affect the inferred transmission. All 11 working channels measure similar absorp-

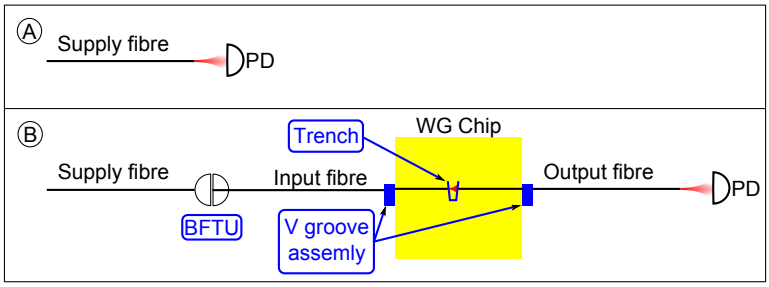


Figure 5.2: Measuring transmission across the setup. We denote as total transmission the fraction of power measured on the photo diode (PD) in part B of the power measured in part A. Losses occur at the interfaces labelled in blue. For the measurement of the atomic saturation the bare fibre terminator unit (BFTU) is replaced with a fibre splicer and losses from the trench to the PD are measured. This isolates the loss due to one waveguide-fibre interface.

tion values. Residual fluctuations are due to fluctuations in the local atom density in the trench. These fluctuations are due to the imperfect reflection of the MOT beam on the chip surface in the waveguide area as described in chapter 4, leading to an inhomogeneous intensity profile and therefore an inhomogeneous distribution of atoms.

The third set of measurements shown in the lowest graph of figure 5.3 is a fluorescence measurement as described above. The beam exciting the fluorescence is supplied by a single-mode fibre and focussed to a waist of $40\,\mu$m. The waist at the focus is measured by fitting a Gaussian profile to the intensity distribution recorded on a CCD camera before the beam is focussed into the chamber. The fibre collimator is then mounted underneath the chamber and reflected off the chip. The reflection can be seen on the Pike camera, which looks into the chamber from underneath. By maximising the intensity recorded on a single pixel we can ensure that the light intensity at the atoms is equal to the intensity at the focus to within a few percent.

Since the excitation beam is smaller than the length covered by the array of waveguides, each channel is expected to record a different fluorescence count rate. The beam intensity is kept below saturation to provide a linear depends between photon count rate and light intensity. A Gaussian profile fitted to the measured points as shown in figure 5.3, gives a waist of $(40 \pm 3)\ \mu$m, in agreement with the waist of the beam measured on the CCD.

Channels 2 and 5 pick up almost no fluorescence light. It is not entirely obvious why this is the case, since those channels work well in the transmis-

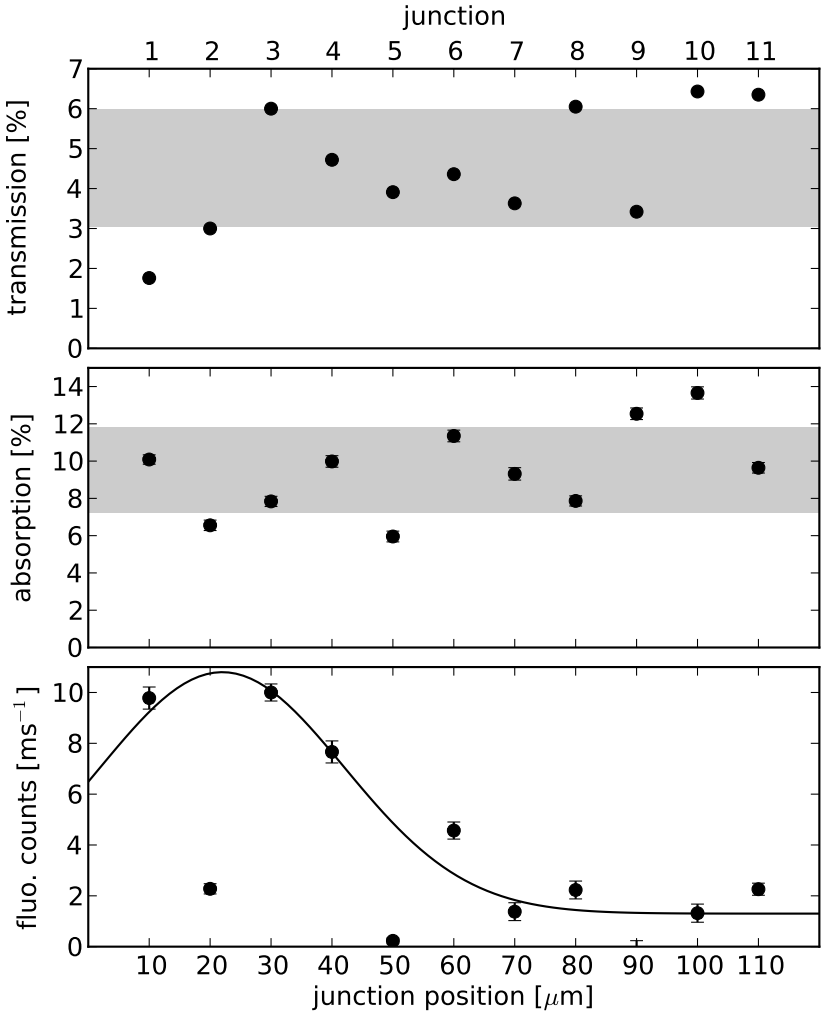


Figure 5.3: Three measurements to characterise the waveguide. Top: Transmission of light through the whole setup. Centre: Absorption due to atoms in the trench. Bottom: Fluorescence from a focused light beam. A Gaussian profile with a $2/e$ radius of $40\,\mu$m fits the measurement. Channel 2,5 and 9 do not work in the third measurement (see text). One of the outermost channels shows almost no transmission and is not included in the graph.

sion and absorption measurements. It might be due to defects or impurities absorbing some of the light or due to reflections from the bottom of the trench interfering with the incoming beam at the waveguide input, even when no atoms are present. For channel 9 we inferred a negative fluorescence count rate and also a very large error bar. This is probably due to a defect scattering light directly into the waveguide.

5.3 Measuring polarisation stability

The fibres guiding light to the waveguide chip are not polarisation maintaining, since control over the polarisation at the junction is desirable. This raises the question of how stable the polarisation can be kept over time. We measure the polarisation components of the light that address atomic $\sigma^{\pm}$ and π transitions, using the atoms as a probe. Set to a particular polarisation in the atomic basis, this polarisation remains the dominant component for more than 30 min. This is sufficiently stable to perform polarisation-sensitive experiments.

The experiments presented here are spectroscopic measurements of transitions between different Zeeman states. The atoms are in a magnetic field of 0.78 mT along the waveguide axis. The $\sigma^{\pm}$ cycling transitions tunes by $\pm\mu_B B$. With the magnetic field parallel to the propagation of light, σ^{+} and σ^{-} transitions are addressed by left- and right-hand circular polarised light from the waveguides. In a spectroscopic measurement, the peaks for the two cycling transition in a magnetic field of 0.78 mT are expected to be separated by ≈ 22 MHz, with the relative height of the two peaks depending on the relative amount of left-hand and right-hand circular polarised light in the beam. By controlling the light polarisation at the fibre input we can change the polarisation of light at the atoms and therefore the relative height of the two peaks in the spectrum. When we reverse the magnetic field, the role of left- and right-handed light is reversed and we expect the relative hight of the peaks in the spectrum to swap. If we swap both light polarisation at the input and field direction we expect no change in the spectrum.

The result of the spectroscopic measurement is shown in figure 5.4. Here, we measure how the light polarisation measured at the input maps across to light polarisation measured in the basis of atomic transitions in the trench.

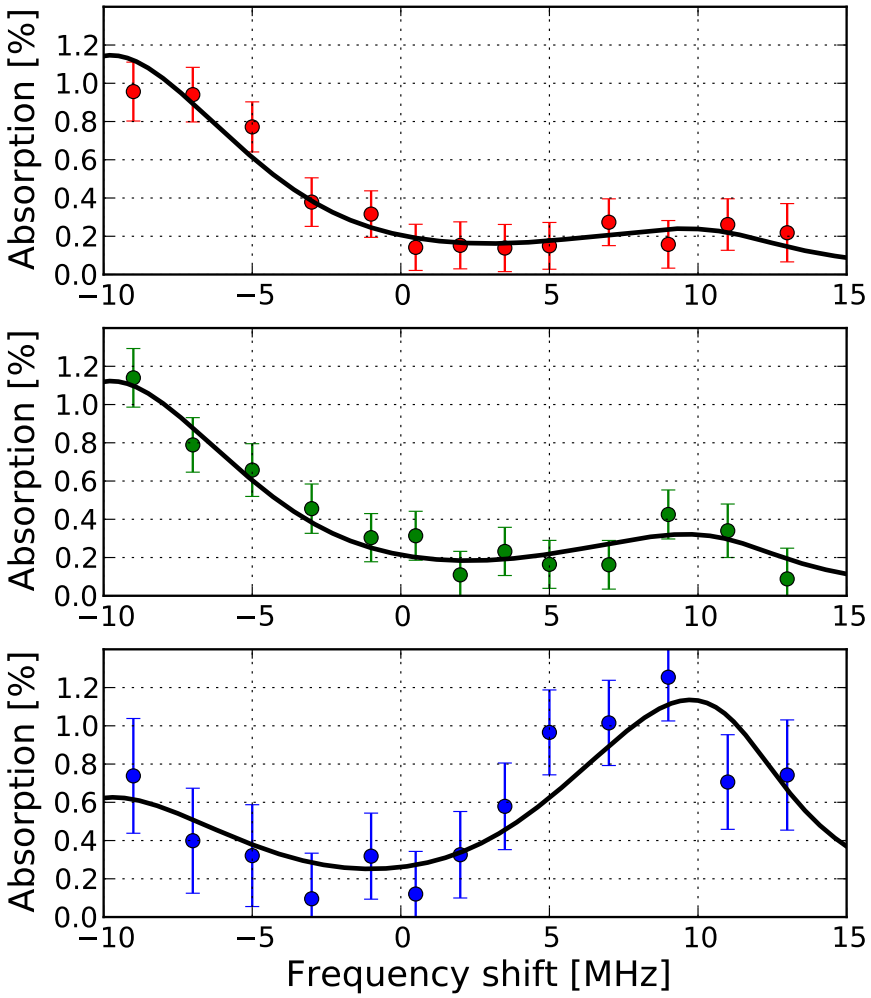


Figure 5.4: Measurement of the mapping of input polarisation to atomic transitions via Zeeman spectroscopy of atoms in a magnetic field. Data for each graph is acquired over the course of 1 h. Top: Atoms in a magnetic field of +0.78 mT, right handed circular light at the input. The light drives on average 85% σ^- transitions (left peak). Centre: Atoms in a magnetic field of −0.78 mT, left handed circular light at the input. The light drives on average 80% σ^+ transitions (left peak). Bottom: Atoms in a magnetic field of +0.78 mT, linear (vertically) polarised light at the input. The light drives on average 35% σ^- transitions (left peak).

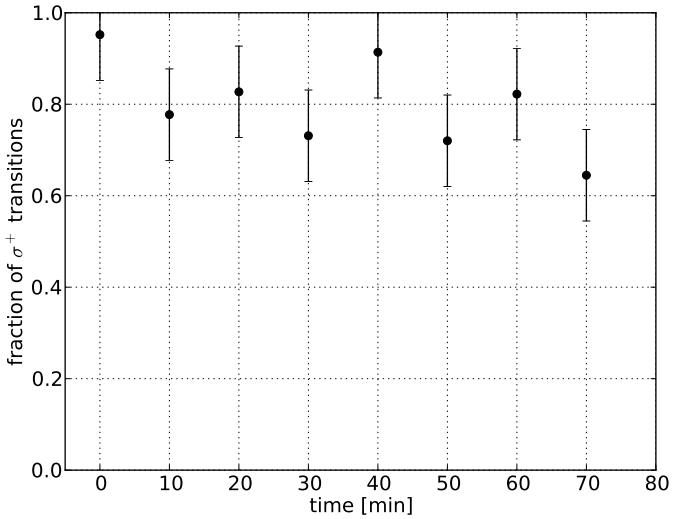


Figure 5.5: Stability of polarisation mapping. The data acquired over the course of 70 min for the centre graph in figure 5.4 is analysed in intervals of 10 min and the relative fraction of light driving σ^+ transitions in each interval is plotted. The fraction decreases from $(95 \pm 10)\,\%$ to $(65 \pm 10)\,\%$ during the measurement. The setup is therefore stable enough to perform polarisation sensitive measurements.

For the experiments shown in the first graph, we adjusted the polarisation at the fibre input to right-handed circular polarisation by analysing the light using a polarising beam splitter cube and a quarter-wave plate. We then collect about 300 measurements for each data point, shuffling the order of the measurements in each scan to eliminate effects of systematic drifts. Error bars indicate 1σ statistical uncertainties for Poissonian light, corrected for the detector dead time. The solid curve in that graph shows a fit of equation 3.27 to the data. For the fit we assume an equal distribution of atoms among magnetic sublevels of the $F = 2$ hyperfine ground state and a small saturation parameter so that $1 + s \approx 1$. Fit parameters are the atomic density N_D and the polarisation tuple $p = (p_+, 0, p_-)$. The fit to the data in the first graph indicates that on average $(85 \pm 3)\,\%$ of the light drives atomic σ^- transitions, which corresponds to the left peak in the first graph of figure 5.4.

For the data presented in the middle graph of figure 5.4 we reversed the polarisation at the input and the direction of the magnetic field. Here, $(80 \pm 3)\,\%$ of the light drives σ^+ transitions, which now corresponds to the

left peak. The relative peak height is within the estimated errorbars equal to the height measured in the top graph. We then analyse the light at the input in a linear basis and set the polariser in front of the input fibre to transmit vertically polarised light. The magnetic field is set to be positive again. We now get a σ^- component (left peak) of $(35 \pm 3)\,\%$. Here, less experiments per data point were performed, resulting in larger errorbars. The three measurements demonstrate that upon changing input polarisation and over the whole time that was needed to record the data, the mapping of input to output polarisation can sensibly be done assuming the same overall polarisation rotation imposed by the experimental setup.

Using the data acquired in these measurements we can now measure the stability of the polarisation at the atoms in the basis of atomic transitions, as done in figure 5.5. Here, the data acquired over the course of more than one hour is chopped into data sets acquired during intervals of ten minutes. During the whole measurement light driving σ^- transitions remains the dominant component in the beam. The setup is therefore stable enough to perform polarisation sensitive measurements with cold atoms.

5.4 Measuring intensity

To measure the transmission of light from the atoms to the detector, we make use of the characteristic reduction of the relative absorption when approaching the atomic saturation intensity I_{sat}. The scattering rate then scales with the intensity I as

$$\gamma_{sc}(I) = \frac{\Gamma}{2} \frac{I/I_{sat}}{1 + I/I_{sat}}. \tag{5.5}$$

The intensity I varies across the trench. Assuming again a Gaussian profile with radial symmetry and intensity $I(r,z) = 1/(\epsilon_0 c) \times |E_g(r,z)|^2$ the effective scattering rate is

$$\gamma_{sc} = \frac{\pi\Gamma}{V} \int_0^\infty r dr \int_0^{z_L} dz \frac{I(r,z)/I_{sat}}{1 + I(r,z)/I_{sat}}. \tag{5.6}$$

where V is the mode volume of the beam. The peak intensity I_0 is linked to the light power by $P = \pi I_0 w_w^2/2$. With this scattering rate we can write

the fractional absorption as

$$\alpha(I) = \frac{2\hbar\omega_a\gamma_{sc}}{\pi w_w^2 I} V N_D, \tag{5.7}$$

where the mode volume drops out again. For $\alpha(I \to 0)$ equation 5.4 is recovered. The only parameter still to be determined is I_{sat}.

The atomic saturation I_{sat} depends on the atom's hyperfine state m as well as on the polarisation of the light. Taking the magnetic field, which is parallel to the waveguides, as the quantisation axis, σ^+ and σ^- transitions can be addressed. Each data point in figure 5.6 is an average over experiments taken over the course of a few hours. When these experiments were done, no effort was taken to stabilise the polarisation. Hence, the fibres could slightly move while experiments were performed. This changes the polarisation of light at the atoms, which might therefore be slightly different for any single realisation of the experiment. The polarisation is therefore unknown and adds an uncertainty to the measured transmission. The fitting parameter I_{sat} is mainly determined by experiments at higher intensity, where each atom scatters several photons. This justifies the assumption, that the distribution of hyperfine Zeeman states has reached the steady state as a result of optical pumping. To calculate the effective saturation intensity we will calculate the scattering rate for the steady state as a function of the relative amount of light driving σ^+ and σ^- transitions.

The steady state distribution ν of atoms among the magnetic sublevels of the $F_g = 2$ ground states (ν_g^i, $i = -2...2$) and $F_e = 3$ excited states (ν_e^i, $i = -3...3$) in a light field with a fractional intensity of $\sigma^\pm$ light of $\eta^\pm$ ($\eta^+ + \eta^- = 1$) can be calculated solving the rate equations

$$0 = I \sum_{\Delta=-1,+1} \eta^\Delta \left(\nu_e^{i+\Delta} - \nu_g^i\right) S_i^{i+\Delta} + (2F_g + 3) \sum_{\Delta=-1,0,+1} \nu_e^{i+\Delta} S_i^{i+\Delta} \tag{5.8}$$

$$0 = I \sum_{\Delta=-1,+1} \eta^\Delta \left(\nu_g^i - \nu_e^{i-\Delta}\right) S_i^{i+\Delta} - \nu_e^i \tag{5.9}$$

The S_m^n are the square of the Wigner $3j$ symbols and are related to those defined in chapter 3 as $S_m^n = j_3(0, 1/2, 2, m, 1, 3/2, 3, n)^2$. Rates are normalised to Γ. With the steady state distribution of ground states ν_g^i we can

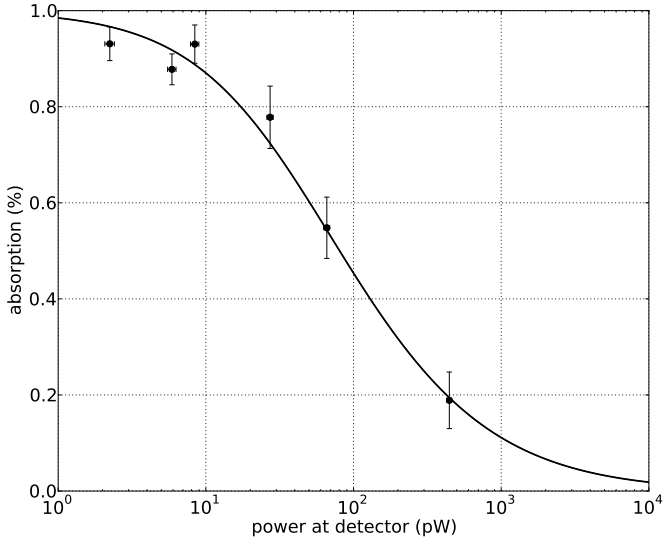


Figure 5.6: Measurement of the atomic saturation. The fitted saturation power is (26 ± 3) pW, indicating a coupling efficiency at the waveguide-fibre interface of $(16 \pm 6 \pm 2)$ %.

now calculate the scattering rate:

$$\gamma(\eta^+, \eta^-) = \sum_{i=-2}^{2} \sum_{\Delta=-1,+1} \eta^{\Delta} \nu_g^i S_i^{i+\Delta} \tag{5.10}$$

Since the saturation intensity for the cycling transition is know to be $I_{sat}^{cyc} = 16.6\,\mathrm{pW}/\mu\mathrm{m}^2$ [1], we can infer the saturation intensity for the chosen polarisation.

If the polarisation was completely random in each shot, the saturation intensity would be:

$$I_{sat} = I_{sat}^{cyc} \int_0^1 d\eta^+ \frac{\gamma(1,0)}{\gamma(\eta^+, 1-\eta^+)} = 22.4\,\frac{pW}{\mu m^2}. \tag{5.11}$$

Since the polarisation is more likely to explore only a subspace of the Bloch sphere, the correct saturation intensity required for our experiments has a value and uncertainty of $(22 \pm 8)\,\mathrm{pW}/\mu\mathrm{m}^2$, given by the extreme situation where the light polarisation only explores a small subspace of the two poles of the sphere where the light is purely left- or right-hand polarised at the

atoms or a small subspace around the equator, which corresponds to an equal mixture of the two polarisation components. This effective saturation intensity translates into an expected saturation power of $P = I_{sat}\pi w_w^2/2 = (163 \pm 59)\,\mathrm{pW}$. The fraction of this power and the power measured at the avalanche photodiode gives the transmission efficiency of light from the atoms to the detector.

Figure 5.6 shows an example of a measurement used to infer the transmission efficiency. Using neutral density filters in front of the SPAPD, we are able to explore intensities ranging over three orders of magnitude. Each data point averages over many experimental cycles, ranging from a few tens for data points at low intensities to some hundreds at high intensities. The number of experiments per data point where chosen to result comparable error bars for all data points. Error bars again indicate 1σ statistical uncertainties for Poissonian light, including corrections for the detector dead time.

A saturation curve using a saturation power of (26 ± 3) pW fits the data, indicating a transmission of about $(16 \pm 6 \pm 2)$ % from trench to SPAPD, where the first error is due to the unknown polarisation and the second error due to the measurement. Note, that this experiment was performed on the first generation atom chip with a much lower transmission efficiency than the chip currently in use (see chapter 4).

The uncertainty on this measurement can significantly be reduced by carefully determining the polarisation of the light at the atoms. This can be done by measuring how the polarisation of light transfers from the input to the output and measuring how this transfer changes when atoms are present in the trench. This was not done yet but can be done when required.

5.5 Using magnetic traps

The next step towards a trapped atomic sample in the trench is to transfer the atoms into a magnetic trap and move those atoms towards the trench. To do so, the magnetic trap is loaded about 1 mm from the trench. Then, the current in the Z wire is decreased while at the same time the current in the bias wires is increased. This moves the trap towards the trench and increases the trap frequencies, while the trap bottom field remains roughly constant. The parameters of the initial and final trap are shown in table

5.1. The field ramps take 6 ms. After the ramp is completed, the current through the bias wires and the Z wire is switched off, removing all gradient fields in less then 1 ms. The offset field from the coils outside the chamber are left on as they cannot be switched fast enough. The atoms then find themselves in a homogeneous offset field of 1.3 mT.

Parameter	Initial	Final	Unit
Radial trap frequency	31	26	Hz
Axial trap frequency	183	515	Hz
Centre field	0.87	0.53	T
Distance below surface	857	-67	μm

Table 5.1: Parameters of magnetic trap for current values before and after the compressing phase. The values are results of a simulations but agree with experimental observations.

When monitoring the light transmitted through one of the waveguides during such an experimental cycle, a time traces as shown in figure 5.7 is recorded. Here, $t = 0$ denotes the time when the trap is switched off. The two curves shown correspond to the peak of the spectrum in the respective colour in figure 5.8. The latter figure shows the peak absorption before (blue curve) and after (green curve) the trap is switched off. Both maxima correspond to the resonance of the $|F, m\rangle = |2, 2\rangle \rightarrow |F', m'\rangle = |3, 3\rangle$ cycling transition. The difference in the laser frequency corresponds to the expected shift in the cycling transition when going from a magnetic field of $0.5\,\mu$T before the trap is switched off to a magnetic field of $1.3\,\mu$T, which is the residual offset field after the trap is switched off.

The two curves are addressed by different polarisation components of the light. Since the magnetic field is perpendicular to the propagation direction of the light, the two linear polarisation components parallel and perpendicular to the magnetic field address either π transitions or a superposition of σ^+ and σ^- transitions, respectively. If there is no special effort taken to keep the fibres mechanically stable, which is the case for these experiments, the polarisation drifts between the two linear components over the course of the 150 min that were necessary to acquire the data. Therefore, in some experimental runs the light mainly addresses the cycling transition in the magnetic trap whereas in others the cycling transition in the homogeneous offset field is addressed, depending on which polarisation is present during the specific experiment. Since the cycling transition is by far the

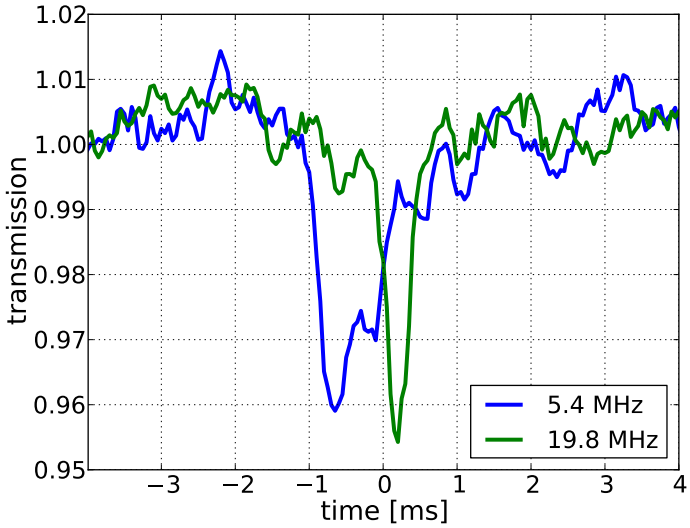


Figure 5.7: Averaged fractional absorption as a function of time relative to the switch-off of the magnetic fields gradients. The two curves are recorded at the maximum of the two frequency peaks in figure 5.8. The peak at lower frequencies corresponds to the earlier peak on the time trace.

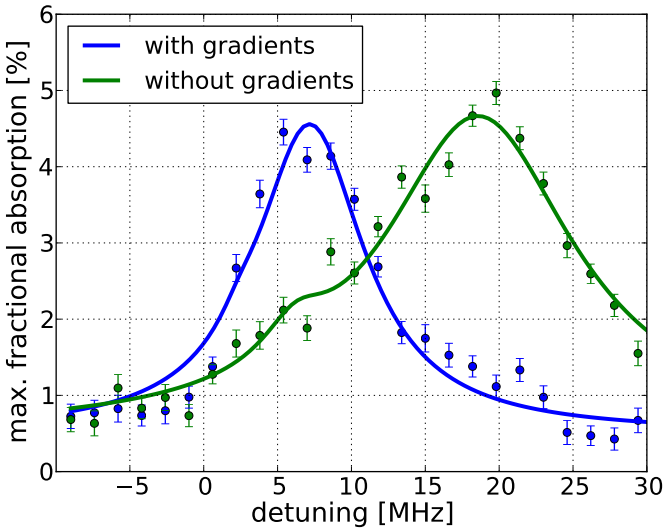


Figure 5.8: Spectrum showing the maximum absorption seen on the light transmitted through a waveguide when moving the trap into the trench. The absorption data is independently analysed before (blue curve) and after (green curve) the trap is switched off. The first peak corresponds to the cycling transition in the trap with a trap bottom field of 0.5 mT in z direction (along the trench), the second peak to the cycling transition in the homogeneous offset field of 1.3 mT in y direction (direction of gravity). The second peak also shows contributions of the π transition.

strongest transition, both peaks occur on the graph when averaging over all experiments.

When the magnetic trap is switched off, the direction of the magnetic field rotates by 90° in the plane perpendicular to the propagation of light. The role of light addressing the π transitions or a superposition of σ^+ and σ^- transitions swaps. Since the σ^+ transition is by far the strongest, this peak will always dominate the spectrum.

The data acquired without field gradients, that is in a homogeneous offset field, shows a visible contribution of π transitions. π transitions pump the atoms out of the trapped state (see chapter 6). In a homogeneous field this makes no differences as the atoms are not trapped anyway. In the gradient field of the trap, however, the depumping from the trapped state enhances the loss of atoms and therefore reduces the π peak.

The measured peaks are much broader then the natural linewidth of the transition. This is because the measurements were not done in a static and homogeneous magnetic field. The decay of the fields after switch-off varies from shot to shot. Also, atoms at different positions in the trap see a different magnetic field. Since the resonance frequency for the cycling transition depends on the magnetic field, these fluctuations broaden the peak.

The maximum fractional absorption that we saw in these experiments is 13 %, which corresponds to an atomic density of $0.02\,\text{atoms}/\mu\text{m}^3$. This makes about 2.3 atoms in the waveguide mode on average. We are now trying to increasing the density by evaporatively cooling the atoms before they are moved towards the trench.

6 Detecting atoms with frequency-synthesised light

The work presented in this chapter is published in a focus issue on "Modern Frontiers of Matter Wave Optics and Interferometry" of the New Journal of Physics with the title "Minimally destructive detection of magnetically trapped atoms using frequency-synthesized light" [59]. Our technique uses a light beam synthesized from two frequencies as a probe to measure the density of atoms. The frequencies are tuned around the atomic resonance and produce an RF beat signal when incident on a photo diode. When the beam propagates through an atomic sample, the two frequency components pick up different phase shifts which results in a phase shift of the beat signal. This phase shift is proportional to the column density of atoms and can be measured with a phase sensitive detector.

The technique is optimised for minimally destructive measurements, meaning that the uncertainty in the measured column density is minimised for a given number of scattered photons per atom. In fact, an off-resonant phase shift measurement cannot improve the signal-to-noise ratio for a fixed number of scattered photons compared to a resonant absorption measurement (see chapter 1). The general limit for both types of measurements is shown to be identical [29], even if an arbitrary number of coherences between atomic levels and an arbitrary number of light fields is used [32].

One advantage of the phase shift measurement is revealed when an optically thick sample (as for example most Bose-Einstein condensates (BECs)) is to be probed. Here, a weak resonant light beam would almost totally be absorbed when passing through the atoms. In a phase measurement on the other hand the probe beam can be adjusted to see an arbitrarily low optical density by simply varying the detuning. This dispersive detection has the advantage that it can be repeated many times on the same cloud. It is therefore sometimes called "non-destructive". Non-destructive detection

by imaging the optical phase shift has been achieved on BECs via the related but different methods of dark ground imaging [60] and phase contrast imaging [61, 62, 63, 64].

Non-destructive optical detection permits multiple measurements of the same trapped atomic sample with repetition rates in excess of 100 kHz; faster than the natural timescales for density evolution in a trapped ultracold cloud set by the trapping frequencies [63, 65]. Consequently the method can be used to explore dynamics in an atomic cloud or to monitor the time evolution of matter wave interference, e.g. in a BEC. With rapid readout, active feedback on the cloud becomes feasible, opening possibilities for cooling the motion [66, 67] or preparing novel quantum states.

Interferometric detection often involves beams that are spatially separated, with one path going through the atom cloud. It is, however, technically demanding to maintain adequate mechanical stability [65]. Our two-frequency method allows the beams to travel on a common path while still accumulating a differential phase shift through the frequency-dependence of the atomic polarisability [68].

Previously, frequency modulation (fm) sidebands have been used to provide the additional frequencies. Atoms dropped from a MOT have been seen using fm sideband detection with a current-modulated diode laser [69] or electro-optic modulation (EOM) [70], and within a MOT, atoms have been probed using EOM to produce fm sidebands [71]. These fm methods produce (at least) three frequencies — a carrier and two sidebands — rather than two. One detection strategy is to tune all three frequency components above (or below) the atomic transition, then the sideband closest to resonance has the main phase shift and the strong carrier acts as the local oscillator. This has the drawback that it induces a light shift in the energy of the atoms [72]. When measuring a Bose-Einstein condensate this phase shift might excite unwanted phonons [73]. It can be eliminated by placing the sidebands symmetrically around the atomic resonance, but then the cloud is heated by the resonant carrier. In order to detect atoms in an optical lattice, Lodewyck *et al.* [74], using an EOM, have suppressed the carrier by choosing a specific, high modulation index (2.4), but this has the effect of putting power into higher-order sidebands that contribute inefficiently to the signal. All the methods described above are ultimately limited by the photon shot noise [75, 29], leading to the standard quantum limit. There

are also methods to go below that limit [70, 76, 77, 78, 79].

Our technique uses an acousto-optical modulator (AOM) to synthesise the required two frequencies without any other sidebands. We can therefore balance the two frequencies around the atomic resonance, cancelling the mean dipole force on the probed atoms. The dual-frequency light is coupled into an optical fibre that allows easy delivery to a remote site where cold atoms are to be measured. We find that the relative phase of the two beams is exceedingly robust when transported in this way. Using a phase sensitive detector to read out both quadratures of the observed beat note, we study the phase noise and compare this with the expected noise floor due to Poisson statistics of the coherent laser light. We then apply this two-frequency interferometer to the dispersive detection of magnetically trapped ^{87}Rb atoms. We measure the spectrum of the phase shift induced by the atoms and investigate the extent to which the measurement is non-destructive. To demonstrate the utility of the method, we non-destructively measure the centre-of-mass oscillations of a magnetically trapped atom cloud. Finally, I describe how to optimise the detection scheme, using the figure of merit based on sensitivity and destructiveness already mentioned in chapter 1.

6.1 Frequency-synthesising light

Figure 6.1 shows the main elements of the experimental apparatus. Light entering the setup (at the top of the diagram) at frequency f_L is taken from the reference laser and tuned close to the $F = 2 \rightarrow F' = 2$ transition by an acousto-optical modulator (not shown) in a double-pass configuration, which can also be used to fine-tune f_L. The collimated, linearly polarized laser beam passes first through a half-wave plate ($\lambda/2$) that adjusts the polarization to be vertical. This light is directed by the polarizing beam splitter (PBS) through lens L_1, AOM and lens L_2 (which re-collimates it). Retro-reflection through the quarter-wave plate rotates the linear polarization to horizontal. After passing again through L_2, AOM and L_1, the light is transmitted by the PBS. A final $\lambda/2$ rotates the polarization to any desired angle before the light is coupled into a single-mode fibre for transmission to the atom cloud.

The AOM is driven by two, passively-summed RF signals produced by a four-channel direct digital synthesizer (Novatech DDS 409B) with fre-

quencies rf_1 and rf_2. After the first pass, the unshifted zero order beam is blocked. Light leaving the double-pass setup at the polarising beam-splitter cube contains frequencies $f_0 \pm \delta f$, where $f_0 = f_L + rf_1 + rf_2$ and $\delta f = |rf_2 - rf_1|$. However, there are also two side beams with frequency f_0. To spatially separate these beam from the central beam, the lenses L_1 and L_2 were chosen with a relatively large focal length of 400 mm, which suppresses unwanted light coupling into the fibre to below 1 % for $\delta f > 10$ MHz. The RF amplitudes are adjusted to balance the power of the two frequency components in the light beam by maximising the detected beat note amplitude.

The fibre guiding light from the synthesis module (A) to the experimental chamber (C) is a single mode fibre to ensure the best spatial mode overlap of the two frequency components. The light leaving this fibre is collimated, linearly polarised (LP) and then focused by a lens (L_3) of 250 mm focal length to a waist of $w_0 = 55$ μm. After passing through the magnetic trap, the beam is re-collimated and coupled into a multi-mode fibre, guiding up to 90% of the light to the detector in the demodulation module (B). The detector is a low-noise analogue avalanche photo-diode (AAPD) with an inbuilt transimpedance amplifier (Analog Modules 712A-4[1]).

The two frequency components produce a beat on the AAPD of $f_{\text{beat}} = 2\delta f$, which is set to 60 MHz in the experiments presented here. This signal is split into two and both parts are mixed down to DC using reference outputs from the DDS. These outputs are phase coherent with the difference of the two RF signals at rf_1 and rf_2 driving the AOM. The two reference signal have a relative phase shift of $\pi/2$. The two mixed signals are low-pass filtered, giving the in-phase component V_i and the quadrature component V_q of the beat note. The filter contains a second-order active and a first-order passive stage and has a 3 dB bandwidth of 650 kHz. The signals are recorded with a NI PCI-6133 14 Bit, 2.5 MS/s ADC card with an analogue bandwidth of 1.3 MHz. The photo-diode signal is also directly low-pass filtered by the ADC and recorded (V_0) to monitor the mean light power on the AAPD.

[1]The module has a bandwidth with a specified -3 dB point of 80 MHz and a noise equivalent power of 20 fW/$\sqrt{\text{Hz}}$. It is AC coupled, filtering signals slower than 230 Hz. Unfortunately, it is no longer available, but we were informed that the next version 712B-4 is being developed.

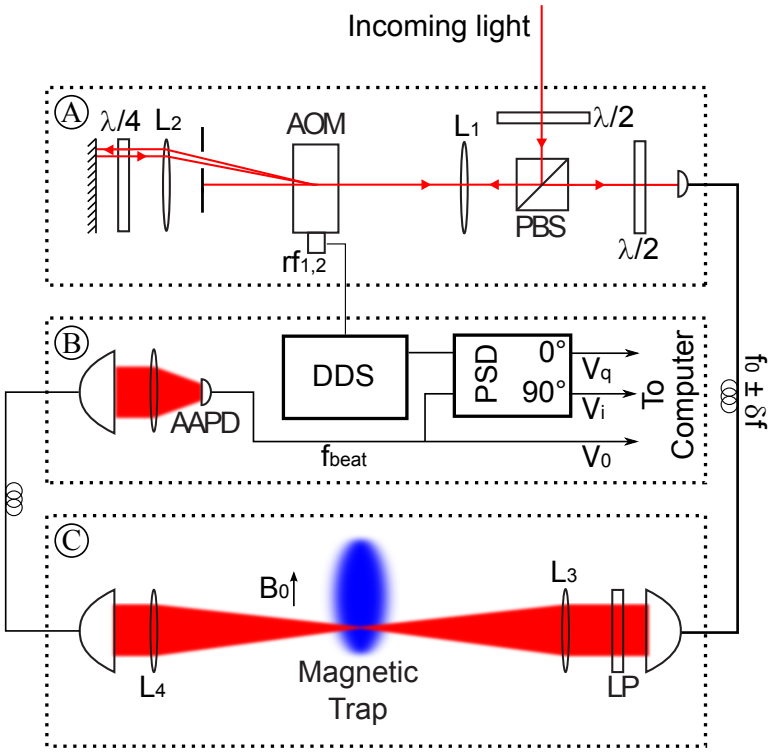


Figure 6.1: Experimental setup. (A) Synthesis: The incoming beam is modulated by a double-pass acousto-optical modulator (AOM) driven with two frequencies rf_1 and rf_2, which makes use of a quarter-wave plate ($\lambda/4$) and a polarising beam splitter cube (PBS). The output is coupled into a single-mode fibre. (C) Experimental chamber: The beam leaving the fibre is collimated, passed through a linear polariser (LP) and focussed (L_3) onto the magnetic trap (MT), re-collimated (L_4) and coupled back into a multi-mode fibre. (B) Demodulation: Light is detected with an analogue avalanche photo-diode (AAPD). A phase sensitive detector (PSD) determines the in-phase and quadrature part of the beat note signal. Modulation and reference signals are produced by the same multi-channel direct digital synthesizer (DDS), and therefore phase stable. The PSD outputs as well as the output of the AAPD are recorded by a computer controlled analogue-to-digital converter (ADC).

6.2 Identifying noise sources

The noise components associated with the detection process can be divided into two categories. The first and fundamental one stems from the fluctuations of incoming photons due to counting statistics, the photon shot noise. It scales with the square root of the photon number N and has a flat (white noise) spectrum up to infinite frequencies. The detected noise spectrum is of course limited by the bandwidth of the detector. An example of a spectrum dominated by this kind of noise is presented in the upper graph of figure 6.2. This spectrum is recorded by sampling the output of the AAPD with the ADC card at a bandwidth of 200 kHz. The AAPD is illuminated with light, so that the photon shot noise dominates the spectrum.

The second significant noise is electronic noise in both the amplifier and the phase sensitive detector. It is independent of the photon number and its spectral density decays as approximately $1/f$ [80]. The electronics also produce white noise, which becomes dominant for large f. A spectrum dominanted by electronic noise is plotted in the lower graph of figure 6.2, taken in the same way as the upper graph but with no light hitting the AAPD. The electronic noise can in general be lowered by improving the electronics.

When increasing the photon number the shot noise increases and will at some point dominate over the electronic noise. The quality of a detector can be characterised by the signal power for a signal-to-noise ratio of 1 at a given bandwidth, which is known as the noise equivalent power (NEP).

6.2.1 Expected noise

In a light pulse of duration T, N_γ photons arrive at the detector on average. The number in each shot will fluctuate around N_γ according to counting (Poissonian) statistic. This Poissonian distribution has standard deviation $\sigma_\gamma = \sqrt{N}_\gamma$. Signal and fluctuations are amplified equally through the several deterministic amplification stages in the diode and the electronics. The randomness of the avalanche process will further increase the fluctuations. Since each avalanche contains a discrete number of charge carriers, this amplification can be again characterised using Poissonian statistics, quantified by the excess noise factor $F = \left\langle G_a^2 \right\rangle / \left\langle G_a \right\rangle^2$, where G_a is the ensemble of fluctuating amplifications and $\langle \cdot \rangle$ denotes the ensemble average. In the limit

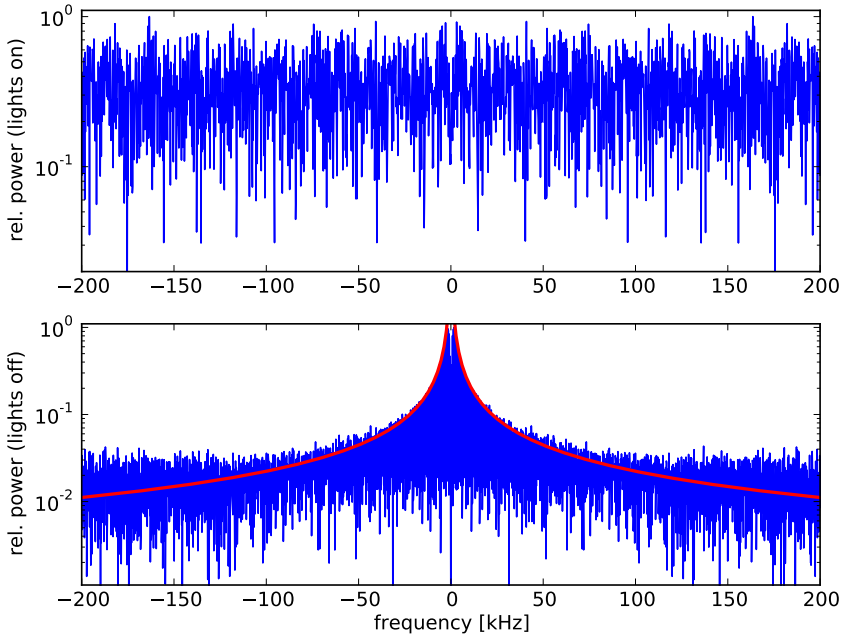


Figure 6.2: Noise spectrum of the AAPD. The upper graph shows the spectrum recorded with 22 nW of light incident on the photo-diode, where the photon shot noise is the dominant noise source. The acquisition bandwidth is 200 kHz. The lower graph shows the Fourier spectrum of the AAPD signal when no light is hitting the diode. Here, the $1/f$ characteristics (red line) of electronic noise dominates the spectrum up to 100 kHz.

of a deterministic amplifier $F = 1$.

The next stage is a phase sensitive detector, decomposing the signal into the components in phase with and orthogonal to a reference signal. The noise on the two components is equal and independent of the phase angle between the input signal and the reference signal. We will therefore without loss of generality set the angle to be 0, which will make the in-phase signal V_i proportional to the demodulator input amplitude V_0 and leave the quadrature channel V_q with noise only ($\langle V_q \rangle = 0$, $\langle V_q^2 \rangle \propto \langle V_0^2 \rangle - \langle V_0 \rangle^2$). Defining the input signal as a positive definite sine wave $V_0 = A_0[1 + \cos(\omega_0 t)]$ (see below) which is in phase with the reference signal $V_r = A_r \cos(\omega_0 t)$ we may define the demodulator signal gain as

$$G_s = \frac{\langle V_i \rangle}{\langle V_0 \rangle} = \frac{\int_0^T A_0 A_r \left[1 + cos(\omega_0 t)\right] cos(\omega_0 t) dt}{A_0 \int_0^T \left[1 + cos(\omega_0 t)\right] dt} = \frac{1}{2} A_r \tag{6.1}$$

Since the noise has a white spectrum[2], we may write the noise signal as $V_n = A_n \int \cos(\omega t + \phi_\omega) d\omega$, with $\langle V_n \rangle = 0$ and $\sigma_n^2 = \langle V_n^2 \rangle$. ϕ_ω is a random phase between the Fourier components. The gain for the noise signal is then

$$G_n = \sqrt{\frac{\langle V_q^2 \rangle}{\langle V_n^2 \rangle}} = \sqrt{\frac{\int_0^T \int_0^\infty \left[A_r A_n cos(\omega t + \phi_\omega) cos(\omega_0 t)\right]^2 d\omega dt}{\int_0^T \int_0^\infty \left[A_n cos(\omega t + \phi_\omega)\right]^2 d\omega dt}} = \frac{1}{\sqrt{2}} A_r \tag{6.2}$$

In this sense the noise is effectively enhanced by a factor $\sqrt{2}$ compared to the signal gain defined above[3]. This result was independently verified using a Monte-Carlo simulation. Here, we model the random process of photon arrival at the diode and the triggered avalanche process and feed the resulting signals through the amplification, filtering and mixing processes as described above. The results of theses simulation and our measurement agree with the results of the above argument.

In the small phase angle approximation ($V_i \gg V_q$), we can write $\phi =$

[2] The detected noise is shot noise, which has a flat spectrum. The recorded noise spectrum is limited by the bandwidth of the detector.

[3] This factor mainly comes from the definition of signal as an amplification in amplitude whereas the magnitude of the noise is a root-mean-square (RMS) signal.

$\arctan(V_q/V_i) \approx V_q/V_i$. Summing up, the phase noise as a function of incident photons is:

$$\sigma_\gamma^2 = \frac{2F}{\eta}\frac{1}{N_\gamma} \tag{6.3}$$

The electronic noise sources are the dark count rate of the photo-diode in conjunction with the electronic noise of the amplifier, which has a gain of G_t. The manufacturer specifies this noise on the photo-current as a power spectral density $\tilde{\sigma}_B$. The total noise power detected is the power spectral density multiplied by the square root of the measurement bandwidth, which is in our case set by the pulse time $B = 1/(2T)$. Furthermore, the demodulator adds a voltage noise σ_D. Equipped with the right amplification factors, the electronic noise can be written as:

$$\sigma_e^2 = T\left(\frac{\tilde{\sigma}_B\lambda}{hc}\right)^2\frac{1}{N_\gamma^2} + \left(\frac{\sigma_d T}{e\eta\left\langle G_a\right\rangle G_t G_s}\right)^2\frac{1}{N_\gamma^2} \tag{6.4}$$

Finally, due to mechanical fluctuations in the double pass AOM setup, fluctuations of the optical path length σ_m are included, which limit the sensitivity at large photon numbers. Putting it all together, the expected standard deviation of the measured phase can be written as:

$$\sigma_\phi^2 = \sigma_\gamma^2 + \sigma_e^2 + \sigma_m^2 \tag{6.5}$$

6.2.2 Experiments

To measure the fluctuations, we average the in-phase $V_i(t)$ and quadrature $V_q(t)$ signals for 50 pulses of duration $T = 10\,\mu$s. For each pulse the average phase $\phi_k = \arctan(\bar{V}_q/\bar{V}_i)$ is determined[4], and the standard deviation $\sigma_\phi^2 = \left\langle\phi_k^2\right\rangle - \left\langle\phi_k\right\rangle^2$ is calculated. The low-pass filtered output voltage of the transimpedance amplifier $V_0(t)$ is also recorded and used to calculate the average photon number per measurement $\left\langle N_\gamma\right\rangle = \left\langle\bar{V}_0\right\rangle e\eta\left\langle G_a\right\rangle\lambda/(hc)$.

The result is plotted in figure 6.3. In the first graph (upper left) we plot the standard deviation of the recorded DC voltage from the photodiode against the mean DC voltage. Since the photodiode is AC coupled at 230 Hz, we switched the light at frequencies much faster than this low-pass cut-off

[4]We distinguish between ensemble average $\langle\cdot\rangle$ and time average $\bar{\cdot}$, the latter being the continuous version of the former. In the experiment, the acquisition is not really continuous but limited by the finite sample speed ($0.4\,\mu$s) of the analogue acquisition card.

to record the light amplitude. The dotted line shows the counting noise, scaling with the square root of the mean voltage. At low light levels the noise is dominated by the electronic noise of the transimpedance amplifier. Adding this electronic noise quadratically to the counting noise, the red curve fits the data quite well.

The second graph of figure 6.3 (upper right) shows the standard deviation of the recorded voltage at the in-phase (V_i) and quadrature (V_i) channel of the phase sensitive detector. Again, the counting noise level and the noise level including electronic noise is plotted. Here, the electronic noise level also includes noise from the demodulator electronics (see table 6.1 for values). The noise measured on V_i and V_q deviates from the expected noise level due to fluctuations on the laser power which adds correlated noise to both channels.

From the two output channels of the phase sensitive detector we can calculate the amplitude of the beat signal as described above. A graph showing the measured noise on this quantity as a function of the incident photon number as calculated from the recorded DC signal is shown in the lower left of figure 6.3. Here, the small angle approximation breaks down in the few photon limit, where $\sigma_e \gtrsim \sigma_\gamma$. Considering the limit of no input light, we can write the distribution of measured voltages V_i and V_q as

$$P(V_{i/q}) = \frac{1}{\sqrt{2\pi\sigma_D}} \exp\left(-\frac{V_{i/q}^2}{2\sigma_D}\right) \tag{6.6}$$

The expected fluctuations on the amplitude $\sigma_a^2 = \langle a^2 \rangle - \langle a \rangle^2$ can then be calculated as

$$\sigma_a^2 = \int_{-\infty}^{\infty}\int_{-\infty}^{\infty} \left(V_i^2 + V_q^2\right) P(V_i)P(V_q)dV_i dV_q - \left(\int_{-\infty}^{\infty}\int_{-\infty}^{\infty} \sqrt{V_i^2 + V_q^2} P(V_i)P(V_q)dV_i dV_q\right)^2 = \left(2 - \frac{\pi}{2}\right)\sigma_D$$

With this additional term the amplitude data fits the few and many photon regime very well, but slightly underestimates the noise in the intermediate regime.

Finally, figure 6.3 shows the standard deviation in the inferred phase as

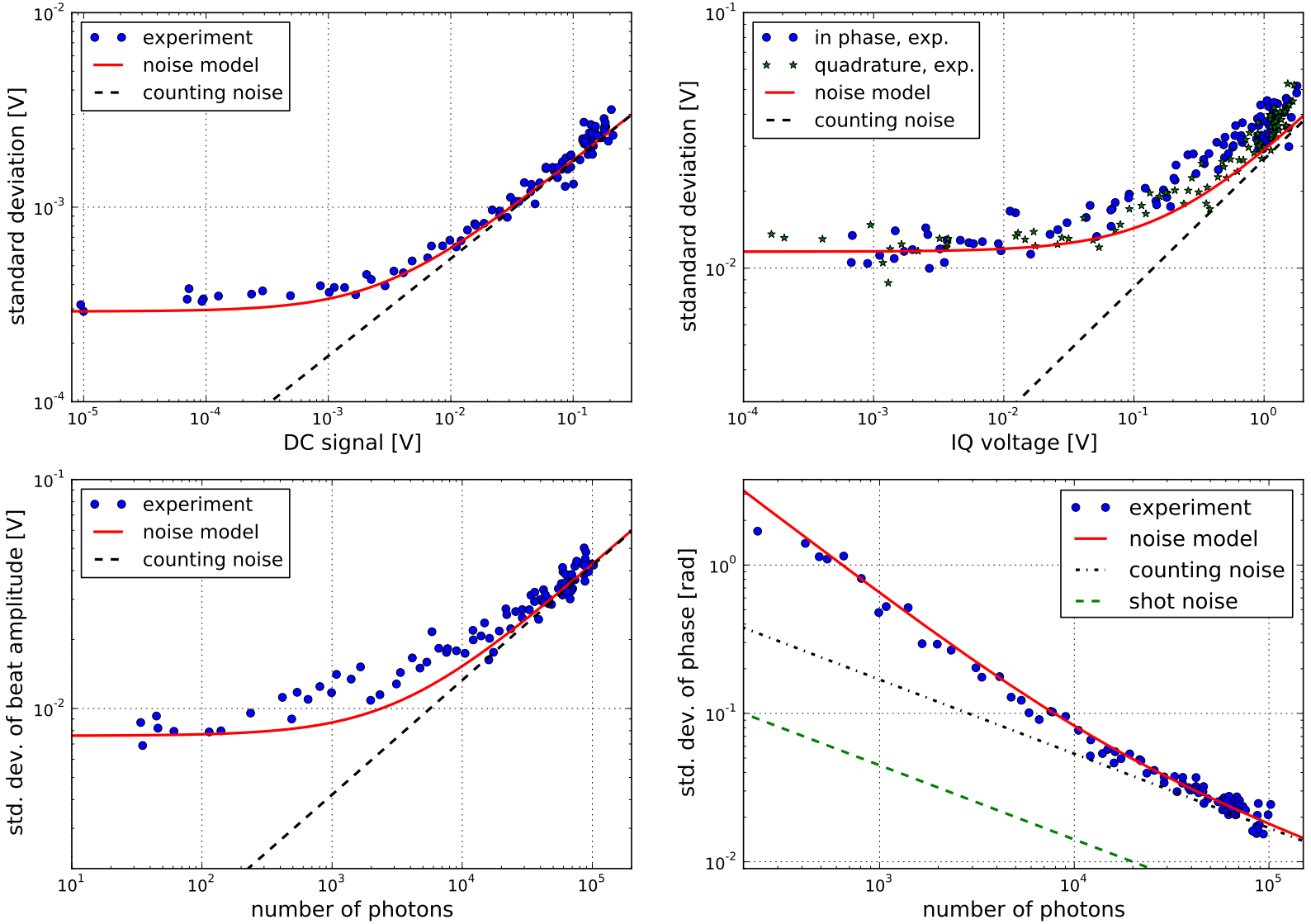


Figure 6.3: Fluctuations of signals from 50 light pulses, each of 10 μs duration. The graphs show the pulse-to-pulse standard deviation of the filtered AAPD output V_0 (top left), the demodulator output V_i and V_q (top right) and the inferred quantities of beat note amplitude (bottom left) and phase (bottom right). Along with the experimental data, the relevant parts of the noise model given in equation 6.5 and the counting ($\sqrt{N}$) noise is plotted. The phase noise graph also contains a line indicating the pure photon shot noise limit without the excess noise introduced by the avalanche process.

Parameter	Symbol	Value	Source
PD quantum efficiency	η	0.77	specifications
Avalanche gain	G_a	150	specifications
Excess noise factor	F	11 ± 2.0	measurement
Transimpedance gain	G_t	$1.12\,\mathrm{MV/A}$	specifications
Demodulator gain	G_D	12.0 ± 0.1	measurement
Amplifier NEP	$\tilde{\sigma_B}$	$16\,\mathrm{fW}/\sqrt{\mathrm{Hz}}$	specs & measured
Demodulator voltage noise	σ_D	$10.5\,\mathrm{mV}$	fit (few photons)
Mechanical phase noise	σ_m	$2\,\mathrm{mrad}$	fit (many photons)

Table 6.1: Parameters of the beat note detection system necessary to calculate the expected noise level. The table also indicates the origin of each value. The product of sensitivity of the diode and transimpedance gain of the AAPD ($G_t S = G_t e \eta \langle G \rangle_a \lambda/(hc)$) was confirmed experimentally.

a function of the inferred photon number. Here, the photon counting shot noise level is indicated by the dash-dotted line, the counting noise including the avalanche excess noise is marked by the dashed line and the solid line shows our noise model taking into account all the noise sources as specified in table 6.1, including the mechanical noise which becomes dominant at larger photon numbers. The full model fits the measured noise very well.

6.2.3 Discussion

The $\sqrt{N}$ noise (photon counting shot noise and avalanche excess noise) is the dominant noise source on our phase measurements down to 580 detected photons per μs. At lower photon numbers, the demodulator electronic noise is dominant. If we were able to halve the noise on the demodulator so that it became comparable to the APD base noise, $\sqrt{N}$ noise would be dominant down to 200 detected photons per μs.

The optical phase noise becomes dominant at frequencies below 3 Hz (as measured with a continuous light beam). This noise originates from mechanical drifts in the double-pass AOM setup, where the two frequency components propagate on different paths. This noise could be eliminated with active phase stabilisation, but that was not yet necessary for our applications, since the noise is small and drifts are slow. Once the two frequencies are combined in the fibre, we can shake it 'till the wheels fall off without observing additional phase noise on the demodulator output.

6.3 Phase-shift signals

The phase shift and the absorption of light due to the atomic sample can readily be calculated from equations 3.28 and 3.27. In the experiments presented below, light propagates at right angles to the magnetic field axis (see figure 6.1, part C). The light component polarised parallel to the magnetic field drives therefore purely atomic π transitions ($m' - m = 0$). The light component polarised perpendicular to that axis is seen by the atoms as a coherent and equal superposition of σ^+ and σ^- light. For convenience, these polarisations will be referred to as parallel and perpendicular polarised light, respectively. All other light polarisations can be decomposed into these two linear modes and transferred into the atomic frame of reference accordingly.

In the magnetic trap, almost all atoms are in the $|F, m\rangle = |2, +2\rangle$ state[5] and we only have to consider transitions from this ground state level. Neglecting saturation effects, equations 3.28 and 3.27 simplify to

$$\alpha(f) = \frac{7}{2}\left(\sum_{m'=1}^{3} p_{(m'-2)} J(2,2;3,m') \frac{\Gamma^2}{4\delta(2,2;3,m')^2 + \Gamma^2}\right) \frac{3\lambda^2 N_c}{2\pi} \tag{6.7}$$

$$\phi(f) = 7\left(\sum_{m'=1}^{3} p_{(m'-2)} J(2,2;3,m') \frac{\Gamma\delta(2,2;3,m')}{4\delta(2,2;3,m')^2 + \Gamma^2}\right) \frac{3\lambda^2 N_c}{2\pi} \tag{6.8}$$

with $J(2,2;3,m')$ denoting the square of the Wigner $3j$ symbols defined as

$$J(2,2;3,m') = \begin{pmatrix} 3 & 1 & 2 \\ -m' & m'-2 & 2 \end{pmatrix}^2. \tag{6.9}$$

The quantities measured in the following experiments are the relative phase shift

$$\theta(f_1, f_2) = \phi(f_1) - \phi(f_2) \tag{6.10}$$

between two light beams of equal power and frequencies f_1 and f_2 and the change in the magnitude of the beat signal. The incident complex electric fields $E_1(t) = E_1^0 \exp\left[-\mathrm{i}\left(2\pi f_1 t + \phi_1\right)\right]$ and $E_2(t) = E_2^0 \exp\left[-\mathrm{i}\left(2\pi f_2 t + \phi_2\right)\right]$

[5] Quantisation axis and symbols are according to chapter 3, but the quantum numbers for I and J are dropped and we label the ground states $|F, m\rangle = |0, 1/2, F, m\rangle$ and excited states $|F', m'\rangle = |1, 3/2, F', m'\rangle$ as well as detunings $\delta(F, m; F', m') = \delta(0, 1/2, F, m; 1, 3/2, F', m')$.

will produce a detected signal $I(t)$ of

$$\begin{aligned} I(t) &= \left[E_1(t) + E_2(t)\right]\left[E_1(t) + E_2(t)\right]^* \\ &= \left(E_1^0\right)^2 + \left(E_2^0\right)^2 + 2E_1^0E_2^0\cos\left[\left(f_1 - f_2\right)t + \phi_1 - \phi_2\right]. \end{aligned} \tag{6.11}$$

While the first two terms cause a constant offset, which is not detected since the AAPD is AC coupled, the last term is the beat with amplitude $2E_1^0E_2^0$ and phase shift $\theta(f_1, f_2)$.

Further, let us consider what happens to the beat amplitude when the atoms attenuate the light. Let each frequency component be attenuated by a fraction $\alpha(f_i)$, $i = 1, 2$ to $E_i(t) = \left[1 - \alpha(f_i)\right]E_i^0\exp\left(-\mathrm{i}2\pi f_i t\right)$. The beat signal now reads

$$\begin{aligned} I(t) = &\left[\left(1 - \alpha(f_1)\right)E_1^0\right]^2 + \left[\left(1 - \alpha(f_2)\right)E_2^0\right]^2 \\ &+ 2\left[1 - \alpha(f_1)\right]\left[1 - \alpha(f_2)\right]E_1^0E_2^0\cos\left[\left(f_1 - f_2\right)t\right], \end{aligned} \tag{6.12}$$

with $\phi_1 = \phi_2 = 0$ for simplicity. The beat is thus reduced by a factor

$$\begin{aligned} 1 - \tau(f_1, f_2) &= \left[1 - \alpha(f_1)\right]\left[1 - \alpha(f_2)\right] \\ &= 1 - \left[\alpha(f_1) + \alpha(f_2) + \alpha(f_1)\alpha(f_2)\right]. \end{aligned} \tag{6.13}$$

For small absorptions ($\alpha_i \ll 1$) the last term can be neglected and the reduction of the beat signal is simply $\tau(f_1, f_2) \approx \alpha(f_1) + \alpha(f_2)$.

Experimental sequence and results

The following experiments are done in a magnetic trap with a field minimum 2.5 mm from the wire surface[6] and a trap bottom field of 0.6 mT. Trap frequencies are 75 Hz $\times$ 75 Hz $\times$ 20 Hz. The trap is loaded with 2.4 million atoms at a temperature of 60 μK.

The phase shift Θ and absorption τ of light is measured for various values of the central frequency f_0 and plotted in figure 6.4. The linear polariser in

[6] This trap is quite far from the chip compared to experiments done to load atoms into the trench. This is because optical access for the free-space probe beam is limited by the V-groove assemblies connecting the fibres to the waveguide chip. At the position of the trap we can only create rather weak magnetic field gradients, resulting an atom cloud with a low optical density. We have done experiments with a trap about 1 mm from the chip surface by bouncing the probe beam off the waveguide chip, which improves signals by more than a factor 4.

figure 6.1 is set to give perpendicular polarisation. For each data point in figure 6.4 50 light pulses with a duration of 10 μs and a photon number of $\approx 4 \times 10^5$ are sent through the atomic cloud with a repetition rate of 1 kHz and the in-phase $V_i(t)$ and quadrature $V_q(t)$ components of the detected beat signal are recorded. After 25 pulses the trap is switched off, releasing the atoms. The measured voltages $V_q(t)$ and $V_i(t)$ are averaged for each pulse and the phase $\theta_k = \arctan(\bar{V}_q/\bar{V}_i)$ and amplitude $A_k = \sqrt{\bar{V}_i^2 + \bar{V}_q^2}$ are calculated. The atom-induced phase shift plotted in the upper graph of figure 6.4 is taken to be the difference in the average phase of the light pulses before and after the trap is switched off. We discard four pulses around the switch-off to discard short-term dynamics and electronic noise due to the switch-off. The difference of the beat signal amplitude is, in the case of small absorption, proportional to the sum of the absorption of the single light beams (see equation 6.12). The absorption normalised to the average magnitude of the beat in absence of atoms is plotted in the lower part of figure 6.4. We averaged several measurements done in the course of a few milliseconds to compensate oscillations of the atoms in the magnetic potential (see below).

The solid red lines in figure 6.4 show a fit to the model described by equations 6.8 and 6.7. The atom-induced phase shows a dispersion feature when either of the two frequency components approaches resonance. This is mainly due to the σ^+ transition, since the σ^- transition is a factor 15 weaker. The only free parameters of the fit are the frequency offset and the atomic column density $N_c = (2.2 \pm 0.6) \times 10^{12}$ m^{-2}. This value is independently obtained with standard absorption imaging as described in chapter 4.

Our two-frequency technique can be used to measure the oscillation frequency of trapped atoms in a single experimental run by making repeated observations of the optical phase shift. An example is shown in figure 6.5. The oscillations are excited by placing the atoms off centre when they are passed from the MOT to the magnetic trap. The frequency and the damping of these oscillations can be measured by observing the density variations in the probing volume for a few cycling periods. This is done using 120 light pulses of 50 μs with 2×10^6 photons each at a repetition rate of 1 kHz. In this experiments, the frequency bands are separated by 60 MHz, with a central frequency detuning corresponding to +17.3 MHz in figure 6.4. The

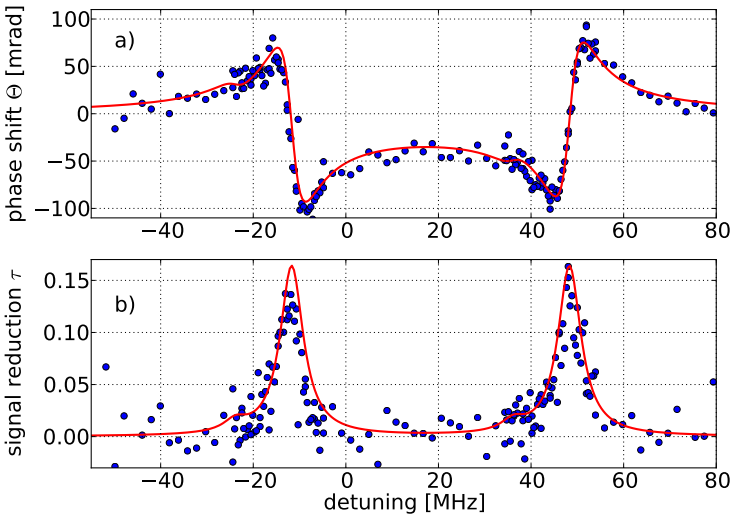


Figure 6.4: Measurement of phase shift θ and amplitude reduction τ of an optically-carried 60 MHz beat note signal due to atoms in a magnetic trap as a function of detuning relative to an arbitrary zero. Light is polarised perpendicular to the magnetic field. The solid lines are fits of phase shift and absorption calculated from equation 6.8 and 6.7. Fitting parameters are the magnetic field, frequency offset and the atomic column density $N_c = (2.2 \pm 0.6) \times 10^{12}$ m^{-2}.

solid line in figure 6.5 shows a fit of a damped sinusoidal function to the data points. The oscillation frequency is inferred to be (21 ± 1) Hz and the damping coefficient is 0.26 s^{-1}. The damping is mainly caused by the anharmonicity of the magnetic trapping potential with only minor contributions due to atom loss. The atom loss can be measured directly if we increase the number of photons per pulse as described in the next section.

6.4 Losses

To characterise how destructive the two frequency measurement is, that is how many atoms are lost from the trap due to scattering of photons, the number of atoms remaining in the trap after a measurement with a well defined number of photons is measured. The result is shown in figure 6.6. For these experiments, the number of atoms remaining in the trap after 200 light pulses with a duration of 30 μs (upper graph) and 60 μs (lower graph) each is measured as a function of the mean frequency of the frequency-synthesised light beam. Both graphs contain two sets of measurements done with light polarised parallel (empty rectangles) and perpendicular (solid

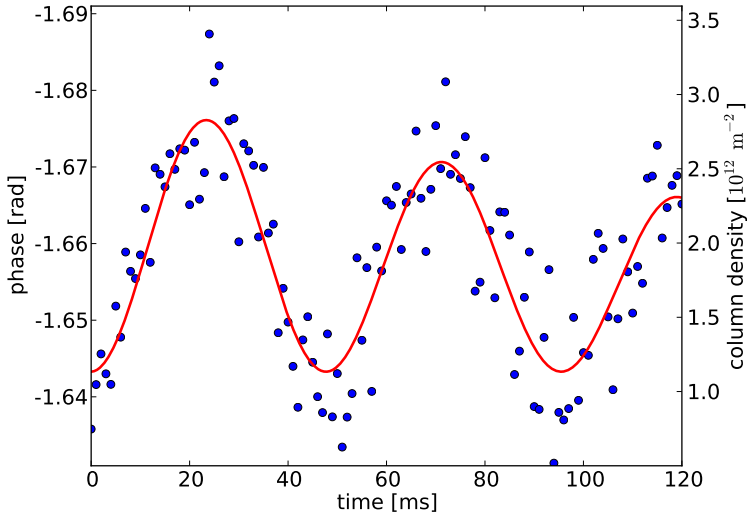


Figure 6.5: Measurement of the axial trap frequency in a single realisation of the experiment. 120 light pulses of 50 μs with 2×10^6 photons each at a repetition rate of 1 kHz are applied to the atoms. The frequency bands are separated by 60 MHz, with a central frequency detuning corresponding to +17.3 MHz in figure 6.4. The inferred density variations are due to movements of the cloud in and out of the beam. A damped sine wave of (21 ± 1) Hz and a damping coefficient of 0.26 s^{-1} fits the data.

dots) to the trap bottom magnetic field. After the pulses the total number of atoms remaining in the trap is determined by absorption imaging.

The primary loss mechanism is Zeeman-state depumping, which can be caused by as little as one spontaneous emission event. Figure 6.7 shows the relative oscillator strength of transitions from the $|F, m\rangle = |2, 2\rangle$ into the sub-levels of the $F' = 3$ excited state and the branching ratios back into the $F = 2$ ground states. Excited states other than the $|F', m'\rangle = |3, 3\rangle$ state can decay into the magnetically untrapped state $|F, m\rangle = |2, 0\rangle$, or the weakly trapped state $|F, m\rangle = |2, 1\rangle$. 90% of the atoms in the weakly trapped state are lost between pulses, since the gravitational force greatly lowers the barrier for escape as shown in figure 6.8. Heating of trapped atoms plays a very minor role here, as the recoil energy ($0.4\mu\mathrm{K} \times \mathrm{k_B}$) is about 1000 times smaller than the trap depth ($400\ \mu\mathrm{K} \times \mathrm{k_B}$).

The four data curves in the two plots in figure 6.6 show a large increase of the loss when one of the two frequencies in the probe beam hit the atomic resonance. Light with parallel polarisation addresses the π transition into the $|F', m'\rangle = |3, 2\rangle$. Perpendicular polarised light addresses mainly σ^+

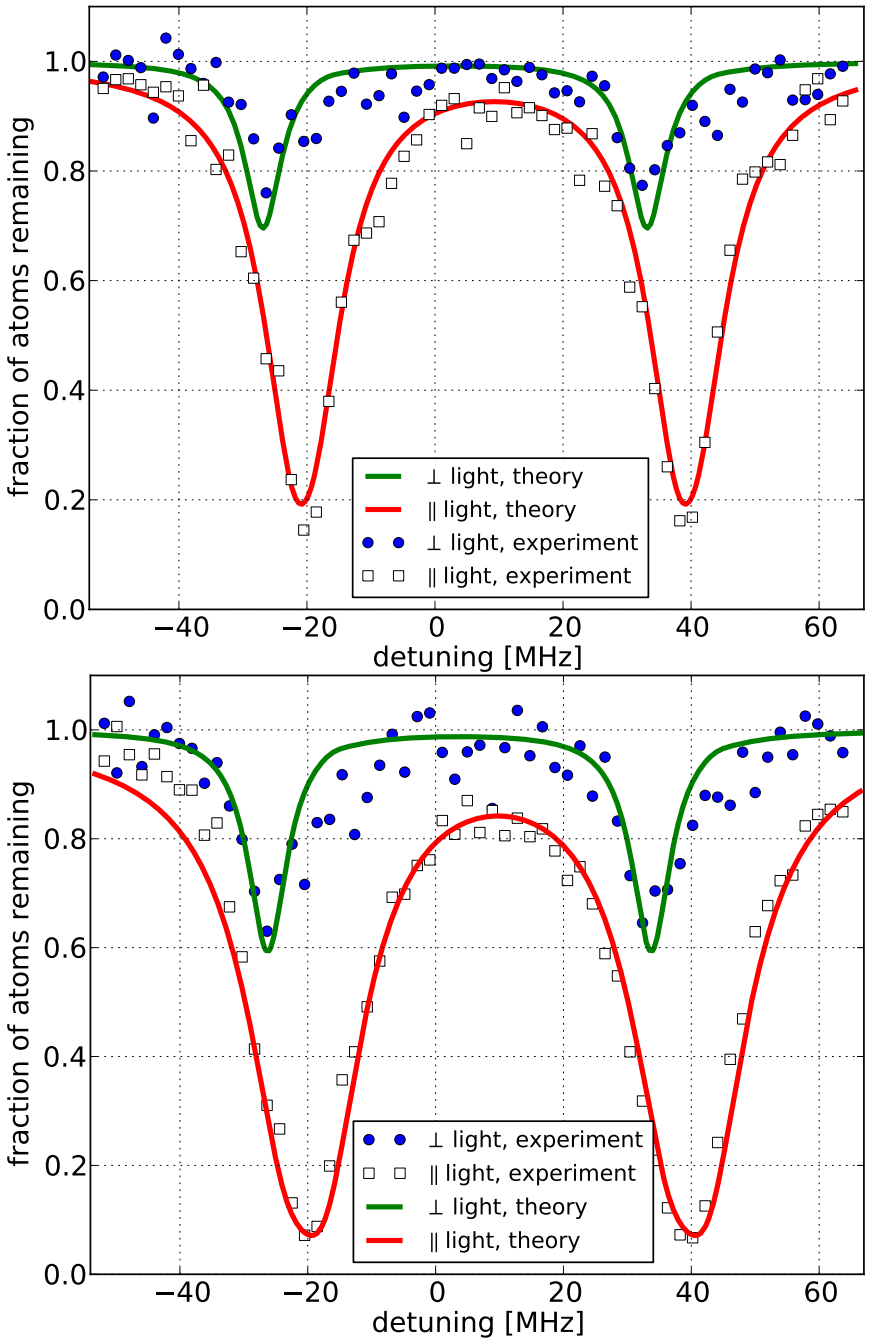


Figure 6.6: Loss of atoms from a magnetic trap due to 200 light pulses of 30 μs and 60 μs, containing 3×10^5 and 6×10^5 photons each, respectively. The loss is due to depumping of the atoms into an untrapped or weakly-trapped state. Since depumping is about 7 times less likely for atoms exposed to perpendicular light than for those interacting with parallel light, the loss also decreases by the same factor. The solid lines are theoretical predictions from a rate equation model.

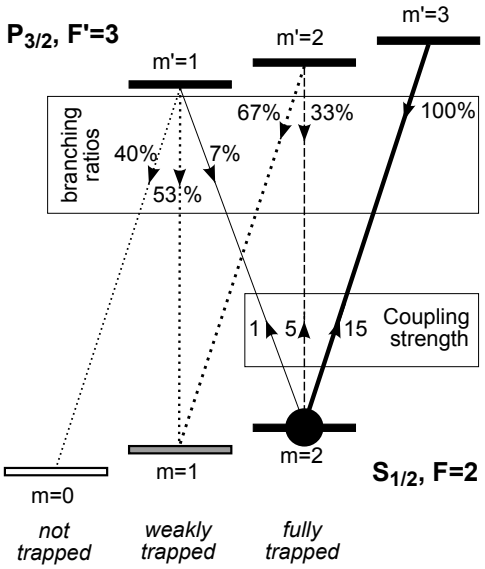


Figure 6.7: Relative coupling strengths for excitations from the trapped $|F, m\rangle = |2, 2\rangle$ state. Transitions driven by light perpendicular (parallel) to the magnetic field are indicated by a solid (dashed) line. The branching ratios from the excited states back to the different ground states are also shown. An atom undergoing a transition to the weakly and untrapped states (dotted lines) are considered to be lost.

transition. The loss, however, is maximised when the light is in resonance with the σ^- transition into the $|F', m'\rangle = |3, 1\rangle$, where the atom has a large probability of leaving the trapped state as shown in figure 6.7.

The curves shown in figure 6.6 are a plot of a simple model, which neglects effects of heating and assume that atoms in the $|F, m\rangle = |2, 1\rangle$ state are lost from the trap. We performed a simulation with a full rate-equation model tracking the internal-state population of the atoms, but deviations between the simple model and the full rate-equation are smaller than the Poissonian fluctuations of the measured atom number. We will therefore only present an approximate model.

In this model the probability Ω per scattered photon of losing an atom can be calculated using the numbers shown in figure 6.7: The probability that a scattered photon excites the atom into an excited state m' is multiplied by the branching ratios for spontaneous emission from that state into ground states other than $|F, m\rangle = |2, 2\rangle$. The fractional absorption of light per atom, i.e. the probability of a photon being scattered, is $\tilde{\tau} = \tau(f_1, f_2)/(N_c A)$, where A is the beam area. The probability of losing an atom per incident photon is therefore $\Omega \times \tilde{\tau}$ and is about 7 times higher

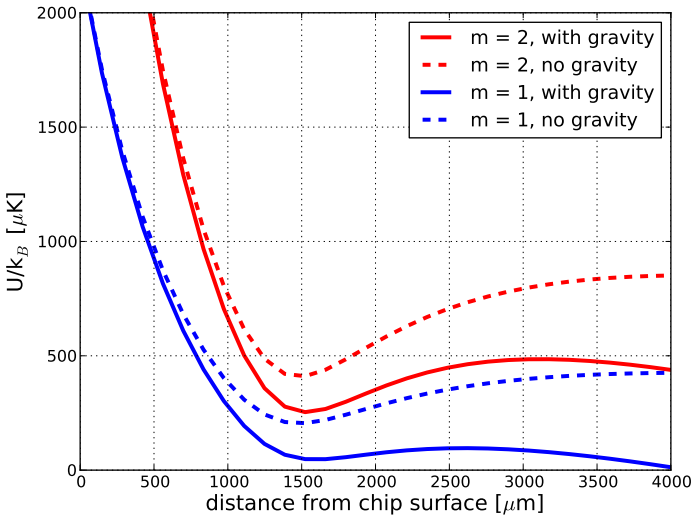


Figure 6.8: Trapping potentials for the trapped $|2,2\rangle$ and weakly trapped $|2,1\rangle$ ground states. The dashed line show the magnetic trap potential only, the solid curves the comprised magnetic potential and the gravitational forces which lower the barrier for escape by such an amount that almost all of the atoms in $|2,1\rangle$ leave the trap between measurement pulses.

for light polarised perpendicular to the trap field than for light polarised parallel to it.

The fraction g of atoms interacting with the light beam can be calculated from the mode overlap of light beam and atoms in the magnetic trap with a density distribution $N_D(x,y,z)$. Since the beam is much smaller than the atomic cloud, we can take a radial Gaussian profile $I(r) = I(r,0)$ and assume constant intensity in the axial direction over the extent of the trap. With the column density

$$N_c = \int_{-\infty}^{\infty} dx\, N_D(x,y,z), \tag{6.14}$$

where the light propagates along x, the fraction of atoms interacting with the light beam can be written as

$$g = \frac{\int_{-\infty}^{\infty} N_c(y,z) I(\sqrt{y^2+z^2}) dydz}{2\pi \int_{-\infty}^{\infty} N_c(y,z) dydz \int_0^{\infty} I(r) r dr} \tag{6.15}$$

After one pulse with N_γ photons, atoms in the interaction region have an exponential survival probability of $\exp(-\Omega\tilde{\tau}N_\gamma)$. From the initial N_0 atoms in the trap, $gN_0(1-\exp(-\Omega\tilde{\tau}N_\gamma))$ are lost during the light pulse. This factor is applied for each pulse as the density distribution recovers between pulses. This assumption is valid since due to the oscillation of atoms in the trapping potential the sample of atoms in the probed volume is renewed within less than 1 ms.

The number of atoms N_k remaining in the trap after k pulses containing N_γ photons each is:

$$N_k = N_0\left[1 - g\left(1 - e^{-\Omega\rho_l N_\gamma}\right)\right]^k. \tag{6.16}$$

The density of the cloud and the magnetic field strength are taken from the fit to the spectral data shown in figure 6.4. The focus of the beam is not at the atoms, but the beam waist at the position of the atoms is $w_0 = 100\,\mu$m. The only adjustable parameter in the fit is the initial atom number N_0. Deviations between model and experiment are due to the geometry of the magnetic field: when moving away from the trap centre, the direction of the magnetic field rotates with respect to the propagation direction of light. Therefore, π transitions are addressed in all atoms except those at the trap centre, which make up for the difference between theory and experiment in figure 6.6.

6.5 Figure of merit

The detection scheme presented above was developed to allow multiple measurements of the atomic density on the same sample, as demonstrated in figure 6.5. As a measure of the "non-destructiveness" of the measurement let us consider the accuracy that can be achieved in measuring the atom density before a given fraction of atoms is lost. It is already obvious that in terms of polarisation the perpendicular polarised light will always win over the parallel polarised light, since in the former case signals are larger and losses smaller.

The phase shift is proportional to the atom number $N_a = N_c A$: the uncertainties are related as $\sigma_a = \sigma_\theta/\tilde{\theta}$, where $\tilde{\theta} = \theta(f_1, f_2)/(N_c A)$ is the optical phase shift per atom. A perfect photon detector would not suffer

any electronic or excess noise and has a quantum efficiency of 1. In this ideal limit, the remaining phase uncertainty due to photon counting noise is $\sigma_\phi^2 = 2/N_\gamma$, which gives for the uncertainty of the atom number

$$\sigma_a = \frac{1}{\tilde{\theta}}\sqrt{\frac{2}{N_\gamma}}. \tag{6.17}$$

Increasing the photon number will decrease the uncertainty but has to be traded off against atom loss. In the limit of a small optical density, which can always be reached by a suitably large detuning, the fraction ρ of atoms lost in a single measurement can be written as

$$\rho = N_\gamma \Omega \tilde{\tau}. \tag{6.18}$$

Combining these two, a figure of merit (FoM) η can be defined, which is independent of the number of atoms and independent of the photon number N_γ. Our FoM is the inverse of the product of the inferred atom number uncertainty and the square root of the fractional atom loss:

$$\eta^2 = \frac{1}{\rho \sigma_a^2} = \frac{\tilde{\theta}^2}{2\Omega\tilde{\tau}} \propto \frac{\lambda^2}{A}. \tag{6.19}$$

The FoM can be interpreted as the signal-to-noise ratio per atom, when the atoms have a $1/e$ probability of surviving the measurement. Note that $\tilde{\theta}$ and $\tilde{\tau}$ are both inversely proportional to the beam area. The FoM therefore scales with the ratio of the scattering cross section, which is proportional to the square of the wavelength λ, to the beam area A. A large FoM therefore requires beams of the size of the wavelength. Our photonic waveguide chip provides such beams.

A plot of the FoM for an idealised detector and the experiment geometry used in this section is shown in figure 6.9. The figure also illustrates the effect of the Zeeman shifts on the FoM. In a very small magnetic field (here the field is taken to be small but sufficient to sustain the quantisation axis) the resonances for the different polarisations are essentially degenerate. The optimal FoM is found when the centre frequency f_0 is equal to the atomic resonance f_a. This corresponds to a detuning of zero in figure 6.9. The FoM approaches zero when either of the frequency components $f_0 \pm \delta f$ is close to the atomic resonance. The zero occurs when the small phase shift of the

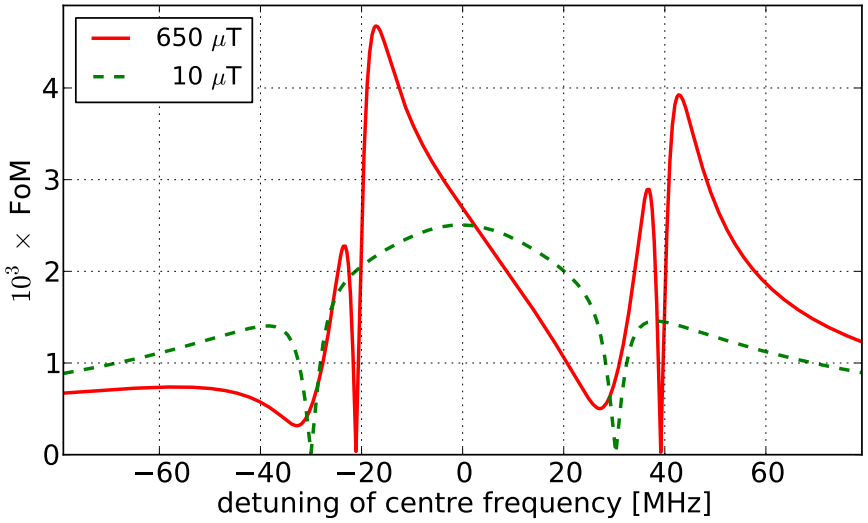


Figure 6.9: Figure of merit (FoM) for an idealised detector and light polarised perpendicular to the magnetic field. The two curves show the FoM for atoms in a magnetic trap (solid line) and in a negligible magnetic field (dashed line). When lifting the degeneracy of the magnetic sublevels the symmetry of the graph is broken. At the same time the optimum FoM is increased.

far detuned frequency component is equal to the one close to resonance.

At 650 μT (solid line in figure 6.9) the degeneracy of the magnetic sublevels is lifted. Since the σ^- transition contributes much less to the signal but much more to the loss than the σ^+ transition, the optimum frequency is shifted and the peak FoM is enhanced.

Examining the behaviour of the FoM, we optimise central detuning f_0, beat frequency $2\delta f$ and (for an experiment that suffers electronic noise) photon number N_γ as shown in figure 6.10. The graph in figure 6.10(a) is similar to the one shown in figure 6.9 and shows the figure of merit as a function of the detuning of the central frequency, keeping the beat frequency $2\delta f = 60$ MHz. The maximum of $\eta(f_0)$ versus the beat frequency $2\delta f$ is shown in 6.10(b), keeping N_γ fixed. The maximum at $2\delta f \approx 7$ MHz and the minimum at 30 MHz are due to the influence of the σ^- transition and do not exist if only a single transition is addressed. For sufficiently large splitting ($2\delta f \gtrsim 60$ MHz), the figure of merit becomes independent of the detuning, as expected. We work at $2\delta f = 60$ MHz, as it is hard to reject unwanted AOM-diffracted beams at $2\delta f = 7$ MHz.

For a real detector, i.e. one that suffers from electronic and mechanical noise, the figure of merit as introduced in equation 6.19 is not independent

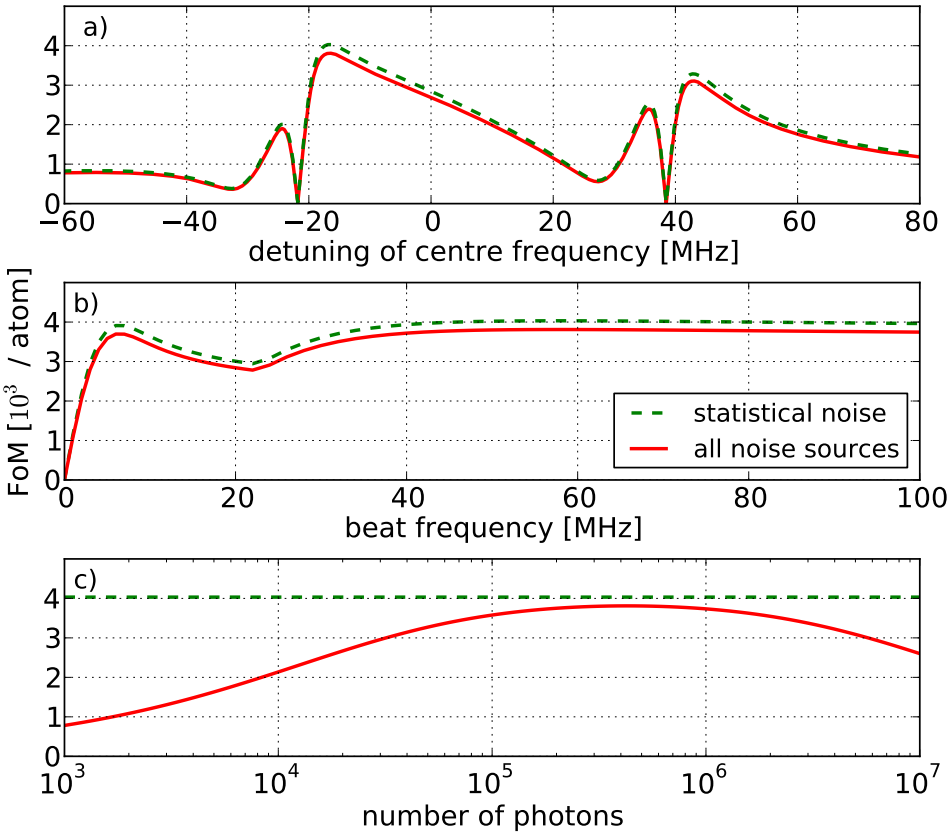


Figure 6.10: Optimising the figure of merit η in terms of central detuning f_0, beat frequency $2\delta f$, and number of photons N_γ. The average magnetic field is set to 0.65 mT, as in figure 6.4. The figure of merit (FoM) is calculated using the phase noise presented in equation 6.5, with (solid line) and without (dashed line) mechanical/technical noise. In (a) the FoM is calculated for different values of the central frequency f_0. The optimum values is found at $f_0 = +22.3$ MHz. (b) shows the maximum of $\eta(f_0)$ for different values of $2\delta f$. The best value for operation is $2\delta f \gtrsim 60$ MHz. (c) shows the FoM versus the number of photons used in a probe pulse. Here, the maximum is at $N_\gamma = 35000$. In all graphs the values that are not scanned are fixed at their optimum values for operation.

of the photon number. One requires enough photons to operate above the technical noise floor. At large photon numbers, the measurement precision is limited by the mechanical phase noise, whereas the atom loss keeps scaling linearly with the photon number. Figure 6.10(c) shows $\eta(N_\gamma)$ for a measurement with an integrated pulse time of 10 μs, keeping f_0 and δf fixed at their optimal and operational value, respectively. In this case, $\eta(N_\gamma)$ is maximised at about $350,000$ photons. The figure of merit is also plotted for a detector with shot-noise as its only noise, showing that with the right choice of parameters we can perform measurements well within 3 dB of the shot noise limit.

The FoM can also be used to explore the performance of the detection technique in different experimental circumstances, e.g. density measurements in a Bose-Einstein condensate (BEC). Here, a single scattered photon excites an atom out of the ground state and therefore out of the condensate ($\Omega = 1$). Now not only excitations on the σ^- transition lead to loss, but equally excitations on the σ^+ transition. Since both transitions contribute equally to loss and signal, the symmetry of the FoM is regained The maximum figure of merit is reduced by a factor of 16, since the latter transition is 15 times stronger than the former.

In the next round of experiments, we plan to bring together the two components of this thesis. The idea is to probe ultracold atoms trapped in the trench of the photonic waveguide chip using the double-frequency method discussed in this chapter. The mode size of the light beams in the waveguide chip, roughly $2\,\mu$m, is 50 times smaller than the $100\,\mu$m beam used in this chapter. Consequently the FoM is enhanced by a factor 50 and the maximum FoM is about 0.03.

To demonstrate the meaning of this FoM in typical experimental conditions, we take a ^{87}Rb condensate of 3×10^4 atoms in a prolate trap of trapping frequencies 20 Hz and 1 kHz inside the trench. A waveguide mode centred on the atom cloud illuminates 10^3 atoms. If we want to measure the number of atoms in the beam with an accuracy of 10%, the value of the FoM of 0.03 tells us that we have to lose as little as 100 atoms from the condensate.

7 Temporal correlation functions

In this chapter, I start developing a theoretical model for understanding what we expect to see when we measure the column density of an atomic sample at two times t and t'. The natural framework for this discussion is the quantum field theory of correlations. I will calculate the temporal correlation function for a non-interacting Bose gas at thermal equilibrium and relate it to the fluctuations of the column density measured in the experiment.

Experimentally, quantum correlations were first observed on photons by Hanbury Brown and Twiss [81]. Spatial correlations in cold atoms were detected by Yasuda and Shimizu [82] and in the groups of C. Westbrook [83, 84] and I. Bouchoule [85, 86].

With the frequency-synthesis technique described in chapter 6 we can probe the same sample of atoms several times with only small disturbances of the atom cloud. Using a waveguide chip for these experiments enables us to measure the column density of the cloud very locally, thus reducing effects of integration over the probe volume as described below. Furthermore, small beams minimise the uncertainty in the measured column density per scattered photon as described in chapter 1.

The theory for understanding the spatial correlations in an ultracold quantum gas was laid out by R. Glauber and M. Naraschewski [87]. This chapter follows reference [87] in describing the correlations, but retains the time dependence in the theory. The correlation function for an ideal Bose gas is calculated, neglecting any effects of interaction between particles or condensation of parts of the cloud. Since we measure the cloud using a probe beam with a finite area, I will calculate how the beam size affects the measured correlations. Finally, I will give an outlook on the next steps necessary to adapt my calculations to approximate the experimental conditions more accurately.

7.1 Correlation functions

In this section we calculate the first and second order correlation functions of the quantum field of cold atoms. In quantum field theory, atoms are created and annihilated by the quantum field operators $\hat{\Psi}^\dagger(\mathbf{r},t)$ and $\hat{\Psi}(\mathbf{r},t)$, respectively, with the coordinate vector $\mathbf{r}$ and time t. For bosonic ^{87}Rb atoms the field operators obey the bosonic commutation rules:

$$\begin{aligned}\left[\hat{\Psi}(\mathbf{r},t),\hat{\Psi}^\dagger(\mathbf{r}',t')\right] &= \delta(\mathbf{r}-\mathbf{r}')\delta(t-t')\\ \left[\hat{\Psi}(\mathbf{r},t),\hat{\Psi}(\mathbf{r}',t')\right] &= 0.\end{aligned} \tag{7.1}$$

For fermions these become:

$$\begin{aligned}\left\{\hat{\Psi}(\mathbf{r},t),\hat{\Psi}^\dagger(\mathbf{r}',t')\right\} &= \delta(\mathbf{r}-\mathbf{r}')\delta(t-t')\\ \left\{\hat{\Psi}(\mathbf{r},t),\hat{\Psi}(\mathbf{r}',t')\right\} &= 0,\end{aligned} \tag{7.2}$$

were $[\cdot,\cdot]$ denotes the commutator and $\{\cdot,\cdot\}$ the anticommutator. In an experiment, we measure atomic densities, integrated over the volume of the probe beam. The atomic density can be written in terms of the quantum field as

$$n(\mathbf{r},t) = \left\langle \Psi^\dagger(\mathbf{r},t)\Psi(\mathbf{r},t)\right\rangle. \tag{7.3}$$

The correlations we are interested in are the correlations in the density fluctuations which are

$$\begin{aligned}&\left\langle [\langle n(\mathbf{r},t)\rangle - n(\mathbf{r},t)]\left[\left\langle n(\mathbf{r}',t')\right\rangle - n(\mathbf{r}',t')\right]\right\rangle\\ &= \left\langle n(\mathbf{r},t)n(\mathbf{r}',t')\right\rangle - \langle n(\mathbf{r},t)\rangle\left\langle n(\mathbf{r}',t')\right\rangle\end{aligned} \tag{7.4}$$

and these correlations can therefore be expressed in terms of the quantum field as:

$$\begin{aligned}&\left\langle n(\mathbf{r},t)n(\mathbf{r}',t')\right\rangle - \langle n(\mathbf{r},t)\rangle\left\langle n(\mathbf{r}',t')\right\rangle =\\ &\left\langle \hat{\Psi}(\mathbf{r},t)^\dagger\hat{\Psi}(\mathbf{r},t)\hat{\Psi}^\dagger(\mathbf{r}',t')\hat{\Psi}(\mathbf{r}',t')\right\rangle - \left\langle \hat{\Psi}^\dagger(\mathbf{r},t)\hat{\Psi}(\mathbf{r},t)\right\rangle\left\langle \hat{\Psi}^\dagger(\mathbf{r}',t')\hat{\Psi}(\mathbf{r}',t')\right\rangle\end{aligned} \tag{7.5}$$

The first- and second-order correlation functions of the quantum field are defined as

$$G^{(1)}(\mathbf{r},\mathbf{r}',t,t') = \left\langle \hat{\Psi}^\dagger(\mathbf{r},t)\hat{\Psi}(\mathbf{r}',t') \right\rangle \tag{7.6}$$

$$G^{(2)}(\mathbf{r},\mathbf{r}',t,t') = \left\langle \hat{\Psi}^\dagger(\mathbf{r},t)\hat{\Psi}^\dagger(\mathbf{r}',t')\Psi(\mathbf{r}',t')\Psi(\mathbf{r},t) \right\rangle . \tag{7.7}$$

Using the commutation rules we can write the density correlations in terms of the field correlations as:

$$\begin{aligned}&\left\langle n(\mathbf{r},t)n(\mathbf{r}',t') \right\rangle - \left\langle n(\mathbf{r},t) \right\rangle \left\langle n(\mathbf{r}',t') \right\rangle = \\ &G^{(2)}(\mathbf{r},\mathbf{r}',t,t') + \delta(\mathbf{r},\mathbf{r}')\delta(t,t')G^{(1)}(\mathbf{r},\mathbf{r}',t,t') - G^{(1)}(\mathbf{r}',\mathbf{r}',t',t')G^{(1)}(\mathbf{r},\mathbf{r},t,t)\end{aligned} \tag{7.8}$$

In the case of a non-interacting gas, reference [87] shows that we can write $G^{(2)}$ in terms of $G^{(1)}$:

$$G^{(2)}(\mathbf{r},\mathbf{r}',t,t') = G^{(1)}(\mathbf{r},\mathbf{r},t,t)G^{(1)}(\mathbf{r}',\mathbf{r}',t',t') \pm \mid G^{(1)}(\mathbf{r},\mathbf{r}',t,t') \mid^2 \tag{7.9}$$

where the plus (minus) sign applies to bosons (fermions). Therefore:

$$\begin{aligned}&\left\langle n(\mathbf{r},t)n(\mathbf{r}',t') \right\rangle - \left\langle n(\mathbf{r},t) \right\rangle \left\langle n(\mathbf{r}',t') \right\rangle = \\ &\qquad \delta(\mathbf{r},\mathbf{r}')\delta(t,t')G^{(1)}(\mathbf{r},\mathbf{r}',t,t') \pm \mid G^{(1)}(\mathbf{r},\mathbf{r}',t,t') \mid^2\end{aligned} \tag{7.10}$$

Hence, to calculate the density correlations in an ideal gas we only need to know $G^{(1)}(\mathbf{r},\mathbf{r}',t,t')$. The first term on the right of equation 7.10 is the uncorrelated poissonian part of the fluctuations, while the second represents the quantum enhancement (suppression) for bosons (fermions).

7.2 Correlations in an ideal Bose gas

In this section we calculate the first order correlation function for a non-interacting gas of bosons in a harmonic potential. Here, the three-dimensional correlation function is just the product of the one-dimensional correlation functions. We therefore start by calculating the correlation function along x, where the confining potential has a harmonic frequency of Ω_x. We can write the correlation function in the basis of the one-particle energy eigenstates

$u_m(r,t)$ with energies

$$\epsilon_m = \hbar\Omega_x \left(m + \frac{1}{2}\right), \tag{7.11}$$

where m is the quantum number of the oscillator state. We can separate the spatial and the temporal parts of the eigenfunctions $u_m(x,t) = v_m(x)\exp\left(-\mathrm{i}\epsilon_m t/\hbar\right)$. The correlation function of an ideal Bose gas at thermal equilibrium in the grand canonical ensemble is a function of the two positions x and x' and the time difference $\tau = t' - t$. It is given as [87]

$$G_x^{(1)}(x,x',\tau) = \sum_m v_m^*(x)v_m(x')e^{-\mathrm{i}\tilde{\epsilon}_m\tau/\hbar}\frac{Z_x e^{-\beta\tilde{\epsilon}_m}}{1 - Z_x e^{-\beta\tilde{\epsilon}_m}} \tag{7.12}$$

with the inverse temperature $\beta = 1/k_B T$, the fugacity $Z_x = e^{\beta\mu_x}$ and the chemical potential μ_x. The eigenenergies of the potential $\tilde{\epsilon}_m = \epsilon_m - 1/2\hbar\Omega_x$ are taken without the ground state energy in order to limit the fugacity to values between 0 and 1 as required for an ideal gas [87]. The Bose-Einstein factor (the last factor in equation 7.12) can be expanded as a power series in the fugacity Z_x

$$\begin{aligned} G_x^{(1)}(x,x',\tau) &= \sum_m v_m^*(x)v_m(x')e^{-\mathrm{i}\tilde{\epsilon}_m\tau/\hbar}\sum_{k=1}^{\infty} Z_x^k e^{-k\beta\tilde{\epsilon}_m} \\ &= e^{1/2\Omega_x(k\beta\hbar+\mathrm{i}\tau)}\sum_{k=1}^{\infty} Z_x^k \sum_m v_m^*(x)v_m(x')e^{-\mathrm{i}\epsilon_m(\tau-\mathrm{i}k\hbar\beta)/\hbar} \end{aligned} \tag{7.13}$$

The sum over m can be written in terms of the propagator $P(x,x',t)$, which is defined as

$$\begin{aligned} P_x(x,x',t) &= \left\langle x' \mid e^{-\mathrm{i}Ht/\hbar} \mid x \right\rangle \\ &= \sum_m v_m^*(x)v_m(x')e^{-\mathrm{i}\epsilon_m t/\hbar}, \end{aligned} \tag{7.14}$$

where H is the single-particle Schrödinger Hamiltonian. Thus, P is also the Green's function for the time-dependent wave equation

$$\left[-\frac{\hbar^2}{2M}\nabla^2 + V(x') - i\hbar\frac{\partial}{\partial t}\right] P(x',x,t) = -i\hbar\delta\left(x'-x\right)\delta\left(t\right) \tag{7.15}$$

with the harmonic oscillator potential $V(x) = M\Omega_x^2 x^2/2$, where M is the mass of the particle. The propagator can be written as [88]

$$P_x(x, x', t) = \sqrt{\frac{M\Omega_x}{2\pi \mathrm{i}\hbar \sin(\Omega_x t)}} \times \exp\left[\frac{\mathrm{i}M\Omega_x}{2\hbar \sin(\Omega_x t)}\left(\left(x^2 + x'^2\right)\cos(\Omega_x t) - 2xx'\right)\right]. \quad (7.16)$$

Using the propagator at time $t = \tau - \mathrm{i}k\tau_c$ with $\tau_c = \hbar\beta$ we can replace the sum in equation 7.13 with the propagator

$$G_x^{(1)}(x, x', \tau) = \sum_{k=1}^{\infty} Z_x^k e^{\frac{1}{2}\Omega(k\tau_c + \mathrm{i}\tau)} P_x(x, x', \tau - \mathrm{i}k\tau_c). \quad (7.17)$$

If the spacing of the energy levels $\hbar\Omega_x$ of the trap is much smaller than the thermal energy $k_B T$ of the particles, the propagator can be simplified substantially. In that case, the term $k = 1$ of the sum is the dominant term and the time argument $\Omega|\tau - \mathrm{i}\tau_c| \ll 1$. This makes the correlation function

$$G_x^{(1)}(x, x', \tau) = Z e^{\frac{1}{2}\Omega_x(\tau_c + \mathrm{i}\tau)} \left(\frac{M}{2\pi i\hbar(\tau - \mathrm{i}\tau_c)}\right)^{1/2} \times \exp\left\{\frac{\mathrm{i}M}{2\hbar(\tau - \mathrm{i}\tau_c)}\left[(x' - x)^2 - \frac{(\tau - i\tau_c)^2}{2}\left(x'^2 + x^2\right)\Omega_x^2\right]\right\}. \quad (7.18)$$

The correlation function is easily generalised to include all three dimensions of the harmonic trap. The propagator is the product of the propagators in each dimension:

$$P(\mathbf{r}, \mathbf{r}', t) = P_x(x, x', t) P_y(y, y', t) P_z(z, z', t). \quad (7.19)$$

and equation 7.17 becomes [1]

$$\tilde{G}^{(1)}(x, x', \tau) = \sum_{k=1}^{\infty} \prod_{s \in \{x,y,z\}} Z_s^k e^{\frac{1}{2}\Omega_s(k\tau_c + \mathrm{i}\tau)} P_s(s, s', \tau - \mathrm{i}k\tau_c). \quad (7.20)$$

[1] The tilde distinguishes the $G^{(1)}$ with three arguments from the one with four arguments used in section 7.1.

In the approximation of equation 7.18 this becomes

$$\tilde{G}^{(1)}(\mathbf{r},\mathbf{r}',\tau) = Z e^{\frac{3}{2}\bar{\Omega}(\tau_c+\mathrm{i}\tau)} \left(\frac{M}{2\pi i\hbar(\tau-\mathrm{i}\tau_c)}\right)^{3/2} \times \exp\left\{\frac{\mathrm{i}M}{2\hbar(\tau-\mathrm{i}\tau_c)}\left[(\mathbf{r}'-\mathbf{r})^2 - \frac{(\tau-i\tau_c)^2}{2}\sum_{s\in\{x,y,z\}}\left(s'^2+s^2\right)\Omega_s^2\right]\right\}, \tag{7.21}$$

where $\bar{\Omega} = (\Omega_x + \Omega_y + \Omega_z)/3$ is the arithmetic mean of the three oscillation frequencies.

The fugacity $Z = Z_x Z_y Z_z$ is determined by the normalisation condition

$$N_a^{tot} = \int d^3\mathbf{r}\, \tilde{G}^{(1)}(\mathbf{r},\mathbf{r},0), \tag{7.22}$$

where N_a^{tot} is the total number of atoms in the cloud. Using equation 7.21 we express Z as:

$$Z = \tau_c^3 e^{-3/2\bar{\Omega}\tau_c}\Omega_x\Omega_y\Omega_z\, N_a^{tot}. \tag{7.23}$$

7.3 Gaussian probe beam

In our experiments we cannot measure the density at a single point $\mathbf{r}$, but only the average column density N_c, that is the density integrated along the propagation direction of the probing laser beam and averaged over the beam profile. From that we can infer the number of atoms N_a that interact with the probe beam

$$N_a(t) = \int n(\mathbf{r},t) I(\mathbf{r})\, d^3\mathbf{r}, \tag{7.24}$$

where $I(\mathbf{r})$ is the intensity profile of the probe beam, normalised by the peak intensity I_0.

In a single experiment, the number of atoms N_a in the beam is measured at two times t and $t' = t + \tau$ to find the product $N_a(t)N_a(t')$. This experiment is repeated several times to create a set of products. The correlations

of the fluctuations of the measured atom number can be expressed as

$$\begin{aligned} C(t,t') &= \left\langle N_a(t)N_a(t')\right\rangle - \left\langle N_a(t)\right\rangle \left\langle N_a(t')\right\rangle \\ &= \left\langle \int n(\mathbf{r},t)I(\mathbf{r})\,d^3\mathbf{r} \int n(\mathbf{r}',t')I(\mathbf{r}')\,d^3\mathbf{r}' \right\rangle - \\ &\quad \left\langle \int n(\mathbf{r},t)I(\mathbf{r})\,d^3\mathbf{r} \right\rangle \left\langle \int n(\mathbf{r}',t')I(\mathbf{r}')d^3\,\mathbf{r}' \right\rangle \\ &= \int d^3\mathbf{r}\, I(\mathbf{r}) \int d^3\mathbf{r}'\, I(\mathbf{r}')\times \\ &\quad \left(\left\langle n(\mathbf{r},t), n(\mathbf{r}',t')\right\rangle - \left\langle n(\mathbf{r},t)\right\rangle \left\langle n(\mathbf{r}',t')\right\rangle\right). \end{aligned} \tag{7.25}$$

Here, angle brackets indicate average over the set of measurements. Using equation 7.10 this becomes

$$\begin{aligned} C(t,t') = \int d^3\mathbf{r}\, I(\mathbf{r}) \int d^3\mathbf{r}'\, I(\mathbf{r}')\times \\ \Big[\underbrace{\delta(t,t')\delta(\mathbf{r},\mathbf{r}')\tilde{G}^{(1)}(\mathbf{r},\mathbf{r}',t'-t)}_{\text{poissonian fluctuations}} + \underbrace{|\,\tilde{G}^{(1)}(\mathbf{r},\mathbf{r}',t'-t)\,|^2}_{\text{bosonic enhancement}}\Big]. \end{aligned} \tag{7.26}$$

The first term gives the poissonian counting fluctuations, proportional to the number of atoms in the beam. The second term, due to the bunching of the bosons, produces an increase of the correlations at small τ.

The three-dimensional integral of equation 7.26 can be decomposed into three one-dimensional integrals. We consider a Gaussian probe beam with a waist w_B. The intensity of the beam along its propagation axis x is constant over the extend of the atomic cloud. The three components of the intensity profile of the beam are then

$$I_x(x) = 1 \tag{7.27}$$

$$I_y(y) = e^{-2\frac{y^2}{w_B^2}} \tag{7.28}$$

$$I_z(z) = e^{-2\frac{z^2}{w_B^2}}, \tag{7.29}$$

which have been normlised to the peak intensity of the beam.

The centre of the trap defines the origin of our coordinate system. Let the centre of the light beam be at position $\mathbf{R}_0 = (x_0, y_0, z_0)^T$. Using equation

7.21, equation 7.26 now becomes

$$\begin{aligned}\tilde{C}(\tau,\mathbf{R}_0) = &\prod_{s\in\{x,y,z\}} \int dq\, I_s(q-s_0) G_s^{(1)}(q,q,0) \\ &+ \prod_{s\in\{x,y,z\}} \int dq \int dp\, I_s(q-s_0) I_s(p-s_0) \left| G_s^{(1)}(q,p,\tau)\right|^2 \\ \equiv &\delta(\tau)\tilde{C}_1(\mathbf{R}_0) + \tilde{C}_2(\tau,\mathbf{R}_0),\end{aligned} \tag{7.30}$$

where $G_s^{(1)}$ is given by equation 7.18.

7.4 Numerical values

Figure 7.1 shows a plot of the correlations we expect in a typical experiment. We take $N_a = 2\times 10^4$ atoms in a harmonic trap with trapping frequencies $\Omega_x = \Omega_y = 2\pi\times 800\,\mathrm{Hz}$ and $\Omega_z = 2\pi\times 20\,\mathrm{Hz}$ and a trap bottom field of $B = 1\,\mathrm{G}$, which are typical parameters for our experiment. The atoms are assumed to have a temperature of $T = 0.5\,\mu\mathrm{K}$. The $1/e$ radius of the cloud is [89]

$$w_i = \sqrt{k_B T/(M\Omega_i^2)}, \tag{7.31}$$

which for our cloud is $1.4\times 1.4\times 55\,\mu\mathrm{m}^3$. This size is chosen to (roughly) match the cloud size to the radius of the waveguide mode $w_B = 2.16\,\mu\mathrm{m}$ while still maintaining a large density. The cloud in this example has a thermal deBroglie wavelength of [89]

$$\lambda_{dB} = \sqrt{\frac{2\pi\hbar^2}{Mk_BT}} = 0.26\,\mu\mathrm{m}, \tag{7.32}$$

which corresponds to a phase space density of

$$\rho_{PSD} = \frac{N_a\lambda_{dB}^3}{(2\pi)^{3/2} w_x w_y w_z} \approx 0.6, \tag{7.33}$$

just below the critical density for Bose-Einstein condensation. The centre of the light beam is at the centre of the cloud ($\mathbf{R}_0 = 0$).

Figure 7.1 shows the function $\tilde{C}(\tau,0)$ in equation 7.30, as calculated by numerical integration. The two curves are plotted as a function of delay time τ in units of $\tau_c = \hbar/(k_BT) = 15\,\mu\mathrm{s}$. These graphs show the correlation

function calculated with the simple propagator (equation 7.21, red, solid line) and with the full propagator (equation 7.20, dashed, blue line). For small times, these two are identical, but to get the temporal evolution at larger τ right, the full propagator needs to be used. We see that $\tilde{C}(\tau, 0)$ drops from an initial value of 6.8 down to 1 over a time delay of order 1.5 ms. The time scale for the decay is set by the time it takes a particle to cross the beam $t = w_B\sqrt{M/(k_B T)}$. In the next section, we consider the possibility of measuring this $\tilde{C}_2(\tau, 0)$.

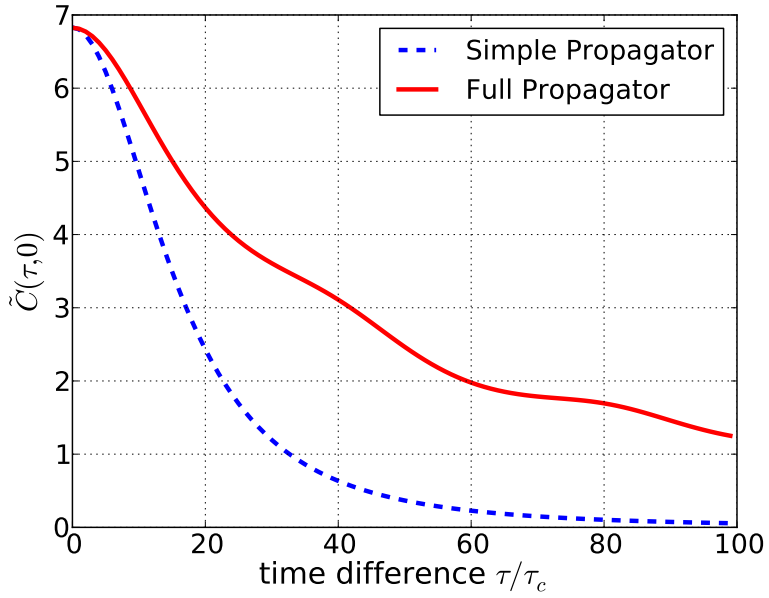


Figure 7.1: Bosonic enhancement of the correlations of the atom number fluctuations ($\tilde{C}_2(\tau, 0)$ from equations 7.30) for a set of parameters typical for our experiments (see text). Dashed line: correlations calculated with simple propagator (equation 7.21), solid line: calculated with full propagator (equation 7.20).

7.5 Possible measurements

The quantity inferred from the experimental data is the correlation of the atom number fluctuations as written in equation 7.25. If we assume a gaussian distribution of $n_i(t)$ and $n_i(t')$ and neglect the small correlations, the uncertainty on the correlation as expressed in equation 7.4 can be calculated

using gaussian error propagation [90]:

$$\sigma_{\tilde{C}} \simeq \frac{\sigma_t \sigma_t'}{\sqrt{N-1}}, \tag{7.34}$$

where N is the number of pairwise measurements and σ_t ($\sigma_{t'}$) is the width of the distribution of $n_i(t)$ ($n_i(t')$). The approximation holds as long as N is large enough so that the gaussian distribution is a good approximation to the poissionian number distribution and the correlation coefficient

$$\frac{\tilde{C}}{\sigma_t \sigma_{t'}} \ll 1 \tag{7.35}$$

is small.

To detect correlations at time τ with a signal-to-noise ratio (SNR) of 1, we need to fulfil:

$$\sigma_{\tilde{C}} < \tilde{C}(\tau, 0). \tag{7.36}$$

This equation sets a lower limit on the number of measurements required to detect the correlations.

In an experiment with a perfect detector, σ_t is set by the poissonian fluctuations of the atom number, $\sigma_t = \sigma_n = \sqrt{N_a^b}$, where $N_a^b = \tilde{C}_1(0)$ is the number of atoms in the beam. In the numerical example presented above, it would require 1260 pairwise measurements to resolve a correlation of $\tilde{C}_2 = 6.8$ with a SNR of 1. If we could measure 100 data pairs in an experimental run before we need to replenish the cloud, and each experimental run takes about 15 s, it would require less than 4 minutes to acquire the necessary data. The number of measurements scales quadratically with the SNR, so for an SNR of 4 we would have to acquire data for just under an hour.

When we use a real detection system, σ_t is the quadratic sum of σ_n and the noise due to the detection process σ_d. σ_d comprises the photon shot noise and the electronic noise from the detection electronics. The detection scheme presented in chapter 6 measures the number of atoms by measuring the phase shift between two frequency components of the probe beam. The noise on this phase due to the detection process can be expressed using equations 6.3 and 6.4:

$$\tilde{\sigma}_d^2 = \frac{2F}{N_{ph}} + \frac{s_e}{N_{ph}^2}, \tag{7.37}$$

where $F \approx 10$ is the measured excess noise factor of our avalanche photodiode and $s_e \approx 5 \times 10^4$ photons is the photon equivalent of the electronic noise in a $1\,\mu$s light pulse. These noise contributions can be made small by using a large number of photons N_{ph}.

The phase shift is proportional to the number of atoms in the beam

$$\phi(\Delta) = \frac{N_a^b}{2}\frac{\sigma_0}{A}\frac{\Delta}{1+\Delta^2}, \tag{7.38}$$

where Δ is the detuning of the laser from the frequency of the closed transition in units of the transition linewidth (HWHM), A the area of the probe beam and σ_0 the resonant atom-light scattering cross section. With this equation we can convert the phase noise to fluctuations in the inferred atom number:

$$\sigma_d = \frac{\tilde{\sigma}_d}{A}\frac{N_a^b}{\phi(\Delta_1) - \phi(\Delta_2)}. \tag{7.39}$$

In the experiments described in chapter 6, we detect the atoms using light polarised perpendicular to the magnetic field, driving σ^+ and σ^- transitions. One out of 16 scattered photons addresses a σ^- transition and the atom has a large probability of being lost from the trap due to Zeeman state depumping. We will therefore limit the number of photons scattered to 1.5 photons per atom.

Scattering 1.5 photons per atoms, with a recoil energy of $k_B \times 0.4\,\mu$K per photon, will heat the trap by $0.6\,\mu$K, which is a limit for the disturbance of the cloud as well.

Taking the parameters given above, we find 213 atoms in the beam ($\tilde{C}_1(0)$), which means we can scatter 320 photons per measurement. Since the absorption coefficient of the electric field is

$$\alpha = N_a^b\frac{\sigma_0}{A}\frac{1}{1+\Delta^2}, \tag{7.40}$$

this corresponds to 3720 incident photons. Using equation 7.37, the detection noise is estimated to correspond to an atom number uncertainty of $\sigma_d \approx 12$ roughly equal to the poissonian fluctuations of the atom number $\sigma_n = 14$. Measuring $\tilde{C}_2(0,0)$ with a SNR of 1 would require about 3500 measurements. Since we scatter 1.5 photons per atom, the premise of doing 100 measurements per experimental run seems unrealistic, but 10

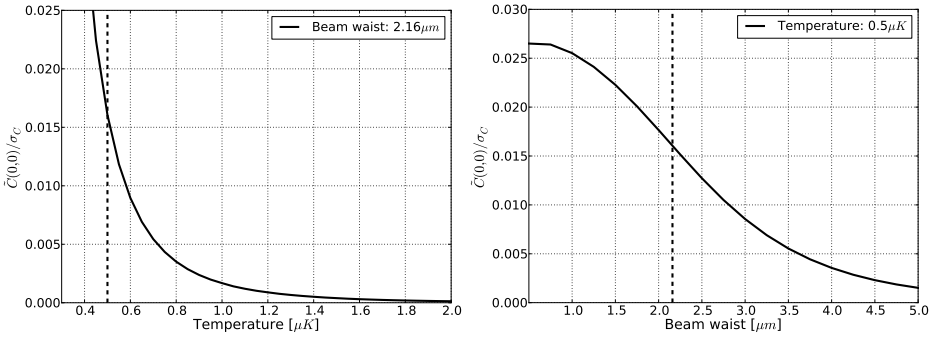


Figure 7.2: Optimising the signal-to-noise ratio ($\tilde{C}(0,0)/\sigma_C$) of the measurement by varying temperature and probe beam size. The SNR is maximised by maximising the average atomic column density in the beam either by reducing the temperature or by reducing the beam size and thus focussing the beam onto the dense parts of the cloud.

measurements may well be possible, e.g. using adjacent waveguides. The measurement would than require an hour, for a SNR of 2 we will need about 4 hours.

7.6 Summary

This chapter showed that one could measure the temporal correlations with an ideal detector. In a real experiment, it depends on the detection scheme and the noise level of the detector whether temporal correlations can be measured with a suitable signal-to-noise ratio (SNR) on time scales accessible with the stability of the experiment. With the apparatus and methods described in this thesis, detecting temporal correlations seems to be a bit hard, but still doable. There is, however, room for optimising the detection. This can for example be done by reducing the noise in the detector electronics. The ratio $\tilde{C}/\sigma_C$ can also be increased by lowering the temperature of the atoms as shown in the left graph of figure 7.2, but then the effect of a condensate needs to be taken into account (see appendix). $\tilde{C}/\sigma_C$ increases with increasing atomic column density, which may be increased by having larger atom numbers or by using higher trap frequencies and correspondingly smaller-diameter light beams. These improvements would require only modest modifications of our experimental setup. The SNR as a function of the beam size is plotted in the right graph of figure 7.2. The smaller beam focusses on the densest part of the cloud, and thereby increases the average column density. The column density can be increased even more dramat-

ically by using a beam that propagates along the long axis of the cloud. Then, measuring temporal correlation functions can easily be done even with a detector with a realistic noise level. These measurements have not been done before in this way, so they may be the basis of a PhD for a new student. It would also be interesting to extend the theory to include a BEC or finite sized particles. I have given a few starting points in the appendix. Finally, we want to understand how the interactions between atoms and light influence the dynamic evolution of the atomic cloud and thereby the correlation function.

8 Conclusion and Outlook

This thesis described the development of novel techniques for the detection and manipulation of cold gases of neutral atoms and possible applications. The focus of this work lies on the implementation of a photonic waveguide chip into an atom optics experiment. The photonic chip we use contains twelve waveguides intercepted by a trench and has been described in chapter 2. The experimental hardware necessary for cooling and trapping neutral atoms of ^{87}Rb was detailed in chapter 4. First experiments involving atoms and chip were presented in chapter 5. These experiments were done to characterise the atom-photon interaction as described in chapter 3 on the chip. The full potential of the array of atom-photon junctions will unfold when the trench is loaded with a cloud of ultracold atoms (below $1\,\mu$K) or even a Bose-Einstein condensate. Then, the waveguide light can be used to probe small parts of the cloud to measure its dynamical evolution and quantum mechanical properties.

To reach the ultracold regime, the process of evaporation needs improving. Evaporative cooling means removing the moste energetic particles from the trap and letting the remaining particles thermalise. The new equilibrium temperature will then be lower than the initial temperature. In our present experiment, the lowest temperature we can reach with this procedure is about $5\,\mu$K, limited by the lifetime of the trap which is about 5 s. The lifetime is defined as the time after which $1/e$ of the initial particles are still in the trap, while the others have been removed mainly due to collisions with particles in the residual background gas. To reach lower temperatures, we either have to reduce the pressure in our chamber and thereby extend the trap lifetime or speed up the evaporation process. Since we have not been able to reduce the pressure (see chapter 4) we require faster evaporation through faster collision rates. This can be done by tightening the trapping potential and increasing the density of atoms. We are trying to do this by overlapping the magnetic trapping potential with the optical potential from

an 8 W laser beam at a wavelength of 1030 nm, boosting the trap frequencies from 27 Hz to about 1 kHz in the axial direction. This should increase the collision rate sufficiently to reach condensation in the lifetime set by the vacuum.

In chapter 6, I have presented a new technique for weakly-destructive measurements of the atom density, using the differential phase shift between two frequency components of a frequency-synthesised light beam. Since the beam is synthesised we can balance the two frequencies around the atomic resonance. When measuring a condensate, this will minimise the optical dipole force on the condensate, since the sum of the forces exerted by the two frequency components can be set to zero.

The experiments presented here, however, are all done with a free-space laser beam. As a next step we will use the waveguides to guide the frequency-synthesised light to and from the atoms. In chapter 7 I proposed the measurement of temporal correlations as a possible application of the combined setup. Beyond what was presented in chapter 7 we consider using the chip for active feedback on the trapping fields to either stabilise the number of particles within an experimental cycles or to damp oscillations of the trap centre, which would otherwise be transformed into heat.

Outlook

Looking further into the future we might be able to use the chip for quantum information processing [91]. Light from the waveguides can be used to produce an array of dipole trap with just a few tens of particles in each site. The spacing of the traps is close enough that the electric field produced by an excitation to a state with a large principle quantum number (Rydberg state) shared between the atoms of one site significantly changes the excitation energy to such a state in the neighbouring site (Rydberg blockade). This mechanism can be used to build a quantum gate [92, 93], with fidelities of up to 99 %, limited by the excited state life time of the Rydberg state. The only problem that obstructs the creation of such gates on our current chip is the effect of surface charges in the trench interfering with the large dipole moment of the Rydberg atoms. This can be prevented by coating the trench surfaces with a conducting material.

It is possible to incorporate more complex structures into the chip. These

include controlled beam splitter [94, 26], magneto-optical traps [95, 96] or optical cavities [97, 98]. The near future might see the realisation of single photon emitters coupled to a waveguide [99] or coupled cavity networks [100] on a chip to mention but a few proposals for future work. With the growing toolbox of on-chip functionality, these hybrid system will surely find plenty of applications for intriguing research on quantum dynamics and information processing.

9 Appendix

9.1 Calculating the figure of merit for absorption and phase measurements

For the following calculations we will assume that we can address a closed transition between atomic states and that the population of the excited state remains small. Furthermore, we take the beam size of the probe beam A to be smaller than the atomic cloud so that all photons interact with the atoms. The beam is detected with a photodiode, which converts photons into free electrons in a semi-conductor. These electrons will form a current in the diode that is proportional to the number of incoming photons and hence the incident light power. We will assume that each incident photon will produce an electron. The constant of proportionality between incident power P_0 and photodiode current I is then

$$I = \frac{e}{\hbar\omega_L} P_0. \tag{9.1}$$

The noise on this current is due to Poissonian fluctuations in the number of incident photons. These fluctuations are inherent to all counting processes with random arrival. This noise scales with the square root of the counted number and is known as shot noise. It transforms into fluctuations of the current as [101]

$$\sigma_I = \sqrt{2eBI}, \tag{9.2}$$

where B is the bandwidth of the photodiode and e the charge of the electron.

The power of a light beam passing through a cloud of atoms will be absorbed according to the Beer-Lambert law as $P' = P_0 e^{-\alpha}$, where P_0 is the initial power of the light beam. We can then write the attenuation constant α as a function of number of atoms N_a in a probe beam of area A

and frequency ω_L as

$$\alpha = \frac{N_a \sigma_0}{2A} \frac{1}{1+\Delta^2}. \tag{9.3}$$

where $\Delta = (\omega_L - \omega_0)/(\Gamma/2)$ is the detuning of the laser from the atomic resonance ω_0 and Γ is the inverse of the excited state lifetime. When detuned from the atomic resonance, the light beam will also acquire a phase shift

$$\phi = \frac{N_a \sigma_0}{2A} \frac{\Delta}{1+\Delta^2}. \tag{9.4}$$

A detailed derivation can be found in chapter 3.

9.1.1 Absorption

The light beam hitting the photodiode after passing through the atomic cloud will produce a current

$$I_s = \frac{e}{\hbar \omega_L} P_0 e^{-\alpha}. \tag{9.5}$$

For small absorption ($\alpha \ll 1$) we can write $P_0 e^{-\alpha} = P_0 (1-\alpha)$. Furthermore, we can express the incident light power in terms of the number of incident photons N_γ in a light pulse of duration T by writing $P_0 T = N_\gamma \hbar \omega_0$. If the light pulse is longer than the inverse of the photodiode bandwidth B and we integrate the signal over the duration of that pulse, the measurement bandwidth is set by the pulse length and is $B = 1/(2T)$. With that the photodiode current becomes

$$I_s = 2eBN_\gamma (1-\alpha). \tag{9.6}$$

In the experiment we will infer the number of atoms from the difference between the measured current when detecting a light beam with (I_s) and without atoms ($I_{ref} = 2eBN_\gamma$) as

$$N_a(I_{ref} - I_s) = \frac{N_a}{\alpha} \frac{I}{2eBN_\gamma} = \frac{2A}{\sigma_0} \frac{I}{2eBN_\gamma} \left(1+\Delta^2\right). \tag{9.7}$$

The measured current difference fluctuates with the quadratic sum of the fluctuations of the reference and signal current

$$\sigma_I = \sqrt{2eB\left(I_s + I_{ref}\right)} = 2eB\sqrt{N_\gamma (2-\alpha)}, \tag{9.8}$$

and the inferred atom number will therefore have an uncertainty of

$$\sigma_a = \left| \frac{\partial N_a(I)}{\partial I} \sigma_I \right| = N_a \sqrt{\frac{1}{N_\gamma}} \sqrt{\frac{2-\alpha}{\alpha^2}} \approx \frac{N_a}{\alpha} \sqrt{\frac{2}{N_\gamma}}. \tag{9.9}$$

The number of photons scattered per atoms is simply

$$\rho = \frac{N_\gamma \alpha}{N_a} \tag{9.10}$$

The figure of merit is

$$\eta^2 = \frac{1}{\rho \sigma_a^2} = \frac{\alpha}{N_a} = \frac{\sigma_0}{A} \frac{1}{1+\Delta^2}. \tag{9.11}$$

9.1.2 Interferometer

To determine the phase shift of a light beam passing through the atoms we will consider a two-path Mach-Zehnder type interferometer (figure 1.2(b)). Two detectors at the output of the interferometer will record currents I_1 and I_2. With no atoms in either of the interferometer arms the interferometer is balanced ($I_1 = I_2$). An atomic sample in one of the beams will introduce a small phase shift $\phi \ll 1$ and the detectors will record currents

$$I_1 = 2eB \left[N_\gamma - \phi N_\gamma \right] \tag{9.12}$$

$$I_2 = 2eB \left[N_\gamma + \phi N_\gamma \right]. \tag{9.13}$$

N_γ is again the number of photons passing through the atomic cloud. The difference between the two currents

$$\delta = I_2 - I_1 = 4\phi e B N_\gamma \tag{9.14}$$

is proportional to the atom number. Again, in the experimental situation we need to infer the atom number from the measured current difference

$$N_a(\delta) = \frac{\delta}{4eBN_\gamma} \frac{N_a}{\phi} = \frac{\delta}{2eBN_\gamma} \frac{A}{\sigma_0} \frac{1+\Delta^2}{\Delta}. \tag{9.15}$$

The uncertainty in the current difference is the quadratically added uncertainty in the two detector currents

$$\sigma_\delta = 2eB\sqrt{2N_\gamma} \tag{9.16}$$

which gives for the uncertainty in the detected atom number

$$\sigma_a = \left|\frac{\partial N_a(\delta)}{\partial \delta}\sigma_\delta\right| = \frac{1}{2}\frac{N_a}{\phi}\sqrt{\frac{2}{N_\gamma}}. \tag{9.17}$$

The number of photons scattered per atom is again

$$\rho = \frac{N_\gamma \alpha}{N_a}, \tag{9.18}$$

This makes the figure of merit

$$\eta^2 = \frac{1}{\rho\sigma_a^2} = 2\frac{N_a}{\alpha}\left(\frac{\phi}{N_a}\right)^2 = \frac{\sigma_0}{A}\frac{\Delta^2}{1+\Delta^2}. \tag{9.19}$$

9.2 Temporal correlations: Next steps

This section summarises a few thoughts I had which can be used to extend the calculations of the temporal correlation functions from chapter 7 to include the effect of particle interactions and condensation. As such, they are more a starting point for a future student who wishes to get involved rather than a complete treatment of the problems.

9.2.1 Interacting thermal gas

I will briefly outline how interactions between particles can be considered in the calculation of the temporal correlation function.

The second-order correlation function is proportional to the conditional probability of finding another particle at position $\mathbf{r}'$ when a particle is found at position $\mathbf{r}$. For a non-interacting bose gas, this is maximal for $\mathbf{r} = \mathbf{r}'$. Real particles of course cannot be at the same positions. The repulsive s-wave scattering between the particles reduces the probability of finding two particles in the same place. The correlation function is therefore reduced for $\mathbf{r} \approx \mathbf{r}'$. The second-order correlation function then becomes a function of the scattering length a of the atoms and takes the form (equation (4.26)

in reference [87])

$$\tilde{G}_i^{(2)}(\mathbf{r},\mathbf{r}',\tau) = \tilde{G}^{(2)}(\mathbf{r},\mathbf{r}',\tau)\left(1-\frac{a}{\mid R \mid}\right)^2 + \Big[\tilde{G}^{(1)}(\mathbf{r},\mathbf{r},\tau) \tilde{G}^{(1)}(\mathbf{r}',\mathbf{r}',\tau) - \left|\tilde{G}^{(1)}(\mathbf{r},\mathbf{r}',\tau)\right|^2\Big]\left[\left(1+\frac{a}{\mid R \mid}\right)^2 - 1\right], \tag{9.20}$$

which with equation 7.9 simplifies to

$$\tilde{G}_i^{(2)}(\mathbf{r},\mathbf{r}',\tau) = \tilde{G}^{(1)}(\mathbf{r},\mathbf{r},\tau)\tilde{G}^{(1)}(\mathbf{r}',\mathbf{r}',\tau)\left(1+\frac{2a^2}{\mathbf{R}^2}\right) + \left|\tilde{G}^{(1)}(\mathbf{r},\mathbf{r}',\tau)\right|^2\left(1-\frac{4a}{\mid \mathbf{R} \mid}\right). \tag{9.21}$$

To evaluate this modified $\tilde{G}_2$ we can use the unmodified function $\tilde{G}^{(1)}(\mathbf{r},\mathbf{r}',\tau)$ for the ideal gas. It is only slightly modified by the meanfield interactions, which are small as long as we do not consider a condensate.

When considering the effect of a gaussian beam, we have to integrate over equation 7.8 using the $G^{(2)}$ function found in equation 9.21. This integral, however, cannot be decomposed into one-dimensional integrals, since this $G^{(2)}$ depends on the inverse of the distance vector $\mathbf{r}$ and the full integral needs to be calculated numerically.

9.2.2 Condensation

We do now consider the correlation functions for a condensed cloud of Bosons. This section just considers the description of a non-interacting condensate.

When the atomic sample is partially or completely condensed, the measured density fluctuations are reduced. The particles in the condensate are in a coherent state [102]. In this case, we have to introduce a special treatment for the ground state and we write the first-order correlation function as a sum of the correlations in the condensate and the thermal correlation function $G_T^{(1)}$:

$$\tilde{G}^{(1)}(\mathbf{r},\mathbf{r}',\tau) = \left\langle \Psi^*(\mathbf{r},\tau)\Psi(\mathbf{r}',\tau)\right\rangle + G_T^{(1)}(\mathbf{r},\mathbf{r}',\tau). \tag{9.22}$$

The spatial component of the wave function of the ground state $\Psi_r(\mathbf{r})$ is given as the solution of the time-independent Schrödinger equation:

$$\left(\frac{\hbar^2\nabla^2}{2M} + V(\mathbf{r}) - \mu\right)\Psi_r(\mathbf{r}) = 0, \tag{9.23}$$

where we have to set the chemical potential μ equal to the ground state energy $\mu = \hbar(\Omega_x + \Omega_y + \Omega_z)/2$. A solution of this equation is just the ground state wave function of the harmonic potential, normalised to the number of particles in the condensate N_c [89]:

$$\Psi(\mathbf{r}) = \sqrt{N_c}\left(\Omega_x\Omega_y\Omega_z\right)^{1/4}\left(\frac{M}{\pi\hbar}\right)^{3/4}\exp\left[-\frac{M}{2\hbar}\left(\Omega_x x^2 + \Omega_y y^2 + \Omega_z z^2\right)\right]. \tag{9.24}$$

With the total number of particles N and a temperature of the thermal part T the fraction of condensed particles is:

$$\frac{N_c}{N} = 1 - \left(\frac{T}{T_c}\right)^3. \tag{9.25}$$

In the thermal part of the correlation function $G_T^{(1)}$ the chemical potential μ_T has to be set to 0 in the local density approximation. Therefore, the fugacity expansion done in the previous section is not possible any more. We can, however, calculate the spatial correlation function by Fourier transforming the Wigner function of the system, which is in the local density approximation equal to the momentum distribution of a spatially homogeneous gas, whose local potential energy is given by the local potential $V(\mathbf{q})$ [87]

$$W_{T,r}(\mathbf{p},\mathbf{r}) = (2\pi\hbar)^{-3}\,\frac{1}{\exp\left[\left(p^2/2m + V(\mathbf{r})\right)/k_BT\right] - 1}. \tag{9.26}$$

The correlation function in terms of this Wigner function is

$$G_{T,r}^{(1)}(\mathbf{r},\mathbf{r}') = \int d\mathbf{p}e^{-i\mathbf{p}(\mathbf{r}-\mathbf{r}')/\hbar}W_T(\mathbf{p},\frac{\mathbf{r}+\mathbf{r}'}{2}). \tag{9.27}$$

The integral

$$N_T = \int d^3\mathbf{r}\,G_T^{(1)}(\mathbf{r},\mathbf{r},\tau). \tag{9.28}$$

determines the number of atoms in the thermal cloud.

To calculate the time evolution we propagate the thermal and condensate part separately. In the condensate case the ground state energy is known and the time evolution is simply given as:

$$\Psi(\mathbf{r},\tau) = \Psi_r(\mathbf{r}) \exp\left[-\frac{i\hbar\tau}{2\hbar}\left(\Omega_x + \Omega_y + \Omega_z\right)\right] \tag{9.29}$$

For the thermal part we have to calculate the time evolution of the Wigner function. A way of doing so has been described by Wong [103].

The second-order correlation function can still be written in terms of the first-order correlation function, but corrections due to the condensate mean field need to be added:

$$\begin{aligned}\tilde{G}^{(2)}(\mathbf{r},\mathbf{r}',\tau) =& \tilde{G}^{(1)}(\mathbf{r},\mathbf{r},\tau)\tilde{G}^{(1)}(\mathbf{r}',\mathbf{r}',\tau) \\ &+ \mid \tilde{G}^{(1)}(\mathbf{r},\mathbf{r}',\tau) \mid^2 - \mid \Psi(\mathbf{r},\tau) \mid^2 \mid \Psi(\mathbf{r}',\tau) \mid^2 .\end{aligned} \tag{9.30}$$

Bibliography

[1] D. A. Steck. Rubidium 87 D line data, revision 2.1.1, 2009: *http://steck.us/alkalidata*.

[2] M. H. Anderson, J. R. Ensher, M. R. Matthews, C. E. Wieman, and E. A. Cornell. Observation of Bose-Einstein condensation in a dilute atomic vapor. *Science*, 269:198–201, Jul 1995.

[3] K. B. Davis, M.-O. Mewes, M. R. Andrews, N. J. van Druten, D. S. Durfee, D. M. Kurn, and W. Ketterle. Bose-Einstein condensation in a gas of sodium atoms. *Phys. Rev. Lett.*, 75(22):3969–3973, Nov 1995.

[4] C. C. Bradley, C. A. Sackett, J. J. Tollett, and R. G. Hulet. Evidence of Bose-Einstein condensation in an atomic gas with attractive interactions. *Phys. Rev. Lett.*, 75(9):1687–1690, Aug 1995.

[5] B. DeMarco and D. S. Jin. Onset of Fermi degeneracy in a trapped atomic gas. *Science*, 285(5434):1703–1706, 1999.

[6] M. Greiner, C. A. Regal, and D. S. Jin. Emergence of a molecular Bose-Einstein condensate from a Fermi gas. *Nature*, 426:537–540, 2003.

[7] S. Jochim, M. Bartenstein, A. Altmeyer, G. Hendl, S. Riedl, C. Chin, J. Hecker Denschlag, and R. Grimm. Bose-Einstein condensation of molecules. *Science*, 302(5653):2101–2103, 2003.

[8] M. W. Zwierlein, C. A. Stan, C. H. Schunck, S. M. F. Raupach, S. Gupta, Z. Hadzibabic, and W. Ketterle. Observation of Bose-Einstein condensation of molecules. *Phys. Rev. Lett.*, 91(25):250401, Dec 2003.

[9] M. Bartenstein, A. Altmeyer, S. Riedl, S. Jochim, C. Chin, J. Hecker Denschlag, and R. Grimm. Crossover from a molecular Bose-Einstein condensate to a degenerate Fermi gas. *Phys. Rev. Lett.*, 92(12):120401, Mar 2004.

[10] T. Bourdel, L. Khaykovich, J. Cubizolles, J. Zhang, F. Chevy, M. Teichmann, L. Tarruell, S. J. J. M. F. Kokkelmans, and C. Salomon. Experimental study of the BEC-BCS crossover region in lithium 6. *Physical Review Letters*, 93(5):050401, 2004.

[11] M. Greiner, O. Mandel, T. Esslinger, T. W. Hänsch, and I. Bloch. Quantum phase transition from a superfluid to a Mott insulator in a gas of ultracold atoms. *Nature*, 415:39 – 44, 2002.

[12] R. Folman, P. Krüger, J. Schmiedmayer, J. Denschlag, and C. Henkel. Microscopic atom optics: From wires to an atom chip. volume 48 of *Advances In Atomic, Molecular, and Optical Physics*, pages 263 – 356. Academic Press, 2002.

[13] J. Fortagh, A. Grossmann, C. Zimmermann, and T. W. Hänsch. Miniaturized wire trap for neutral atoms. *Phys. Rev. Lett.*, 81(24):5310–5313, Dec 1998.

[14] E. A. Hinds and I. G. Hughes. Magnetic atom optics: mirrors, guides, traps, and chips for atoms. *Journal of Physics D: Applied Physics*, 32(18):R119, 1999.

[15] T. Schumm, S. Hofferberth, L. M. Andersson, S. Wildermuth, S. Groth, I. Bar-Joseph, J. Schmiedmayer, and P. Kruger. Matter-wave interferometry in a double well on an atom chip. *Nat Phys*, 1:57–62, 10 2005.

[16] R. J. Sewell, J. Dingjan, F. Baumgärtner, I. Llorente-García, S. Eriksson, E. A. Hinds, G. Lewis, P. Srinivasan, Z. Moktadir, C. O. Gollasch, and M. Kraft. Atom chip for BEC interferometry. *Journal of Physics B: Atomic, Molecular and Optical Physics*, 43(5):051003, 2010.

[17] P. Krüger, S. Hofferberth, I. E. Mazets, I. Lesanovsky, and J. Schmiedmayer. Weakly interacting Bose gas in the one-dimensional limit. *Phys. Rev. Lett.*, 105:265302, Dec 2010.

[18] M. P. A. Jones, C. J. Vale, D. Sahagun, B. V. Hall, and E. A. Hinds. Spin coupling between cold atoms and the thermal fluctuations of a metal surface. *Phys. Rev. Lett.*, 91:080401, Aug 2003.

[19] M. P. A. Jones, C. J. Vale, D. Sahagun, B. V. Hall, C. C. Eberlein, B. E. Sauer, K. Furusawa, D. Richardson, and E. A. Hinds. Cold atoms probe the magnetic field near a wire. *Journal of Physics B: Atomic, Molecular and Optical Physics*, 37(2):L15, 2004.

[20] S. Wildermuth, S. Hofferberth, I. Lesanovsky, E. Haller, L. M. Andersson, S. Groth, I. Bar-Joseph, P. Kruger, and J. Schmiedmayer. Bose-Einstein condensates: Microscopic magnetic-field imaging. *Nature*, 435:440 – 440, 2005.

[21] M. F. Riedel, P. Böhi, Y. Li, T. W. Hänsch, A. Sinatra, and P. Treutlein. Atom-chip-based generation of entanglement for quantum metrology. *Nature*, 464:1170–1173, 04 2010.

[22] M. Wilzbach, D. Heine, S. Groth, X. Liu, T. Raub, B. Hessmo, and J. Schmiedmayer. Simple integrated single-atom detector. *Opt. Lett.*, 34(3):259–261, 2009.

[23] A. Takamizawa, T. Steinmetz, R. Delhuille, T. W. Hänsch, and J. Reichel. Miniature fluorescence detector for single atom observation on a microchip. *Opt. Express*, 14(23):10976–10983, 2006.

[24] Isabel Llorente García. *Advances in the design and operation of atom chips.* PhD thesis, Imperial College London, 2011.

[25] A. Mayer. Photonics in Europe, economic impact. European Technology Platform Photonics21, 12 2007.

[26] A. Politi, M. J. Cryan, J. G. Rarity, S. Yu, and J. L. O'Brien. Silica-on-silicon waveguide quantum circuits. *Science*, 320:646, 2008.

[27] A. Crespi, M. Lobino, J. C. F. Matthews, A. Politi, C. R. Neal, R. Ramponi, R. Osellame, and J. L. O'Brien. Measuring protein concentration with entangled photons. *ArXiv e-prints*, 2011. arXiv:1109.3128v1 [quant-ph].

[28] H. Schmidt and A. R. Hawkins. The photonic integration of non-solid media using optofluidics. *Nat Photon*, 5:598–604, 10 2011.

[29] J. E. Lye, J. J. Hope, and J. D. Close. Nondestructive dynamic detectors for Bose-Einstein condensates. *Phys. Rev. A*, 67:043609, Apr 2003.

[30] S. S. Szigeti, M. R. Hush, A. R. R. Carvalho, and J. J. Hope. Continuous measurement feedback control of a Bose-Einstein condensate using phase-contrast imaging. *Phys. Rev. A*, 80(1):013614, Jul 2009.

[31] S. S. Szigeti, M. R. Hush, A. R. R. Carvalho, and J. J. Hope. Feedback control of an interacting Bose-Einstein condensate using phase-contrast imaging. *Phys. Rev. A*, 82(4):043632, Oct 2010.

[32] J. J. Hope and J. D. Close. General limit to nondestructive optical detection of atoms. *Phys. Rev. A*, 71(4):043822, Apr 2005.

[33] A. M. Streltsov and N. F. Borrelli. Study of femtosecond-laser-written waveguides in glasses. *J. Opt. Soc. Am. B*, 19(10):2496–2504, Oct 2002.

[34] M. Svalgaard, C.V. Poulsen, A. Bjarklev, and O. Poulsen. Direct UV writing of buried singlemode channel waveguides in Ge-doped silica films. *Electronics Letters*, 30(17):1401 –1403, aug 1994.

[35] S.J. Hewlett and F. Ladouceur. Fourier decomposition method applied to mapped infinite domains: scalar analysis of dielectric waveguides down to modal cutoff. *Lightwave Technology, Journal of*, 13(3):375 –383, mar 1995.

[36] Karl Joachim Ebeling. *Integrated optoelectronics : waveguide optics, photonics, semiconductors*. Springer-Verlag, 1993.

[37] Bahaa E. A. Saleh and Malvin Carl Teich. *Fundamentals of Photonics*. John Wiley and Sons, Inc., 1991.

[38] Eric R.I. Abraham and Eric A. Cornell. Teflon feedthrough for coupling optical fibers into ultrahigh vacuum systems. *Appl. Opt.*, 37(10):1762–1763, Apr 1998.

[39] Claude Cohen-Tannoudji, Jacques Dupont-Roc, and Gilbert Grynberg. *Atom-Photon interaction*. Wiley-Interscience, 1 edition, 1992.

[40] I. I. Sobelman. *Atomic spectra and radiative transitions*. Springer-Verlag, 1979.

[41] P.J. Ungar, D.S. Weiss, E. Riis, and S. Chu. Optical molasses and multilevel atoms: theory. *J. Opt. Soc. Am. B*, 6(11), 1989.

[42] John von Neumann. Wahrscheinlichkeitstheoretischer Aufbau der Quantenmechanik. *Göttinger Nachrichten*, 1:245–272.

[43] V. Weisskopf and E. Wigner. Berechnung der natürlichen Linienbreite auf Grund der Diracschen Lichttheorie. *Zeit. f. Phys.*, 93(54), 1930.

[44] Rodney Loudon. *The quantum theory of light*. Oxford University Press, 3 edition, 2000.

[45] Pierre Meystre and Murray Sargent III. *Elements of Quantum Optics*. Springer-Verlag, 3 edition, 1998.

[46] Hermann Haken and Hans Christoph Wolf. *Atom- und Quantenphysik*. Springer Verlag, 1993.

[47] Harold J. Metcalf and Peter van der Straten. *Laser Cooling and Trapping*. Springer-Verlag, New York, 1999.

[48] Christopher D. J. Sinclair. *Bose-Einstein Condensation of Microtraps on Videotape*. PhD thesis, Imperial College London, 2005.

[49] Manuel Succo. *An integrated optical-waveguide chip for measurement of cold-atom clouds*. PhD thesis, Imperial College London, 2011.

[50] Z. T. Lu, K. L. Corwin, M. J. Renn, M. H. Anderson, E. A. Cornell, and C. E. Wieman. Low-velocity intense source of atoms from a magneto-optical trap. *Phys. Rev. Lett.*, 77(16):3331–3334, Oct 1996.

[51] A. S. Arnold, J. S. Wilson, and M. G. Boshier. A simple extended-cavity diode laser. 69(3):1236–1239, 1998.

[52] C. Wieman and T. W. Hänsch. Doppler-free laser polarization spectroscopy. *Phys. Rev. Lett.*, 36(20):1170–1173, May 1976.

[53] Jocelyn Anna Retter. *Cold Atom Microtraps abova a Videotape Surface*. PhD thesis, University of Sussex, 2002.

[54] G. Ritt, G. Cennini, C. Geckeler, and M. Weitz. Laser frequency offset locking using a side of filter technique. *Applied Physics B: Lasers and Optics*, 79:363–365, 2004. 10.1007/s00340-004-1559-6.

[55] D. S. Weiss, E. Riis, Y. Shevy, P. J. Ungar, and S. Chu. Optical molasses and multilevel atoms: experiment. *J. Opt. Soc. Am. B*, 6(11):2072–2083, Nov 1989.

[56] J. Reichel, W. Hänsel, and T. W. Hänsch. Atomic micromanipulation with magnetic surface traps. *Phys. Rev. Lett.*, 83:3398–3401, Oct 1999.

[57] S. Wildermuth, P. Krüger, C. Becker, M. Brajdic, S. Haupt, A. Kasper, R. Folman, and J. Schmiedmayer. Optimized magneto-optical trap for experiments with ultracold atoms near surfaces. *Phys. Rev. A*, 69(030901), 2004.

[58] M. Kohnen, M. Succo, P. G. Petrov, R. A. Nyman, M. Trupke, and Hinds E. A. An array of integrated atom-photon junctions. *Nat. Photon*, 5(1):35–38, 2011.

[59] M Kohnen, P G Petrov, R A Nyman, and E A Hinds. Minimally destructive detection of magnetically trapped atoms using frequency-synthesized light. *New Journal of Physics*, 13(8):085006, 2011.

[60] M. R. Andrews, M.-O. Mewes, N. J. van Druten, D. S. Durfee, D. M. Kurn, and W. Ketterle. Direct, nondestructive observation of a Bose condensate. *Science*, 273(5271):84–87, July 1996.

[61] M. R. Matthews, B. P. Anderson, P. C. Haljan, D. S. Hall, M. J. Holland, J. E. Williams, C. E. Wieman, and E. A. Cornell. Watching a superfluid untwist itself: Recurrence of Rabi oscillations in a Bose-Einstein condensate. *Phys. Rev. Lett.*, 83(17):3358–3361, Oct 1999.

[62] C. McKenzie, J. Hecker Denschlag, H. Häffner, A. Browaeys, Luís E. E. de Araujo, F. K. Fatemi, K. M. Jones, J. E. Simsarian, D. Cho, A. Simoni, E. Tiesinga, P. S. Julienne, K. Helmerson, P. D. Lett, S. L. Rolston, and W. D. Phillips. Photoassociation of sodium in a Bose-Einstein condensate. *Phys. Rev. Lett.*, 88(12):120403, Mar 2002.

[63] J. M. Higbie, L. E. Sadler, S. Inouye, A. P. Chikkatur, S. R. Leslie, K. L. Moore, V. Savalli, and D. M. Stamper-Kurn. Direct nondestructive

imaging of magnetization in a spin-1 Bose-Einstein gas. *Phys. Rev. Lett.*, 95(5):050401, Jul 2005.

[64] S. Levy, E. Lahoud, I. Shomroni, and J. Steinhauer. The a.c. and d.c. Josephson effects in a Bose-Einstein condensate. *Nature*, 449:579–583, October 2007.

[65] P. G. Petrov, D. Oblak, C. L. Garrido Alzar, N. Kjærgaard, and E. S. Polzik. Non-destructive interferometric characterization of an optical dipole trap. *Phys. Rev. A*, 75(033803), 2007.

[66] T. Fischer, P. Maunz, P. W. H. Pinkse, T. Puppe, and G. Rempe. Feedback on the motion of a single atom in an optical cavity. *Phys. Rev. Lett.*, 88(16):163002, Apr 2002.

[67] A. Kubanek, M. Koch, C. Sames, A. Ourjoumtsev, P. W. H. Pinkse, K. Murr, and G. Rempe. Photon-by-photon feedback control of a single-atom trajectory. *Nature*, 462(7275):898–901, December 2009.

[68] G. C. Bjorklund, M. D. Levenson, W. Lenth, and C. Ortiz. Frequency modulation FM spectroscopy. *Applied Physics B: Lasers and Optics*, 32:145–152, 1983.

[69] V. Savalli, G. Zs. K. Horvath, P. D. Featonby, L. Cognet, N. Westbrook, C. I. Westbrook, and A. Aspect. Optical detection of cold atoms without spontaneous emission. *Opt. Lett.*, 24(22):1552–1554, 1999.

[70] S. Bernon, T. Vanderbruggen, R. Kohlhaas, A. Bertoldi, A. Landragin, and P. Bouyer. Heterodyne non-demolition measurements on cold atomic samples: towards the preparation of non-classical states for atom interferometry. *New Journal of Physics*, 13(6):065021, 2011.

[71] J. E. Lye, B. D. Cuthbertson, H.-A. Bachor, and J. D. Close. Phase modulation spectroscopy: a non-destructive probe of Bose-Einstein condensates. *J. Opt. B: Quantum Semiclass. Opt.*, 1(4):402, 1999.

[72] M. Saffman, D. Oblak, J. Appel, and E. S. Polzik. Spin squeezing of atomic ensembles by multicolor quantum nondemolition measurements. *Phys. Rev. A*, 79(2):023831, Feb 2009.

[73] P. J. Windpassinger, D. Oblak, U. Busk Hoff, J. Appel, N. Kjærgaard, and E. S. Polzik. Inhomogeneous light shift effects on atomic quantum state evolution in non-destructive measurements. *New Journal of Physics*, 10(5):053032, 2008.

[74] J. Lodewyck, P. G. Westergaard, and P. Lemonde. Nondestructive measurement of the transition probability in a Sr optical lattice clock. *Phys. Rev. A*, 79(6):061401, Jun 2009.

[75] P. Horak, B. G. Klappauf, A. Haase, R. Folman, J. Schmiedmayer, P. Domokos, and E. A. Hinds. Possibility of single-atom detection on a chip. *Phys. Rev. A*, 67(4):043806, Apr 2003.

[76] C. M. Caves. Quantum-mechanical noise in an interferometer. *Phys. Rev. D*, 23(8):1693–1708, Apr 1981.

[77] S. Kasapi, S. Lathi, and Y. Yamamoto. Sub-shot-noise FM noise spectroscopy of trapped rubidium atoms. *J. Opt. Soc. Am. B*, 15(10):2626–2630, 1998.

[78] H. Mabuchi, J. Ye, and H.J. Kimble. Full observation of single-atom dynamics in cavity QED. *Applied Physics B: Lasers and Optics*, 68:1095–1108, 1999.

[79] R. Long, A. K. Tuchman, and M. A. Kasevich. Multiple frequency modulation for low-light atom measurements in an optical cavity. *Opt. Lett.*, 32(17):2502–2504, 2007.

[80] Paul Horowitz and Winfield Hill. *The art of electronics*. Cambridge University Press, 1980.

[81] R. Hanbury Brown and R. Q. Twiss. Correlation between photons in two coherent beams of light. *Nature*, 177:27–29, 1956.

[82] Masami Yasuda and Fujio Shimizu. Observation of two-atom correlation of an ultracold neon atomic beam. *Phys. Rev. Lett.*, 77:3090–3093, Oct 1996.

[83] M. Schellekens, R. Hoppeler, A. Perrin, J. Viana Gomes, D. Boiron, A. Aspect, and C. I. Westbrook. Hanbury Brown-Twiss effect for ultracold quantum gases. *Science*, 310(5748):648–651, 2005.

[84] T. Jeltes, J. M. McNamara, W. Hogervorst, W. Vassen, V. Krachmalnicoff, M. Schellekens, A. Perrin, H. Chang, D. Boiron, A. Aspect, and C. I. Westbrook. Comparison of the Hanbury Brown-Twiss effect for bosons and fermions. *Nature*, 445:402–405, 2007.

[85] J. Esteve, J.-B. Trebbia, T. Schumm, A. Aspect, C. I. Westbrook, and I. Bouchoule. Observations of density fluctuations in an elongated Bose gas: Ideal gas and quasicondensate regimes. *Phys. Rev. Lett.*, 96(13):130403, Apr 2006.

[86] J. Armijo, T. Jacqmin, K. V. Kheruntsyan, and I. Bouchoule. Probing three-body correlations in a quantum gas using the measurement of the third moment of density fluctuations. *Phys. Rev. Lett.*, 105:230402, Nov 2010.

[87] M. Naraschewski and R. J. Glauber. Spatial coherence and density correlations of trapped Bose gases. *Phys. Rev. A*, 59(6):4595–4607, Jun 1999.

[88] J. J. Sakurai. *Modern quantum mechanics*. Addison-Wesly, 1994.

[89] Lev Pitaevskii and Sandro Stringari. *Bose-Einstein Condensation*. Oxford Science Publications, 2003.

[90] R. J. Barlow. *Statistics*. John Wiley and Sons, 1989.

[91] R. Nyman, S. Scheel, and E. Hinds. Prospects for using integrated atom-photon junctions for quantum information processing. *Quantum Information Processing*, 10:941–953, 2011.

[92] M. D. Lukin, M. Fleischhauer, R. Cote, L. M. Duan, D. Jaksch, J. I. Cirac, and P. Zoller. Dipole blockade and quantum information processing in mesoscopic atomic ensembles. *Phys. Rev. Lett.*, 87:037901, Jun 2001.

[93] M. Saffman, T. G. Walker, and K. Mølmer. Quantum information with Rydberg atoms. *Rev. Mod. Phys.*, 82:2313–2363, Aug 2010.

[94] Masao Kawachi. Silica waveguides on silicon and their application to integrated-optic components. *Optical and Quantum Electronics*, 22:391–416, 1990. 10.1007/BF02113964.

[95] S. Pollock, J. P. Cotter, A. Laliotis, and E. A. Hinds. Integrated magneto-optical traps on a chip using silicon pyramid structures. *Opt. Express*, 17(16):14109–14114, Aug 2009.

[96] S. Pollock, J. P. Cotter, A. Laliotis, F. Ramirez-Martinez, and E. A. Hinds. Characteristics of integrated magneto-optical traps for atom chips. *New Journal of Physics*, 13(4):043029, 2011.

[97] M. Trupke, J. Goldwin, B. Darquie, G. Dutier, S. Eriksson, J. Ashmore, and E. A. Hinds. Atom detection and photon production in a scalable, open, optical microcavity. *Phys. Rev. Lett.*, 99(063601), 2007.

[98] J. Goldwin, M. Trupke, J. Kenner, A. Ratnapala, and E.A. Hinds. Fast cavity-enhanced atom detection with low noise and high fidelity. *Nat Commun*, 2:418, 08 2011.

[99] J. Hwang and E. A. Hinds. Dye molecules as single-photon sources and large optical nonlinearities on a chip. *New Journal of Physics*, 13(8):085009, 2011.

[100] G. Lepert, M. Trupke, M. J. Hartmann, M. B. Plenio, and E. A. Hinds. Arrays of waveguide-coupled optical cavities that interact strongly with atoms. *New Journal of Physics*, 13(11):113002, 2011.

[101] M. Teich, K. Matsuo, and B. Saleh. Excess noise factors for conventional and superlattice avalanche photodiodes and photomultiplier tubes. *IEEE Journal of Quantum Electronics*, 22:1184–1193, 1986.

[102] Roy J. Glauber. The quantum theory of optical coherence. *Phys. Rev.*, 130:2529–2539, Jun 1963.

[103] C.-Y. Wong. Explicit solution of the time evolution of the Wigner function. *J. Opt. B: Quantum Semiclass. Opt.*, 5(420), 2003.